Analytical and Computational Techniques for Fluid Flows Interacting with Intense Radiation Fields

by

Griffin S. Cearley

A dissertation submitted in partial fulfillment
of the requirements for the degree of
Doctor of Philosophy
(Mechanical Engineering and Scientific Computing)
in The University of Michigan
2022

Doctoral Committee:

Associate Professor Eric Johnsen, Chair
Assistant Professor Rohini Bala Chandran
Professor Smadar Karni
Associate Professor Carolyn Kuranz
Dr. Peter Porazik, Lawrence Livermore National Laboratory

Griffin S. Cearley

gcearle@umich.edu

ORCID iD: 0000-0002-4072-0809

For my late grandfather Paul Beauprè, my first friend in learning.

ACKNOWLEDGEMENTS

This dissertation is the culmination of a long experience that has been as rewarding and as it has been difficult. The process has taught me invaluable skills, both technical and non-technical, but I believe the most important lessons have been in patience, determination, and self-sufficiency. Without the support of many individuals, this achievement would not have been possible. First, I would like to thank my family, including my parents Charles and Suzanne, and my brother Cooper. Without their love and support, I certainly would not have continued past moments of uncertainty that occurred along the way. I would also like to thank my friends: Hayden, Lucca, Alyssa, Heath, and others. Your friendship means more to me than you can know.

There are few institutions that combine an unwavering commitment to excellence with the supportive, collaborative environment I have found at the University of Michigan. The scale of such an institution makes it impossible to acknowledge all of the individuals that have contributed to my success on behalf of the university, but I will try. I would like to thank my advisor, Eric Johnsen, for his seemingly endless patience and advocacy, and his dedication to sharing his love of research. I would also like to thank Peter Porazik and Carolyn Kuranz for their phenomenal mentorship, and for their service on my dissertation committee. I would also like to thank Smadar Karni and Rohini Bala Chandran for their service on my committee, and for their valuable input on this dissertation. I would like to thank all of the ASO staff that work so hard to make sure the department's graduate students are happy, supported and compensated. I would like to thank my colleagues in the Auto Lab for sharing

their technical insights and companionship. I would also like to thank the students in Carolyn Kuranz's group, as my interactions with them taught me a great deal about the field of high-energy-density physics.

This work was supported in part by the Lawrence Livermore National Laboratory under subcontracts B642551 and B632749.

TABLE OF CONTENTS

LIST OF FIGURES

Figure

LIST OF APPENDICES

Appendix

LIST OF ABBREVIATIONS

HED High-energy-density

RT Rayleigh-Taylor

ICF Inertial confinement fusion

DG Discontinuous Galerkin

NIF National Ignition Facility

BBAY Bethe, Bade, Averell, and Yos (model)

XTRRA X-ray Transport and Radiation Response Assessment

PDI Photon Displacement Interferometry

ABSTRACT

The field of high-energy-density (HED) physics features many problems of importance to society, including stellar formation in astrophysics as well as next-generation energy technologies. Often, these systems involve complex fluid flows, such as mixing between different fluids, that are influenced by radiation fields. Predicting the evolution of these systems requires understanding the role of the two-way coupling between radiation and the fluid flow. The development of experimental techniques for creating and diagnosing HED systems has greatly expanded our understanding of their evolution. However, these experiments are challenging, and the state of HED plasmas often cannot be completely constrained by available diagnostics. Analytical and computational tools provide valuable insight in predicting quantities that may be difficult to glean from experiments.

Intense sources of radiation drive ablative flow in many applications, generating impulse and driving a compression wave into the bulk material. Analytical models exist to predict the impulse generated in materials exposed to radiation, but they depend on the energy of the blown-off material, which in general is not known due to the complex partitioning of energy that occurs in the system. The uncertainty associated with measurements of x-ray spectra poses another difficulty in predicting the impulse generated in an irradiated material. We address these issues via a data-driven approach to modeling the impulse generated in materials exposed to a given x-ray source spectrum. We use data from high-fidelity simulations to inform an analytical model

for the impulse generated in a given material by an arbitrary radiation source. This model also provides an analytical form for the impulse-spectrum sensitivity, a quantity that is important for constraining the uncertainty in impulse resulting from uncertainty in the source spectrum. The model for the impulse-spectrum sensitivity agrees well with the sensitivity evaluated directly from simulations, requires significantly less computation time, and can also be evaluated using data from experiments. This work enables low-cost prediction of important quantities in the radiation-generated impulse in materials. The modeling approach we propose greatly simplifies the study of such systems, as well as the design of robust experiments.

Numerical simulation of HED systems poses a challenge, as the problems tend to be multi-scale and involve fundamentally different, often competing, physical processes. The discontinuous Galerkin (DG) method offers many advantages, particularly as computing architectures evolve to offer exascale capabilities. In particular, DG offers arbitrarily high-order accuracy with a compact stencil, making it well-suited for parallel scaling. However, high-order methods have seen limited application to the study of HED systems. As we are primarily interested in the study of multi-material flows in intense radiation fields, we extend interface capturing techniques used for classical fluid flows to radiation hydrodynamics in the framework of the DG discretization. Our approach uses a careful, physically consistent treatment of material interfaces, including a limiting procedure designed to prevent unphysical errors that occur from other approaches. This development results in an approach that is high-order accurate, conservative, physically consistent, and well-suited for parallel computation of radiation hydrodynamics. We demonstrate these properties of the method using one-dimensional verification problems, as well as a two-dimensional problem relevant to HED science. This work demonstrates the promising application of high-order numerical methods to practical problems in HED science, a field that has seen limited application of such methods.

CHAPTER I

Introduction

This chapter describes the scope of this dissertation and motivates the work within using applications in the fields of physics and engineering. This research belongs in the context of high-energy-density physics, which will be defined in the following section along with other key physical concepts, such as radiation hydrodynamics. Additionally, we detail the models we will use to describe the phenomena of interest, as well as the assumptions upon which they rely. We discuss the motivation for the specific approaches used in this work, namely high-order numerical methods and sensitivity analysis. Finally, we provide an overview of this dissertation, including an outline complete with the objective of each chapter.

1.1 High-energy-density physics

High-energy-density (HED) systems are loosely defined as systems featuring material under extremely high pressures. A criterion for a more quantitative definition has specified thermodynamic pressures of one million atmospheres, approximately 1 Megabar [1]. However, a more useful criterion simply requires pressures large enough that traditional descriptions of condensed matter are insufficient, which can occur at pressures on the order of 0.1 Mbar [2]. Accordingly, HED systems may involve an array of effects that complicate their description, including non-ideal plasma effects

such as strong Coulomb interactions [3, 4, 5], radiation effects that may dominate the energy fluxes or energy densities of the system [6, 7, 8], and strongly relativistic [9, 10] or strongly quantum-mechanical [11, 12] behavior. Each of these complicating factors is rich enough to merit its own body of research, but in the present work we restrict ourselves to studying the effects of radiation.

Recent development of HED science has occurred in large part due to revolutionary experimental techniques developed in the 1980's and 1990's. These developments include high-energy laser systems that can concentrate large amounts of energy into relatively small targets [13, 14, 15], wire-array Z-pinch systems that use the Lorentz force to rapidly compress targets [16], as well as ultrafast laser systems achieving unprecedented intensities, enabling laboratory study of relativistic systems [17]. Alongside these methods for driving HED experiments evolved techniques for diagnosing these systems, requiring imaging or spectroscopic measurement on sub-nanosecond time-scales [18, 19]. These systems enabled laboratory study of new physical phenomena that were previously only conceived of theoretically, most often in the field of astrophysics. These techniques enabled development of intense sources of x-ray radiation, which are used to drive experiments [20, 21, 22, 23] as well as in diagnostics [24].

Radiation hydrodynamics is the study of systems in which the exchange of energy and/or momentum with electromagnetic radiation significantly affects fluid flow [25]. Examples of flows that interact with radiation in this manner are virtually absent from everyday life on Earth. However, the high-pressure environments of HED systems give rise to temperatures at which radiative energy fluxes are significant when compared to those of the fluid. Such systems are said to be in the radiative flux regime, and are frequently created and diagnosed in HED laboratory experiments [26]. In the radiation-dominated regime, the energy content contained by the radiation component of system is on the order of that of the material. Due to the extremely

high temperatures required, the radiation-dominated regime is more difficult to obtain. However, many astrophysical systems, such stellar interiors, are in this regime. We will discuss these regimes and other characteristics of radiation hydrodynamics systems further in Section 1.3.2.

As discussed previously, the development of HED science was enabled by powerful experimental techniques, but computational tools have played arguably an equally important role. HED experiments use an immense amount of energy and very high-precision manufactured targets, which are often completely vaporized or unretrievable afterwards. Therefore, experiments on current facilities are limited in terms of repetition rate [27]. Additionally, due to the difficulty of diagnosing HED systems, certain quantities of interest may not be constrained by measurements obtained during experiments. Computational codes that simulate different aspects of the experimental system enable predictions important to the design of experiments [28]. Additionally, numerical simulations allow researchers to vary parameters that cannot readily be varied in the experiments, as well as inform the values of quantities that could not be measured experimentally [29]. This benefitial relationship computation and experiment is bilateral, as experimental methods enable new physical models employed in simulations to be validated [30, 31].

HED systems are multiphysics systems, in which fundamentally different nonlinear physical processes must be modeled. The presence of different physical processes typically causes a variety of physical scales (e.g., time scales, length scales) to exist. The multiscale nature of HED systems poses a challenge for computational approaches, as different scales and physics may require different solution methodologies (e.g., diffusive processes are typically discretized differently than convective processes) [32]. This difficulty is often handled through operator splitting, in which discretization is applied to each scale or physical process separately [33]. An example of this type of approach is implicit-explicit schemes, where terms that are stiff are integrated implicitly for

stability [34]. Additionally, the complications inherent to multiphysics systems often make traditional analytical approaches less feasible than in single-process systems. In this context, data-driven approaches to developing analytical models have proven useful in a number of multiphysics systems, including HED science [35, 36, 37].

In this work, we focus on radiation hydrodynamics phenomena in HED systems, and make some assumptions that allow us to focus on this interplay between fluid flow and radiation transport. We are particularly interested in HED systems featuring phenomena that occur at interfaces between materials, including radiation-driven ablation and blow-off at material surfaces, as well as the growth of hydrodynamic instabilities that seed turbulent mixing in radiative environments. In particular, this dissertation provides a data-driven modeling approach to describe radiation-driven blow off in materials, and a computational approach to simulating instability growth and turbulent mixing in multifluid radiation hydrodynamics systems.

1.2 Relevant applications

Radiation hydrodynamics systems appear in a number of areas in science and engineering that are important to modern society. In addition to naturally existing in astrophysical systems, radiation hydrodynamics is also relevant to energy technologies. We will find, in a more detailed discussion of these application areas, that complex hydrodynamic flows often occur in radiative environments in HED systems. A fundamental understanding of the interaction between intense radiation fields and the evolution of these flows is crucial to each of these practical areas of science and engineering.

1.2.1 Emission nebulae

Astrophysical systems feature phenomena that involve fluid flows interacting with radiation fields. Due to the very low density of matter in the vast majority of space,

radiation emitted by stars is able to stream large distances with little attenuation. The radiative fluxes seen by celestial objects can therefore be large enough to directly drive flow. One type of celestial object whose very origin is a direct consequence of the interaction of intense radiation and hydrodynamics is cold pillar structures observed in emission nebulae.

Emission nebulae form due to the intense ultraviolet radiation emitted from young O and B-type stars, which travels through the near-vacuum of the interstellar medium until encountering cold clouds comprised of molecular hydrogen gas. Absorption of this radiation causes the clouds to ionize, expand, and rarefy, forming emission nebulae containing relatively hot, ionized hydrogen [38, 39]. Often observed jutting into these regions are relatively cold pillars of unionized (molecular) hydrogen, like the *Pillars of Creation* shown in Figure 1.1. The *Pillars of Creation* are massive; the vertical scale of the structures pictured in Figure 1.1 is approximately 70 light years. While the exact mechanism for the formation of these cold molecular pillars is debated, it is clear from velocity gradients measured across cold molecular pillars that they were created by the hydrodynamic flow driven by radiative fluxes during the formation of the emission nebula, and that this evolution is ongoing [40]. These cold molecular pillars are continually irradiated, which causes the gas within them to compress, a process that is believed to trigger the birth of new stars by gravitational instabilities [41].

There are two competing theories explaining the mechanism for the creation of cold molecular pillars that extend into emission nebulae. One theory describes the pillars as being penetrating spikes of cold molecular hydrogen that grew as a result of the Rayleigh-Taylor instability [42]. This instability arises as the photoionization fronts that carve out the emission nebulae slow down, causing heavier molecular hydrogen to accelerate into lighter ionized hydrogen [43, 44, 45]. The second theory attributes the structures to pre-existing dense clumps within the cloud which retard

Figure 1.1: Hubble Space Telescope image of the Pillars of Creation within the Messier 16 emission nebula. Reproduced with permission from `www.nasa.gov`.

the propagation of the ionization front, effectively shielding the gas behind it from ionizing radiation [46, 47]. Computational and experimental studies have attempted to re-create the development of these structures based on these two theories [48], but as of this writing neither theory clearly prevails. Understanding the effects of radiation in initiating the flows creating these structures — as well as the interplay between radiation and hydrodynamics as they continue to evolve — is essential to explaining the origins of important sites for stellar birth and cosmology.

1.2.2 Core-collapse supernovae

In addition to playing a role in the birth of stars, radiation hydrodynamics governs the death of stars as well. Stars larger than eight solar masses conclude their lives in extremely powerful explosions called core-collapse, or Type-II, supernovae. Core-collapse supernovae are the most powerful explosions in the universe, at their peak releasing 10^{46} Watts in the form of neutrinos, which is as much instantaneous power as the rest of the visible Universe combined [49]. These events are important

cosmically: a large fraction of heavy elements were created in core collapse supernovae, explosions that act to disperse these heavy elements throughout the universe. In fact, humans are (by mass) approximately 60% comprised of oxygen that was created and scattered by core collapse supernovae [50]. Here we describe the physics of core collapse supernovae, the most common kind of supernova in the universe [51].

Massive stars begin in the main sequence, burning hydrogen in their cores via nuclear fusion [52]. The fusion reaction generates neutrons, which exert a pressure in hydrostatic equilibrium with the gravitational force pulling the star inward on itself. The hydrogen fuses to form helium, which eventually replaces the center of the star. As the star approaches the end of its life, burning hydrogen remains outside the new helium core. This process continues, as heavier and heavier elements fuse in successive interior layers of the star: hydrogen, helium, carbon, neon, oxygen, and then silicon. Each stage causes the center of the star to grow hotter and denser. Eventually, the silicon fuses to produce a core of about 1.5 solar masses of iron. Because the nuclear binding energy per nucleon is at a maximum for iron, no more energy can be produced by fusing iron and the fusion cycle stops. At this point gravitational forces become dominant, driving the star's iron core to collapse inward, achieving local flow velocities of about a quarter of the speed of light ($\approx$ 70,000 km/s) [53]. Because the core collapses so quickly and the gravitational force is much weaker acting on lighter elements far from the core, the less dense outer layers remain static. An iron core that was the size of the Earth collapses into a sphere only 30 km in radius, creating extremely high temperatures and densities. This process is eventually halted by the short-range nuclear force, after the core has attained the nuclear mass density of around 5 $\times 10^{14}$ g/cm^3 [49].

The abrupt stagnation of the collapsing core causes a shockwave to propagate outward, but this shockwave stalls at the outer edge of the core due to large neutrino losses and photodisintegration. It is unclear why the stalled shockwave restarts its

outward propagation. However, the incredibly hot, dense, neutron-rich core radiates 10% of its rest mass in the form of neutrinos; it is believed that the flux of neutrinos from the core is sufficient at the stalled shock front to restart the shockwave [54]. As the rebound of the core ends and again falls inward, it generates a rarefaction wave that catches the shock [55]. As these waves travels outward, they interacts with stratified layers of decreasing density. Each interaction causes a reflected shock to travel in the opposite direction. As the expanding ejecta decelerates, the material interfaces located between the inward and outward-traveling shocks become unstable to hydrodynamic instabilities, such as the Rayleigh-Taylor (RT) instability [42]. This process is illustrated in Figure 1.2. The RT instability causes interpenetrating structures to grow between the layers composed of different elements. HED experiments have shown that the growth of these structures are likely influenced by the magnitude of radiative fluxes present in the system [56]. It is believed that the mixing between these material layers may provide the conditions for synthesis for even higher elements than those produced within the star [57]. Therefore, studying how radiation affects the growth of RT and other instabilities is important to understanding the chemical origins of our universe.

1.2.3 Inertial confinement fusion

Radiation hydrodynamics is also relevant to renewable energy technologies. Current research in nuclear fusion is focused on reactions between hydrogen atoms, creating energy in the form of neutrons without generating harmful or polluting by-products [58]. Unlike fission, fusion requires overcoming the Coulomb force that repels like-charged atomic nuclei, which only occurs *en masse* given extremely hot, dense conditions [59]. While mankind has been able to create these conditions within thermonuclear weapons by use of a primary fission explosion [60], creating these conditions in a controlled manner suitable for power production poses challenges. Among

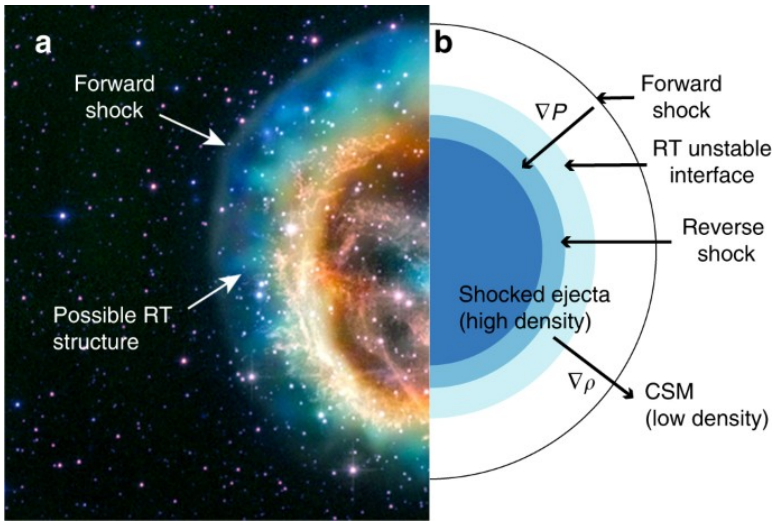

Figure 1.2: (a) Image of supernova remnant E0102.2-72, located in the Small Megallanic Cloud, and (b) schematic showing structure and gradients of a supernova explosion. Reproduced with permission from Kuranz et al. [56].

the most promising schemes for controlled nuclear fusion is inertial confinement fusion (ICF), a family of schemes for heating, compressing, and confining nuclear fusion fuel using x-rays or lasers [61]. ICF has the potential of becoming a clean, renewable source of energy that may require smaller facilities and less cost than other alternatives [62]. Figure 1.3 is a schematic of the two main ICF schemes: indirect and direct drive.

Indirect drive ICF utilizes powerful laser pulses to heat the inner wall of a gold cylinder, known as a hohlraum, which houses a capsule containing fusion fuel. Heating the hohlraum wall causes x-rays to be emitted, converting the laser energy into an x-ray environment of millions of degrees [63]. The direct-drive scheme skips this step, directly applying laser energy to the capsule. The capsule is composed of a solid shell filled with a mixture of deuterium and tritium gas and comprised of an outer ablator layer, typically made of plastic, Beryllium, or diamond, coated on the

inside with a layer of cryogenically frozen deuterium-tritium fuel. The ablator layer of the capsule absorbs x-rays (or laser beams), which cause it to ablate, or blow off. As nature demands that momentum be balanced, the remaining capsule is driven inward, accelerating to hundreds of kilometers per second [63]. As this spherical flow converges at the center, it stagnates, forming a hot-spot in which densities of approximately 100 g/cm^3 and temperatures of hundreds of millions of degrees are attained [64]. The hot-spot needs to have sufficiently high densities to stop the reaction products (neutrons and α-particles) created by fusing fuel elsewhere, so that these products can further heat the fuel and produce a burning, self-heating plasma wherein the fuel ions fuse in a chain reaction [65]. Achieving the in-flight velocities and hot-spot conditions required to create a burning plasma requires a symmetric implosion, such that the conversion of the kinetic energy of the shell to the internal energy of fuel within the hotspot is efficient.

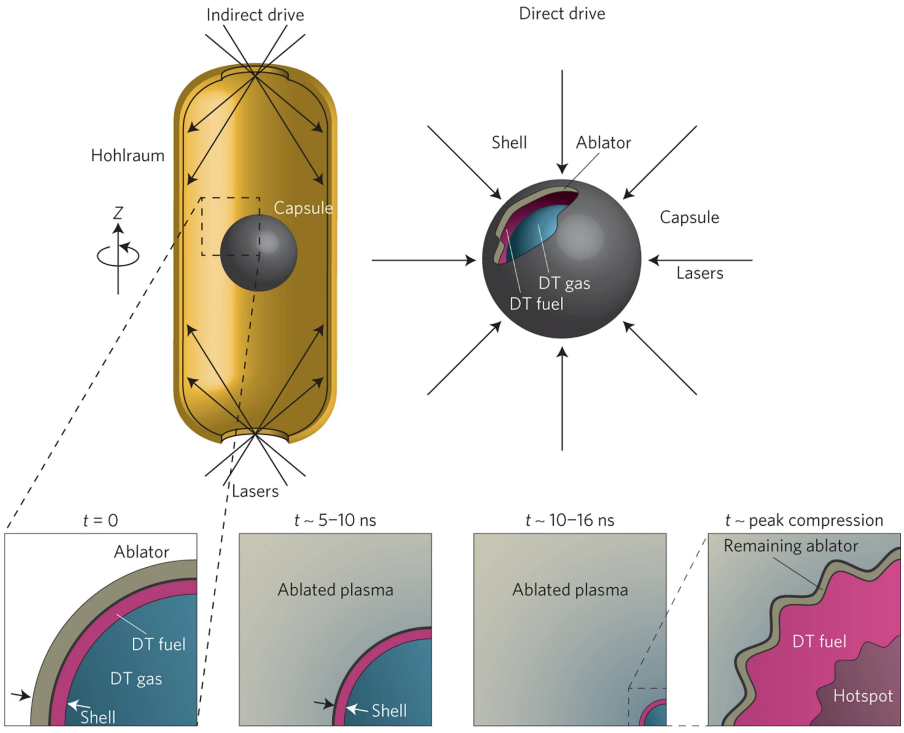

Figure 1.3: Schematic of indirect-drive (left) and direct-drive (right) inertial confinement fusion configurations. Reproduced with permission from Betti et al. [61].

Historically, the performance of ICF experiments has been limited by the growth of in-flight asymmetries that prevent the implosion from being perfectly spherical [66]. These instabilities are seeded by various sources, including low-mode asymmetries in the capsule shape and hohlraum drive, roughness on the surfaces of the ablator, and the fill-tube used to inject the fuel [28]. While great progress has been made in limiting these hydrodynamic instabilities, it is apparent that their further minimization is essential to the success of inertial confinement fusion [67]. A recent ICF experiment on the National Ignition Facility that demonstrated record-breaking neutron yields of 1.7 MJ featured unprecedented implosion metrics, including inferred hot-spot pressures and temperatures [68]. This result demonstrated that the ICF concept is capable of producing a burning plasma for the first time. ICF features both complex hydrodynamics driven by irradiation in the ablation of the fuel capsule, and the evolution of interfacial instabilities and turbulent mixing in an intense radiative environment. As our knowledge of ICF continues to develop, understanding how these radiation-hydrodynamics effects influence these experiments is a crucial ingredient to the success of this promising technology.

1.3 Physical models and approaches

Implying summation over repeated indices, we write a general mixed hyperbolic-parabolic system of partial differential equations with source terms as:

$$\frac{\partial}{\partial t}\mathbf{q} + \frac{\partial}{\partial x_j}\mathbf{f}_j(\mathbf{q},\mathbf{p}) + \mathbf{h}(\mathbf{q}, \frac{\partial \mathbf{q}}{\partial x_j}, \mathbf{p}) = \frac{\partial}{\partial x_j}\mathbf{g}_j(\mathbf{q}, \frac{\partial \mathbf{q}}{\partial x_j}, \mathbf{p}) + \mathbf{s}(\mathbf{q},\mathbf{p}). \tag{1.1}$$

Here, t is the time variable, x_j is the Eulerian spatial coordinate, $\mathbf{q}$ is the state vector, $\mathbf{p}$ is the vector of (constant) parameters explicitly entering the system, $\mathbf{f}_j$ is the divergence-form hyperbolic flux, $\mathbf{g}_j$ is the parabolic flux, $\mathbf{h}$ is the term containing non-conservative products, and $\mathbf{s}$ is the source term.

Here, we refer to $\mathbf{f}_j$ as the divergence-form hyperbolic flux, as it's contribution to (1.1) can be written in vector form as $\nabla \cdot \vec{\mathbf{f}} = \text{div}(\vec{\mathbf{f}})$. A common example of an equation containing a non-conservative product that cannot be written in divergence form is the advection of a material in a flow with velocity u_j, described using the material (i.e., Lagrangian) derivative D/Dt

$$\frac{D}{Dt}q = \frac{\partial}{\partial t}q + u_j \frac{\partial}{\partial x_j}q = 0. \tag{1.2}$$

This equation states that the quantity q moves with the flow. So, we contain products that are first-order in the spatial derivative, yet cannot be written in divergence form, in the vector $\mathbf{h}$, which we refer to as the non-conservative product term.

The vector $\mathbf{p}$ contains parameters specific to the models used to describe the system. A common example would be constants that enter the equation of state or some constitutive model describing the system under consideration.

In this section, we describe physical models that can be written in the form of System (1.1). Here we describe models which apply only to a single fluid, in which the equation-of-state properties are constant and uniform; modeling of multiple fluids will be discussed in detail in Chapter 3 of this dissertation. In Sections 1.3.5 and 1.3.4 we provide high-level discussion of the computational and analytical approaches taken in this dissertation.

1.3.1 Hydrodynamics models

Here we discuss various models for describing fluid flow. We begin with the compressible Euler equations, a system of nonlinear, hyperbolic conservation laws that describe the flow of an inviscid, compressible fluid. We then consider viscosity and heat conduction, ending up with the compressible Navier Stokes equations.

The Euler equations state the conservation of mass, momentum, and energy for a fluid continuum. The assumption of a continuous fluid is typically valid in the

systems of interest due to their density and the length-scales under consideration. The state vector and divergence-form hyperbolic fluxes for this model are

$$\mathbf{q} = \begin{bmatrix} \rho \\ \rho u_i \\ E \end{bmatrix}, \qquad \mathbf{f}_j = \begin{bmatrix} \rho u_j \\ \rho u_i u_j + \delta_{ij} p \\ u_j (E + p) \end{bmatrix}. \tag{1.3}$$

Here ρ is the mass density of the fluid, u_i is the i-th component of velocity of the fluid, p is the pressure of the fluid, and E is the total energy density of the fluid, comprised of internal and kinetic contributions, $E = \rho e + \frac{1}{2}\rho u_i u_i$. For the compressible Euler equations, $\mathbf{h}_j$, $\mathbf{g}_j$, and $\mathbf{s}$ are zero. To close the Euler system of equations, we require a thermodynamic equation of state (EOS) relating the specific internal energy e to the pressure p and density ρ,

$$e = e(\rho, p). \tag{1.4}$$

For instance, the ideal gas equation of state can be used to describe gases,

$$e = \frac{p}{\rho(\gamma - 1)}. \tag{1.5}$$

Here γ is the adiabatic index, or ratio of specific heats. In the case of a single fluid, where γ is constant and uniform, this parameter enters the vector $\mathbf{p}$ in Equation (1.1).

As the compressible Euler equations model inviscid, compressible fluid mechanics, they admit the wave dynamics (e.g., normal and oblique shockwaves, rarefaction waves, contact waves) that are present in fluid flows. The compressible Euler equations is a very useful model in certain limits, when mass, momentum, and energy are transported via wave dynamics. In reality, the transport of momentum and energy of fluids is also affected by internal friction caused by the property of viscosity. Viscosity acts to resist deformation of fluid elements, dissipating kinetic energy to heat. The compressible Navier-Stokes equations is an accurate model for compressible, viscous

fluids and typically includes a term describing heat conduction as well. This model consists of the state vector and hyperbolic fluxes of the compressible Euler equations given by Equation (1.3), additionally modeling the diffusive processes of Fourier heat conduction and Newtonian viscosity by incorporating the divergence of the parabolic flux vector:

$$\mathbf{g}_j = \begin{bmatrix} 0 \\ \tau_{ij} \\ u_i\tau_{ij} - Q_j \end{bmatrix}. \tag{1.6}$$

Here, the viscous stress tensor τ_{ij} and the Fourier heat flux Q_j are given by

$$\tau_{ij} = \mu\big(\frac{\partial u_i}{\partial x_j} + \frac{\partial u_j}{\partial x_i} - \frac{2}{3}\frac{\partial u_k}{\partial x_k}\delta_{ij}\big) + \mu_B\frac{\partial u_k}{\partial x_k}\delta_{ij}, \qquad Q_j = -\kappa\frac{\partial T}{\partial x_j}. \tag{1.7}$$

Here, the dynamic shear viscosity is μ, the bulk viscosity is μ_B, and the thermal conductivity is κ. We require an equation of state relating the specific energy e to the other thermodynamic properties. Following the ideal gas assumption, we may relate the pressure to the temperature via

$$p = \rho R T, \tag{1.8}$$

where the gas constant per unit mass, R, is given in terms of the (universal) gas constant per mole, R_u, by

$$R = \frac{R_u}{M}, \tag{1.9}$$

where the molar mass of the gas is M. Using the ideal gas law, we write the equation of state in terms of temperature and density, $e(\rho, T)$, as

$$e = \frac{p}{\rho(\gamma - 1)} = \frac{R}{\gamma - 1}T = c_v T, \tag{1.10}$$

where c_v is the specific heat at constant volume. Accounting for additional physical

effects upon the fluid involves augmenting the system with further fluxes or source terms. For instance, an external gravitational field with acceleration g_i is represented by adding the source term,

$$\mathbf{s} = \begin{bmatrix} 0 \\ \rho g_i \\ \rho g_i u_i \end{bmatrix}. \tag{1.11}$$

In this case, the entries of the vector g_i are further examples of additional parameters that enter the vector $\mathbf{p}$ in the system (1.1).

1.3.2 Radiation-hydrodynamics models

Here we discuss models for radiation-hydrodynamics flows and the assumptions we make in attaining the model used in this work. In general, this interaction involves two-way coupling, so the energy of the radiation field must be solved for along with the fluid quantities. In particular, we discuss the grey (i.e., single radiation energy) non-equilibrium diffusion radiation hydrodynamics model, derived in Appendix A. We also discuss the limitations of this model, as well as alternative approaches. The state vector and hyperbolic fluxes for this model is:

$$\mathbf{q} = \begin{bmatrix} \rho \\ \rho u_i \\ E \\ E_R \end{bmatrix}, \qquad \mathbf{f}_j = \begin{bmatrix} \rho u_j \\ \rho u_i u_j + \delta_{ij}(p + p_R) \\ u_j(E + p) \\ u_j(E_R + p_R) \end{bmatrix}. \tag{1.12}$$

These are the hyperbolic fluxes for the compressible Euler equations, with the addition of an equation transporting the radiation field energy density E_R and the fluid pressure in the momentum equation augmented by the radiation pressure p_R. For an isotropic radiation field, the radiation pressure is given in terms of the radiation energy by $p_R = \frac{1}{3}E_R$. This assumption is discussed at length in Appendix A, and

is valid in the presence of a sufficiently dense fluid. Here E is the total energy density comprised of internal and kinetic contributions of the fluid, $E = \rho e + \frac{1}{2}\rho u_i u_i$. In the radiation-hydrodynamics case, the fluid may be ionized such that E consists of contributions from both ion and electron species. In this work, we use a 'single fluid' approach that assumes that the mass, momentum, and energy of the ion species dominates that of the electron species, so that E is dominated by the internal and kinetic energy of the ion fluid. This is discussed in greater detail later in this section.

In radiation hydrodynamics, the radiation field and material interact through different mechanisms. One such mechanism is in the work done on the flow by the radiation field, which is represented by the non-conservative products in the vector:

$$\mathbf{h} = \begin{bmatrix} 0 \\ 0 \\ u_j \frac{\partial}{\partial x_j} p_R \\ -u_j \frac{\partial}{\partial x_j} p_R \end{bmatrix}. \tag{1.13}$$

Additionally, we model the transport of photons using the diffusive radiative flux,

$$\mathbf{g}_j = \begin{bmatrix} 0 \\ 0 \\ 0 \\ F_{R,j} \end{bmatrix}, \tag{1.14}$$

where the radiation diffusion model, discussed at length in Appendix A, models the radiative flux as

$$F_{R,j} = D_R \frac{\partial}{\partial x_j} E_R, \tag{1.15}$$

where the diffusion coefficient is given as

$$D_R = \frac{c}{3\kappa_R}. \tag{1.16}$$

Here the Rosseland mean opacity κ_R governs the diffusion of photons throughout the system. As described in in Appendix A, the radiation diffusion model results from the assumption that the radiation field is isotropic, which is true in optically thick systems where the photon mean-free path is very small. In the case where this model is used in an optically thin system, significant modeling issues occur. As radiation diffusion models result in an unbounded flux in the case of free-streaming radiation, flux limiters are often employed to ensure that the magnitude of the radiative flux is at most $F_R = cE_R$ by modifying the diffusion coefficient [69, 70, 71]. This *ad hoc* fix increases the robustness of codes based on radiation diffusion, ensuring that physical results are attained in both the diffusion and free-streaming limits. Here we employ the radiative flux limiter of Morel [72],

$$D_R = \frac{c}{\sqrt{(3\kappa_R)^2 + (\frac{1}{E_R}\frac{\partial E_R}{\partial x_j})^2}}. \tag{1.17}$$

We observe that as $\kappa_R \to 0$, F_R is bounded to a magnitude of cE_R. In the limit where κ_R is large, D_R approaches the diffusion form in Equation (1.16). While flux-limited diffusion causes the correct solution to be attained in the optically thick and optically thin limits, it is not appropriate in systems with intermediate values of optical depth. Furthermore, in optically thin regions, the radiative flux will be non-zero in any direction where the gradient of radiative energy density is negative, i.e., the radiative flux will act to diffuse radiative energy from regions of high energy to regions of low energy. This means that, in two and three spatial dimensions, the flux limited diffusion approach cannot follow shadows (regions of low radiative energy density where free-streaming radiation should not reach due to an intervening optically-thick object)

and may even result in calculation of a net force in the wrong direction from the unidirectional irradiation of optically thick bodies [73]. Therefore, it is important that the limitations of the flux-limited diffusion model be recognized, and that the model not be employed to solve problems where these limitations are influential. Methods exist that do not rely on the assumption of isotropy, such as variable Eddington tensor [74], discrete ordinates [75] and Monte Carlo [76] methods. These methods typically involve solving for directionally-dependent distribution functions, such as the specific intensity in Equation (A.2), rather than moment quantities derived in Section A.1.2, and as a result are typically much more computationally expensive.

Finally, the radiative source term drives the energies of the radiation field and the material to equilibrium in a local sense via photoabsorption and emission processes:

$$\mathbf{s} = \begin{bmatrix} 0 \\ 0 \\ -S_R \\ S_R \end{bmatrix}. \tag{1.18}$$

Where the source is given as,

$$S_R = c\kappa_P(E_R - B), \tag{1.19}$$

where B is the frequency-integrated Planck intensity evaluated at the material temperature T, $B = a_R T^4$, where a_R is the radiation constant. Thus the Planck mean opacity κ_P governs the local equilibration of the radiation field and the fluid.

Typically, one would model the opacities κ_R and κ_P using data obtained from experiment or an atomic-level calculation. In general, they are functions of the density and temperature of the fluid: $\kappa_P = \kappa_P(\rho, T)$ and $\kappa_R = \kappa_R(\rho, T)$. This model for grey radiation involves the solution of radiative quantities that have been integrated

over frequency. The opacities used here are calculated by averaging the absorption coefficient in some sense over the frequency spectrum, as given in Equations (A.35) and (A.37). In some systems, the absorption coefficient may vary significantly over frequency. Figure 1.4 shows an example of the dependence of the absorption coefficient on photon energy as a function of temperature. The absorption coefficient can vary significantly over small ranges of photon energy, particularly near the bound-free absorption edge (Carbon's K-edge) which occurs at 283 eV. If this variation is

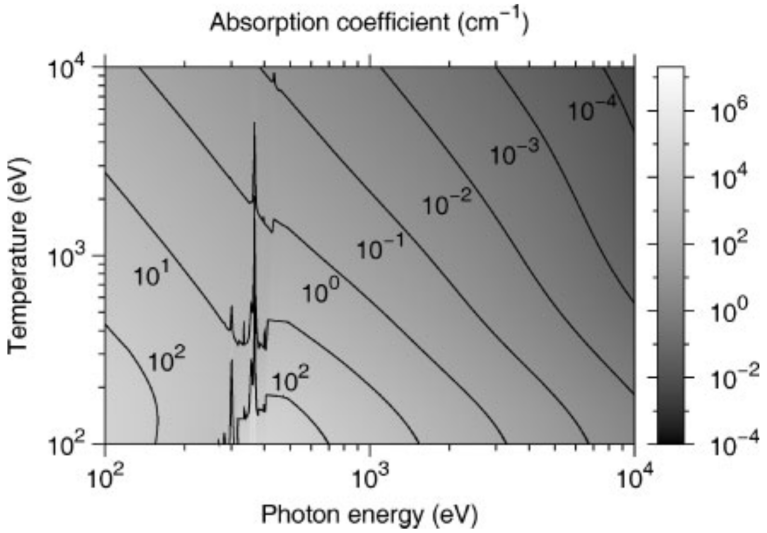

Figure 1.4: Spectral dependence of the absorption coefficient of carbon with a density of 2.2 g/cm^3, as a function of temperature. Reproduced with permission from Hau-Riege [77].

significant in spectral regions where the radiation transport is significant, as often occurs for non-Planckian radiation fields, the use of a single averaged value to describe transport in this region may be insufficient. In these systems the grey approximation is inadequate, and some model that provides spectral resolution of the unknown radiation quantities should be used instead. In Appendix A, we derived the multi-group model, which is one such model. However, solving for the many unknowns required for multi-group calculations can be expensive, though methods for improving the cost of the multi-group model have been proposed [78].

We note that we can combine the material and radiation energies to derive a conservation energy for the total energy:

$$\frac{\partial}{\partial t}(E + E_R) + \frac{\partial}{\partial x_j}\left[u_j(E + E_R + p + p_R)\right] = \frac{\partial}{\partial x_j}F_{R,j}. \tag{1.20}$$

In general, one would need to consider both electron and ion energies as unknowns, replacing the equation governing material total energy density in Equations (1.12) with separate equations for these two fluid species [79, 80, 81]. In such a model, the electron fluid exchanges energy with the radiation field via the source term, and the two species are coupled by a term depending on the ion-electron collision rate and the difference between the temperatures of the two species. As the mass of a proton is approximately 1,836 times that of an electron, the mass of the ion fluid is much greater, even in the case of a fully ionized gas of an element of high atomic number. As we are concerned with inertially dominated flows in which ions are the important participant, we use a 'single-fluid' approach considering only momentum transport due to the ion species. Therefore, we assume that the ion pressure (and internal energy density) dominates, and so we solve an equation for the total material energy density as a whole, where the internal energy of the material is that of the ion species. Including the source term S_R in this equation effectively implies the ions and electrons are instantaneously coupled in our model. As the plasmas considered in this work are non-magnetized, we consider them to be quasi-neutral and neglect Coulomb interactions within the plasma. These assumptions greatly simplify the equation of state of the fluid; as the ion species is essentially a monatomic gas, it is valid to consider the ideal gas law for pressure, Equation (1.5), and for temperature, Equation (1.10), where the molar mass is $M = Am_pN_A/(\mathcal{Z} + 1)$, where A is the atomic mass, m_p is the mass of a proton, N_A is Avogadro's number, and the average ionization is $\mathcal{Z}$. An example of where this assumption may break down is in certain

types of radiative shocks [82, 83].

One may also include other multiphysics effects in these models. In applications where thermal conduction is important, one may include a heat flux term in the parabolic flux vector in Equation (1.13) to model the conductive heat transport of free electrons. This term is added similarly to that in the compressible Navier-Stokes viscous fluxes in Equation (1.6). Many codes utilize the classic Spitzer-Harm [84] form for electron conductivity of a collisional plasma. Similar to the case of radiation diffusion, this result is only valid in a highly collisional, dense plasma. As the system departs from this ideal, the streaming speed given by this treatment increases without bound. Various approaches have modified the conductivity with flux limiters in past studies [79, 85, 86] to limit the streaming speed to a physically sensible value. Highly collisional plasma flows or flows that are turbulent may also require modeling of viscosity of the ion species. Various models exist for the viscosity of high-energy-density plasmas [87, 88] and viscous stress terms can be added to the parabolic fluxes for the momentum and material energy in Equations (1.14), similar to the compressible Navier-Stokes viscous fluxes in Equation (1.6).

1.3.3 Dimensional analysis

In multi-physics problems where multiple competing physical processes are being modeled, it is often useful to non-dimensionalize the governing equations. This allows one to study physical regimes through non-dimensional parameters and assess the relative importance of the physical processes being considered. In some cases, this allows one to neglect certain processes and simplify the equations. Additionally, dimensional analysis allows the comparison of phenomena at different scales, as non-dimensionalization reveals dimensionless parameters that, when their values are similar, imply some physical similarity between systems at very different scales [89]. First we will demonstrate this process on the compressible Navier-Stokes equations,

with state vector and hyperbolic fluxes given by Equation (1.3) and parabolic fluxes given by Equation (1.6).

Selecting an appropriate scale length L, a sound-speed scale a_0 (giving a time-scale $\tau = L/a_0$), and a scale density ρ_0, we define the non-dimensional independent variables $x'_j = x_j/L$ and $t' = t/\tau$, as well as the non-dimensional dependent variables $\rho' = \rho/\rho_0$, $u'_j = u_j/a_0$, $p' = p/(\rho_0 a_0^2)$, $E' = E/(\rho_0 a_0^2)$, and $T' = T/T_0$, where $T_0 = a_0^2/c_v$. Multiplying the conservation of mass equation by $L/(\rho_0 a_0)$, we obtain

$$\frac{\partial}{\partial t'}\ \rho' + \frac{\partial}{\partial x'_j}(\rho' u'_j) = 0. \tag{1.21}$$

Next, we multiply the balance of momentum equation by $L/(\rho_0 a_0^2)$,

$$\frac{\partial}{\partial t'}\ \rho' u'_i + \frac{\partial}{\partial x'_j}\left[\rho' u'_i u'_j + p'\delta_{ij}\right] = \frac{\partial}{\partial x'_j}\left[\frac{1}{Re_\mu}\left(\frac{\partial u'_i}{\partial x'_j} + \frac{\partial u'_j}{\partial x'_i} - \frac{2}{3}\frac{\partial u'_k}{\partial x'_k}\delta_{ij}\right) + \frac{1}{Re_{\mu_B}}\frac{\partial u'_k}{\partial x'_k}\delta_{ij}\right]. \tag{1.22}$$

Here $Re_\mu = \rho_0 a_0 L/\mu$ is the Reynolds number based on the dynamic viscosity and $Re_{\mu_B} = \rho_0 a_0 L/\mu_B$ is the Reynolds number based on the bulk viscosity. Multiplying the conservation of energy equation by $L/(\rho_0 a_0^3)$

$$\frac{\partial}{\partial t'}\ E' + \frac{\partial}{\partial x'_j}u'_j(E'+p') = \frac{\partial}{\partial x'_j}\left[\frac{u'_i}{Re_\mu}\left(\frac{\partial u'_i}{\partial x'_j} + \frac{\partial u'_j}{\partial x'_i} - \frac{2}{3}\frac{\partial u'_k}{\partial x'_k}\delta_{ij}\right) + \frac{u'_i}{Re_{\mu_B}}\frac{\partial u'_k}{\partial x'_k}\delta_{ij} + Fo_T\frac{\partial T'}{\partial x'_j}\right]. \tag{1.23}$$

Here the thermal Fourier number is $Fo_T = \alpha_T \tau/L^2$, where the thermal diffusivity is $\alpha_T = \kappa/(\rho_0 c_v)$. The non-dimensional energy equation can also be written in terms of the thermal Péclet number, $Pe_T = La_0/\alpha_T$. The non-dimensional numbers that emerge are each a ratio of different physical processes present in the compressible Navier Stokes equations. For example, the Reynolds numbers are a ratio of inertial forces to viscous forces (from dynamic/bulk viscosity) within the fluid flow. In the case of a very large Reynolds number, the respective viscous term can be neglected. The thermal Fourier number is the ratio of time scales associated with thermal conduction

to that associated with the storage of thermal energy by increasing internal energy in the flow. Similarly, the Péclet number is the ratio of time scales associated with advection to that associated with thermal conduction. In the case of a small thermal Fourier number (or large thermal Péclet number), the thermal conductivity term can be neglected. If viscosity and heat transport are neglected, we are left with the compressible Euler equations, in which inertial effects are the only means of momentum and energy transport.

A similar procedure allows us to analyze the different regimes in the radiation-hydrodynamics equations. We follow the convention in [90], and non-dimensionalize the hydrodynamic quantities using the previous scale quantities L, a_0, ρ_0, and define the non-dimensional variables x'_j, t', ρ', u'_j, p', E', as in the hydrodynamic case. We non-dimensionalize the radiation quantities using $T_0 = a_0^2/(R\gamma)$, and the radiation constant a_R: $E'_R = E_R/(a_R T_0^4)$, $p'_R = p_R/(a_R T_0^4)$, and $F'_{R,j} = F_{R,j}/(c a_R T_0^4)$. Using this non-dimensionalization, the equation of state in terms of pressure becomes,

$$e' = \frac{p'}{\rho'(\gamma - 1)}, \tag{1.24}$$

and in terms of temperature,

$$e' = \frac{T'}{\gamma(\gamma - 1)} = c'_v T', \tag{1.25}$$

The non-dimensionalization of the conservation of mass equation is the same as in the compressible Navier-Stokes case, yielding Equation (1.21). We multiply the momentum equation by $L/(\rho_0 a_0^2)$,

$$\frac{\partial}{\partial t'}\ \rho' u'_i + \frac{\partial}{\partial x'_j}\left[\rho' u'_i u'_j + (p' + \frac{1}{\mathcal{R}} p'_R)\delta_{ij}\right] = 0. \tag{1.26}$$

Here $1/\mathcal{R} = a_R T_0^4/(\rho_0 a_0^2)$ is the radiation density ratio. This quantity indicates the

relative importance of the energy densities (or, roughly, the pressures) of material versus the radiation field in the radiation hydrodynamic system. We multiply the conservation equation for total energy given in Equation (1.20) by $L/(\rho_0 a_0^3)$,

$$\frac{\partial}{\partial t'}\left(E' + \frac{1}{\mathcal{R}}E'_R\right) + \frac{\partial}{\partial x'_j}u'_j\left(E' + \frac{1}{\mathcal{R}}E'_R + p' + \frac{1}{\mathcal{R}}p'_R\right) = Bo\frac{\partial}{\partial x'_j}F'_{R,j}. \tag{1.27}$$

Here the Boltzmann number $Bo = ca_R T_0^4/(\rho_0 a_0^3)$ is a ratio of radiative energy flux to the energy flux due to hydrodynamic motion.

These dimensionless parameters enable us to define the regimes of radiation hydrodynamics. Considering air at atmospheric conditions, taking a_0 as the sound speed, $1/\mathcal{R} \approx 4 \times 10^{-11}$ and $Bo \approx 3 \times 10^{-5}$. Clearly, in this case, all terms associated with the radiation field can be neglected, recovering the Euler equations as given in Equation (1.3). Indeed, radiation-hydrodynamics phenomena do not occur at terrestrial conditions. Both of these numbers scale positively with temperature, so the regimes of radiation hydrodynamics tend to occur at higher than atmospheric temperatures. For non-relativistic flows, Bo is significantly larger than $1/\mathcal{R}$. For this reason, as temperature increases, values of Bo near unity while those of $1/\mathcal{R}$ are orders of magnitude smaller. This situation is known as the radiative flux regime, and in this case all terms multiplying $1/\mathcal{R}$ in Equations (1.26) and (1.27) may be neglected, while the radiative flux term multiplying Bo must be included. As temperature increases still, eventually both dimensionless numbers are large enough that none of the terms in Equations (1.26) and (1.27) may be neglected. This situation is known as the radiation-dominated regime. This concept is illustrated in Figure 1.5, where the solid lines indicate where radiation energy fluxes become equivalent to those associated with the hydrodynamic motion, and the dashed lines indicate where radiation energy densities/pressures become equivalent to those of the fluid. We observe that at lower densities lower temperatures are required to transition in radiation hydrodynamics

regimes. The radiation dominated regime is only attained, at ordinary gas densities, at temperatures above about 100 eV (1,160,452 K). The computational approach taken in this work is applicable to the radiation-dominated regime, so may be used in the most general radiation-hydrodynamic systems.

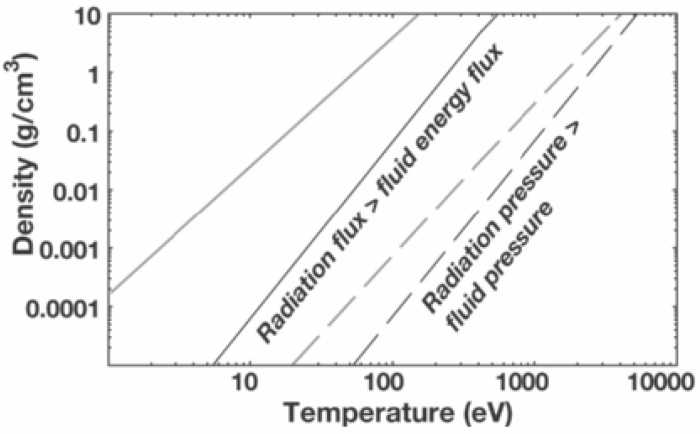

Figure 1.5: Regimes of radiation hydrodynamics, gray curves are for Xenon and black curves are for CH plastic. Reproduced with permission from Drake [63].

While it is illustrative to non-dimensionalize the total energy equation in considering the regimes of radiation hydrodynamics, in reality we solve separate energy equations for material and radiation energy densities, with state vector and divergence-form hyperbolic fluxes given in Equation (1.12) and non-conservative products, parabolic fluxes, and source terms given by (1.13), (1.14), and (1.18), respectively. We non-dimensionalize the material energy equation as we did the total energy equation, introducing the non-dimensional variables $\sigma'_P = cL\kappa_P/a_0$, and $B' = B/(a_R T_0^4)$. Multiplying the material energy equation by $L/(\rho_0 a_0^3)$,

$$\frac{\partial}{\partial t'}\ E' + \frac{\partial}{\partial x'_j} u'_j(E' + p') + \frac{1}{\mathcal{R}} u'_j \frac{\partial}{\partial x'_j} p'_R = -\frac{1}{\mathcal{R}} \sigma'_P (B' - E'_R). \tag{1.28}$$

We now non-dimensionalize the radiation energy equation, introducing the non-dimensional variables $D'_R = c/(3\kappa_R L a_0)$ and $\sigma'_P = (c/a_0)\kappa_P L$. Multiplying the mate-

rial energy equation by $L/(a_0 a_R T_0^4)$,

$$\frac{\partial}{\partial t'}\ E'_R + \frac{\partial}{\partial x'_j} u'_j (E'_R + p'_R) - u'_j \frac{\partial}{\partial x'_j} p'_R - \frac{\partial}{\partial x'_j} D'_R \frac{\partial}{\partial x'_j} E'_R = \sigma'_P (B' - E'_R). \tag{1.29}$$

These are the equations we solve in practice, and that we refer to as the non-dimensionalized non-equilibrium diffusion radiation-hydrodynamics equations. With flux-limited diffusion, where the diffusion coefficient is given by (1.17), the non-dimensional diffusion coefficient is given instead by,

$$D'_R = (c/a_0) / \sqrt{(3\kappa_R L)^2 + (\frac{1}{E'_R} \frac{\partial E'_R}{\partial x'_j})^2}. \tag{1.30}$$

This modification of the diffusion coefficient ensures that a mathematically sensible value of the radiative flux is obtained in the diffusion (optically thick) and free-streaming (optically thin) limits.

We note that when solving these non-dimensional equations, one must specify the ratios $1/\mathcal{R} = a_R T_0^4/(\rho_0 a_0^2)$ as well as c/a_0. The speed of sound in air at 10 eV, a typical temperature in HED systems, is approximately 6,800 m/s, while the speed of light is approximately 3.0 $\times 10^8$ m/s. The value of this ratio depends on the value chosen for a_0, but values of $c/a_0 \sim 10^2 - 10^6$ are reasonable in HED systems. For smaller values, relativistic effects should be considered, meaning that the governing equations given here are insufficient. One also needs to define $\kappa_R L$, $\kappa_P L$. As we discuss in Appendix A, the opacity κ_R is related to the mean-free path in the material. So, the non-dimensional quantity $\kappa_R L$ is a measure of the optical depth of the system. For small values of $\kappa_R L$, the system is optically thin, and for large values, the system is optically thick. Many references note that near boundaries between materials, the opacity may become small and the system may become optically thin [25, 63, 91]. The formulation in Equation (1.30) ensures that the proper radiative flux value is obtained in optically thin and thick regions. However, this scenario involves a transition, and at some point

the optical depth will be on the order of unity. In this region, the use of flux-limited diffusion is subject to serious modeling errors.

1.3.4 Sensitivity analysis

Oftentimes, the values of inputs into mathematical models are not known to a high degree of certainty. In this situation, statistical distributions are useful for representing the likelihood of an input attaining a certain value. When such models are used to make predictions, those outputs are subject to uncertainty as well. As some model predictions may be only as useful as they are accurate, it is important to be able to constrain the uncertainty in modeling outputs that result from uncertainties in specific inputs. Additionally, this may motivate efforts to place tighter constraints on certain model inputs. Sensitivity analysis is an important practice in the field of uncertainty quantification, wherein values of parametric sensitivities constrain the uncertainty of model output due to uncertainty present in those parameters [92]. Sensitivity analysis has been employed in fields as diverse as biomedical engineering [93], geophysics [94], chemical kinetics [95], and finance [96] in order to determine the effect of changes in model parameters upon model solutions.

A physical system can be modeled mathematically (e.g., the system (1.1)) using equations relating the vector of dependent variables $\mathbf{q}$, defining the state of the system, to the model parameters or inputs $\mathbf{p}$, which contains model parameters and perhaps initial and/or boundary conditions of the system, and the independent variables $\mathbf{x} = (t, x_j)$, which in general includes spatial and/or temporal coordinates. This model is generally comprised of some number of equations (for example, each system described in Sections 1.3.1 and 1.3.2), written concisely as

$$\mathbf{H}(\mathbf{q}(\mathbf{x}), \mathbf{p}(\mathbf{x}), \mathbf{x}) = 0. \tag{1.31}$$

Here $\mathbf{H}$ is a vector operator whose elements may consist of algebraic equations, differential operators, integro-differential operators, or any combination/convolution thereof. In general, sensitivity analysis concerns some vector of response quantities of interest, $\mathbf{R}(\mathbf{q}(\mathbf{x}), \mathbf{p}(\mathbf{x}))$, which typically only depends on $\mathbf{p}$ implicitly through Equation (1.31). There exist a number of approaches to sensitivity analysis, including differential analysis [97], variance decomposition methods [98], and Monte Carlo methods [99]. Differential sensitivity analysis is chiefly concerned with the determination of the sensitivities of response quantities to the various model parameters $\frac{\partial \mathbf{R}}{\partial \mathbf{p}}$. In Chapter 2 of this dissertation, we apply sensitivity analysis to systems in which intense radiation sources drive blow-off flow and generate impulse in metals.

1.3.5 High-order numerical methods

Experiments in HED science are expensive to conduct, as well as difficult to design and diagnose. It is common that the process of designing experiments requires that certain quantities be predicted or estimated. Due to the expense and difficulty of implementing preliminary proof-of-concept experiments, these predictions often cannot be determined from previous experiments. Analytical prediction can be especially difficult in this field, as the system is governed by complex multi-physics processes. An additional limitation in HED experiments is that it is often possible to obtain measurement of only limited quantities during experiments due to diagnostic limitations.

Computational simulation can be useful for addressing each of these issues; simulations are often used to predict quantities for experimental design, and to match measured quantities from experiments and extract others that could not be accessed. Simulations provide a relatively inexpensive tool that offer unlimited detail of the entire evolution the system while accounting for all relevant physical processes. Additionally, simulations can be used to explore the effects of certain physical processes

systematically in a way that typically cannot be done with experimental methods.

In general, governing model equations, such as the general system (1.1), are discretized using numerical methods that approximate their solution. A given numerical method has an associated error and order of accuracy, which means that the error by some measure scales as Error $\sim \Delta x^{\mathrm{OA}}$, where Δx is the size associated with the numerical discretization and OA is the order of accuracy. High-order numerical methods are defined as having second-order accuracy or greater. Higher order methods converge at a higher rate of accuracy, meaning that they generally obtain a lower error with a given discretization. This means that high-order methods, in general, obtain a certain level of error with fewer calculations, and are in general less expensive [100]. Due to this advantage, high-order numerical methods are particularly attractive for applications where low-order methods would require prohibitively high resolutions. One such application is in the direct numerical simulation (DNS) of turbulent flows, where every physically relevant length and time-scale is resolved, including those due to the small-scale motions responsible for turbulent dissipation [101].

Despite this advantage, most computational studies in industry as well as research environments is done with methods that are at most second-order accurate. This tendency is especially true in HED science, where the application of high-order methods has been particularly limited. High-order methods tend to be more complicated, more difficult to implement, and more difficult to analyze than low-order methods. Another advantage of low-order methods is robustness, i.e., the ability to produce stable and useful results for a wide range of problems. Additionally, increasing the order of accuracy typically increases the computational stencil and the communication requirements of the implementation, which can cause a bottleneck during parallel execution. Another issue is that high-order interpolation of discontinuities, such as shockwaves and material interfaces, causes oscillations, which need to be damped by either introducing dissipation through artificial viscosity [102] or limiting the values

of the high-order representation [103].

In Chapter 3, we introduce a high-order numerical method for computing flows in radiation hydrodynamics. Our method is based on the discontinuous Galerkin (DG) discretization, which uses high-order polynomials to approximate the solution within each computational element. Because these polynomials are supported (i.e., defined to be nonzero) only in their corresponding element, the computational stencil for the DG approach is compact. This means that the numerical treatment of fluxes only requires communication between immediately adjacent elements, allowing for minimal latency due to communication during computation on parallel architectures. We apply this method to multi-material flows that interact with intense radiation fields according to the models described in Section 1.3.2. It is our hope that by showcasing the advantages of this method, we will demonstrate the potential usefulness that high-order methods offer in HED science.

1.4 Dissertation overview

This dissertation introduces analytical and computational techniques useful for studying flows in radiation hydrodynamics. We address two important gaps in knowledge that exist in the currently available techniques used to describe radiation/material interaction. The objectives of this work are (i) to develop a modeling approach for predicting the impulse and uncertainty in impulse in materials irradiated by x-ray sources subject to uncertainty, and (ii) to develop an approach for numerical simulation of multi-material radiation hydrodynamics suitable for the study of mixing at material interfaces.

Towards this first objective, Chapter 2 introduces a data-driven semi-analytical model for studying systems in which deposited energy from intense radiation sources causes surface material to blow off, driving motion of the remaining bulk material. The model we present is useful for predicting the impulse imparted to a material

by a given radiation spectrum. Furthermore, our model provides the sensitivity of this impulse to the spectrum, allowing uncertainty in impulse to be constrained given the uncertainty present in a measured radiation spectrum. Our modeling approach is novel, and allows reliable prediction of impulse and impulse-spectrum sensitivity using a relatively small set of data. While we use high-fidelity simulations to obtain this data, experimental measurements can be used as well.

We address the second objective in Chapter 3, where we introduce a numerical method for computational investigation of multi-material flows in radiation hydrodynamics. Based on the DG discretization, our method is high-order accurate, physically consistent at material interfaces, and conserves total energy. We use an interface-capturing approach via a high-order limiting scheme that is designed to prevent pressure and temperature errors at interfaces. We apply this limiting procedure in a solution-adaptive fashion using a physics-based discontinuity sensor. Our scheme offers promising advantages for parallel computation of phenomena occurring at material interfaces in radiation hydrodynamics, which are a key aspect of HED science. The extension of these types of high-order interface capturing schemes to the field of radiation hydrodynamics is novel, and hopefully will provide a basis for wider use of high-order schemes in the field of HED science.

In Chapter 4, we summarize this dissertation and the impact of its contributions. Additionally, we discuss limitations of the approaches employed herein, and make suggestions for future work.

CHAPTER II

Analytical Modeling of Radiatively-Generated Impulse in Materials [1]

2.1 Abstract

High-intensity x-ray sources are used for a variety of purposes in HED physics. Additionally, many engineering applications involve exposing materials to a high fluence of radiation. Absorption of these x-rays heats the material, causing an increase in pressure and driving material to blow off/ablate, imparting impulse to the bulk material. Accurately modeling the physical processes involved in radiatively-driven impulse in materials is challenging, as the material behavior is governed by complex material opacity, constitutive, and equation of state relations. Analytical models for radiatively-generated impulse in materials exist, but contain an unclosed term that must be either modeled or fit using data. Additionally, uncertainties present in the measurement of the detailed spectra of x-ray sources give rise to uncertainties in the generated material impulse. We present a semi-analytical model for the impulse-spectrum sensitivity, which governs the relationship between these uncertainties and is especially useful for performing forward propagation of uncertainty. We use high-fidelity simulations in which the modeling parameters have been selected to fit data

[1] This chapter was released by Lawrence Livermore National Laboratory as LLNL-TH-835682.

from experiments of impulse generated by x-rays on the National Ignition Facility to provide data for closure of the model for a few example materials. We also verify our model for impulse-spectrum sensitivity by comparison to brute-force calculation of sensitivity with this simulation approach. We then perform uncertainty propagation using this sensitivity model to demonstrate the utility of this methodology in the design of robust experiments.

2.2 Introduction

Significant progress has been made over the past few decades on the development of high-intensity x-ray sources on facilities such as the Z machine at Sandia National Laboratories [104], the Omega laser at the Laboratory for Laser Energetics [105], and the National Ignition Facility (NIF) at Lawrence Livermore National Laboratories [106]. Many experiments in HED physics [55, 107] and inertial confinement fusion [108, 109] have used high-intensity x-ray sources to drive hydrodynamic flows of interest. Furthermore, x-ray sources are often used as probes and backlighters for radiography in plasma experiments [110, 111]. Many applications also require materials to withstand large doses of irradiation, including the design of vehicles and equipment for space travel [112, 113], the design of detectors in high-energy physics [114], and the design of military communications systems [115]. Additionally, past studies have focused on the response of planetary and meteorite materials to x-ray irradiation to study the origin and evolution of the universe [116] and develop strategies for near-Earth object impact hazard mitigation [117]. In these application areas, an accurate representation of the radiation and material physics is essential to predicting the impulse generated by a given radiation source.

As photons interact with a material, photoabsorption and inelastic scattering deposit energy in the material as determined by the material's opacity and the spectral intensity of the x-ray source corresponding to the photons' frequency [118]. The

energy deposited contributes to phase change, ionization, or may increase the internal energy of solid material. An increase in internal energy corresponds to a pressure increase dictated by the material's equation of state. Energy that goes into phase change of the material or ionization acts to create liquid, gas, or plasma, causing material to expand from, or blow off of, the bulk material, imparting impulse and sending a compressive wave that travels both directions, the primary wave moving into the bulk of the material. The resulting stresses may surpass the yield strength of the material, resulting in strain or even failure. Additionally, as the compression wave interacts with the front and rear surfaces of the bulk material, it reflects a tensile wave that may cause solid material to fail in tension and fragment from the bulk material. Past studies have attempted to model impulse generated by x-ray irradiation using purely analytical methods, but due to the complicated nature of the energy deposition mechanisms, analytical models include a term describing the final energy of the blown-off material, a quantity that is generally unknown [119]. Prior modeling efforts have arbitrarily set this term as the enthalpy of fusion or vaporization of the material [120], or modeled this term from thermodynamic considerations that rely on fixing the final state of the material [119]. In this work, we employ a data-driven approach to fit an assumed functional form for this quantity, resulting in a fully specified model for a given material that can be used for predictive calculation of impulse.

The Dante is a diagnostic with 18 filtered channels used in HED experiments to measure spectrally-resolved x-ray fluxes [121]. Dante systems are commonly used in HED experiments and are currently in use at the Omega laser facility [122] and the NIF [123], with a similar system in use by the French Atomic Energy Agency [124]. X-ray spectral measurements using the Dante diagnostic are subject to uncertainties, including those due to shot-to-shot variation [125] and the algorithm used to unfold the raw data into detailed spectra [126]. In modeling radiatively-generated impulse

in materials, uncertainty in the various model inputs, or parameters, (e.g., the initial state of the material, parameters entering the constitutive relationships governing the material, and the x-ray spectrum) result in uncertainty in the prediction of impulse. We are interested in constraining the uncertainty in impulse that is due to uncertainties in the source spectrum, a problem which we address using sensitivity analysis, which was introduced in Section 1.3.4. In this study, we are concerned with differential sensitivity analysis, which uses various approaches to determine the values of the derivatives of model outputs with respect to model parameters, such as direct differentiation of the governing model [92], Green's functions [127], and brute-force model recalculation combined with finite differences [128]. Herein, we use this first approach as our chief means of studying this quantity, and the last approach as a means of verification and comparison.

In the current chapter of this dissertation, we develop a semi-analytical approach to modeling the impulse-spectrum sensitivity of x-ray irradiated materials. First, we establish context by describing an experimental platform for studying radiatively-generated impulse in materials in Section 2.3. We will use data from these experiments that characterize the x-ray source and material response in this work. Next, our model is derived directly from the Bethe, Bade, Averell and Yos (BBAY) impulse model [129] in Section 2.4. The model contains a term describing the energy of the blown-off material, which is not known *a priori*. We use results from high-fidelity 1-D simulations with sophisticated photon transport, equation of state, and constitutive models described in Section 2.5 to provide a data-driven representation of this term. We employ a procedure that calibrates parameters used in these simulations to achieve close agreement to experimental data. Our methodology of fitting coefficients in an assumed functional form for the blown-off material energy given this data from simulations is described in Section 2.6. Our model allows for predictive calculation of impulse as well as impulse-spectrum sensitivity, enabling the propagation of uncer-

tainty associated with the x-ray spectrum to constrain the resulting uncertainty in impulse. We apply our methodology to two different irradiated materials, verifying the results of our model using brute-force sensitivity evaluations directly from the 1-D simulations in Section 2.7. In Section 2.8, we demonstrate the application of the model, constraining the uncertainty in material impulse using estimates of uncertainty in x-ray spectrum due to shot-to-shot variation. The authors believe that the approach outlined in this work will prove useful in the design of robust experiments studying x-ray impulse generation in a range of materials given x-ray sources subject to uncertainty in spectral content from a variety of sources.

2.3 Experiments of radiatively-driven impulse

An experimental platform for studying material response to intense x-ray sources is under development at the NIF [130, 131, 132]. These experiments examine the response of various materials to exposure to different x-ray sources heated and ionized by the NIF laser beams, each emitting radiation in a different characteristic spectrum. In this work, we consider results obtained with a Xenon gas pipe x-ray source, which has been characterized in prior experiments [133]. The emission spectrum of the x-ray source is measured by the Dante diagnostic. A detailed spectrum is obtained from the 18-channel Data data using the UNSPEC unfold algorithm [126]. A target positioner holds the x-ray source equidistant in the line-of-sight of an array of material samples held by the X-ray Transport and Radiation Response Assessment (XTRRA) test cassette, shown in Figure 2.1 [131]. This apparatus holds multiple material samples as they are exposed to a given x-ray source in a manner that enables the samples to be recovered after the conclusion of the experiment. The apparatus also houses instruments for diagnostic measurements characterizing the mechanical responses of the samples during the experiment. As x-rays are absorbed by the material samples and material blow-off occurs, a compression wave is driven into the remaining bulk of

the material. The time history of the displacement of the rear surfaces of the material samples caused by interaction with the compression wave is measured by Photon Displacement Interferometry (PDI), which uses interference between incoming and outgoing light waves to measure small displacements [134]. The PDI measurements indicate the temporal shape of the compression wave, which displaces the rear surface over a relatively short time as it interacts with the rear of the sample.

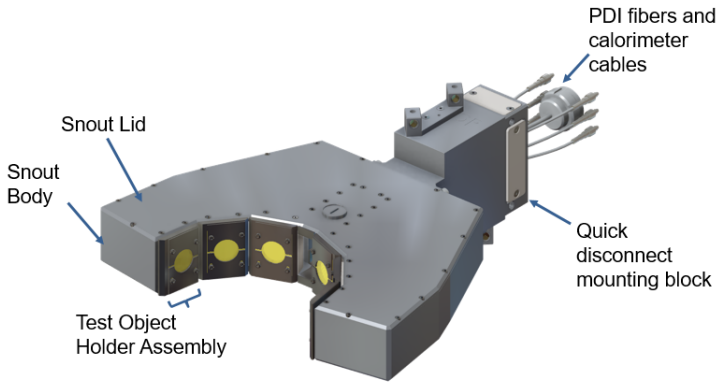

Figure 2.1: The XTRRA test casette used in radiatively-driven impulse experiments on the NIF. The Test Object Holder Assembly windows contain the material samples, which are exposed to x-ray emissions from a source material held within the snout equidistant in the line-of-sight of each sample.

In our treatment of this problem, we rely on a few key assumptions. In these experiments, the duration of the x-ray source is on the order of nanoseconds, whereas bulk hydrodynamic motion is on the order of a tenth of a microsecond, as seen in the simulation results in Section 2.5.1. These disparate time scales justify the approach of treating radiation transport and hydrodynamics in a sequential fashion, which both our simulation and modeling approaches rely upon. As the Dante diagnostic measures source emission along a different axis than that seen by the material samples, it is assumed throughout this work that the source is isotropic in spectral shape. Additionally, the small diameter (3.0 cm) of the material samples relative the distance to the source (10 cm) means that the distance to the source at the edges of the samples

is less than 5% larger than at the center of the samples, so the variation in fluence from one point to another across the face of a sample is negligible. This means that blow-off is driven uniformly across the face of the sample. The samples have a large aspect ratio, and are larger in diameter than in thickness (0.05 cm for Ti-64, 0.20 cm for Al-6061). A signal will traverse the thickness 30 times for Ti-64, and 7.5 times for Al-6061 before a signal from the boundary will travel to the middle of the sample. Signals resulting from effects at the sample boundaries are thus unlikely to affect the sample interior before the compression wave reaches the rear surface of the sample. It is therefore reasonable to use one-dimensional simulations to represent the hydrodynamics. The results in Section 2.5.2 indicate that these assumptions are appropriate.

2.4 Impulse-spectrum sensitivity model

As described in Section 1.3.4, a physical system can be modeled mathematically using equations relating the vector of dependent variables $\mathbf{q}$, defining the state of the system, to the model parameters or inputs $\mathbf{p}$, including model parameters and perhaps initial and/or boundary conditions of the system, and the independent variables $\mathbf{x}$. As we are primarily interested in the damage caused to materials in radiative environments, we define our response quantity of interest, $\mathbf{R}(\mathbf{q}(\mathbf{x}), \mathbf{p}(\mathbf{x}))$, as the impulse imparted to the material. Throughout this study, we restrict ourselves to 1-D slabs of material that are initially uniform. We also assume that exposure to radiation occurs over a time-scale much smaller than that associated with the material response. In this case, impulse is an integral quantity that characterizes the amount that the blown-off material 'pushes' on the remaining bulk material due to the radiation-deposited energy. The impulse imparted to a continuous material can be defined by integrating the momentum over the slab or the pressure at the blow-off/bulk material boundary over time, so long as the integration time far exceeds the time associated

with blow-off:

$$I = \int_{m_B}^{M} u(m, t = \tau)\mathrm{d}m = \int_{0}^{\tau} p(m = m_B, t)\mathrm{d}t, \tag{2.1}$$

where u is the material velocity, p is the material pressure, t is time, τ is a time-scale associated with bulk material motion, m is the 1-D Lagrangian coordinate,

$$m = \int_{0}^{x} \rho_0(\tilde{x}, t)\mathrm{d}\tilde{x}, \tag{2.2}$$

M is the initial mass of the slab of material and m_B is the value of the Lagrangian coordinate corresponding to the blow-off/bulk material interface. Here ρ_0 is the initial density of the slab, which we assume to be uniform, and x is the Eulerian coordinate in the slab. A hierarchy of analytical models have been developed to calculate radiation-generated impulse [135]. Perhaps the most sophisticated is the BBAY model, written for a 1-D slab of material as [129]:

$$I = \alpha\Big[2\int_{0}^{m_B}\big[E(m) - E_f(m)\big]m\mathrm{d}m\Big]^{1/2}. \tag{2.3}$$

In Equation (2.3), $E(m)$ is the initial energy deposited by x-rays within the slab, $E_f(m)$ is the final internal energy distribution of the blown-off material, α is a coefficient of integration, and m_B is the coordinate where $E = E_f$. The BBAY model (2.3) is a closed-form solution of the equations of motion; we derive this expression in Appendix B. α is a constant, here assumed to be $\alpha = \sqrt{2}$. Assuming that photoabsorption is the dominant mechanism of energy deposition, and that the mass absorption coefficient $\mu(e)$, dependent on photon energy e, is uniform within the slab, we can write the initial energy deposition as:

$$E(m) = \int_{-\infty}^{\infty} f(e)\mu(e)\exp\left[-\mu(e)m\right]\mathrm{d}e, \tag{2.4}$$

where the spectral fluence of the incident x-ray field is $f(e)$, with dimensions of energy per unit area per unit photon energy. The total fluence is given by

$$F = \int_0^\infty f(e)\mathrm{d}e. \tag{2.5}$$

In practice, we approximate the x-ray spectrum of the source using piecewise-constant values within G number of groups with photon energy $e \in [e_g, e_{g+1}]$. This practice is commonly performed to simplify the frequency dependence of material and unknown radiation quantities [25, 91]. Using this approximation, the fluence of the g-th group is computed as:

$$F_g = \int_{e_g}^{e_{g+1}} f(e)\mathrm{d}e. \tag{2.6}$$

In this case, we approximate the energy deposition with the expression

$$E(m) = \sum_{g=1}^{G} F_g \mu_g \exp\left[-\mu_g m\right], \tag{2.7}$$

where μ_g is the mass absorption coefficient averaged over the g-th group.

We utilize the BBAY model (2.3) to derive an analytical expression for the impulse-spectrum sensitivity. The derivative of the expression for energy deposition in Equation(2.4) with respect to the fluence of group g is,

$$\frac{\partial E}{\partial F_g} = \mu_g \exp\big[-\mu_g m\big], \tag{2.8}$$

Evaluating the functional derivative of the BBAY impulse model (2.3), and making use of (2.8), we evaluate the sensitivity of impulse with respect to the fluence of group g:

$$\frac{\delta I}{\delta F_g} = \frac{\alpha^2}{I} \int_0^{m_B} \mu_g \exp\big[-\mu_g m\big] \Big[1 - \frac{\partial E_f}{\partial E}\Big] m\mathrm{d}m. \tag{2.9}$$

As we evaluate the impulse-spectrum sensitivity using numerical methods, we refer to this model as semi-analytical.

As the function $E_f(m)$ is not known *a priori*, this term must be modeled. One such effort is the McCloskey-Thompson model [119], which assumes that the blow-off material isentropically expands to the triple point pressure and temperature. This is a mathematically convenient, albeit arbitrary, state at which to fix the final energy of the material. This model has been used to investigate trends in impulse dependence on x-ray fluence in experiments [136, 137, 138]. More sophisticated models for $E_f(m)$ tend to have material parameters that are difficult to obtain experimentally [119], and so may require individual calibration, which we prefer to avoid. Instead, we use data from simulations using high-fidelity transport and constitutive models to obtain a functional form for $E_f(m)$, as will be discussed in Section 2.5. To verify this analytical expression, we compare this semi-analytical model for impulse-spectrum sensitivity to that evaluated by brute-force model reevaluation using finite differences with simulations in Section 2.5.1.

2.5 Obtaining data to model $E_f(m)$ function

Our approach to closure of Equations (2.3) and (2.9) involves using data from simulations to fit an assumed analytical form of the function $E_f(m)$, described in Section 2.6. In the current section, we describe our methodology for conducting these simulations. We outline our computational approach in Section 2.5.1. In Section 2.5.2 we describe our process of calibration, which allows us to achieve good agreement between simulation and experiment. This process allows us to use a data-driven approach for informing the function $E_f(m)$, which enables our semi-analytical model for the impulse as well as the impulse-spectrum sensitivity to be used to predict quantities with a high degree of fidelity.

2.5.1 Computational approach

Our computational approach involves the use of two simulation codes ran in succession, each simulating a different set of the physics of radiatively-driven blow-off and impulse generation. We use the Mercury Monte Carlo particle transport code [139] to calculate the radiation energy deposited in materials exposed to intense sources of radiation. The Mercury code is capable of computing transport of neutrons, photons, and light elements with multigroup or continuous interaction cross-sections. Our photon transport calculations include 3×10^6 marker particles with interaction cross-sections from the Evaluated Nuclear Data Library [140]. The Monte Carlo approach enables us to account for the effect of coherent scattering with reasonable computational cost. Though this effect is negligible at solid densities, this strategy enables us to extend our approach to examine lower-density systems of interest. We use time-integrated emission spectra, as measured by the Dante diagnostic during radiatively-generated impulse experiments described in Section 2.5.2, to define the source of photons in the simulations. An example of a time-integrated spectrum measured from a Xenon source is shown in Figure 2.2a. As can be observed, unfolding the Dante data with the UNSPEC algorithm results in fairly complex emission spectra. The Monte Carlo simulations provide profiles of the internal energy deposited within the material, initializing the internal energy in the hydrodynamics simulations we conduct with the Ares code. The profile of energy deposited by the spectrum shown in Figure 2.2a within a Ti-64 sample is shown in Figure 2.2b. Absorption of radiation from this source results in an energy deposition profile that is monotonically decreasing, as expected, and most of the energy is concentrated in the leading ~ 10 μm of the sample.

We utilize the Ares code [141] to simulate the 1-D hydrodynamic response to the energy deposition profile calculated by Mercury. Ares is an Arbitrary Lagrangian-Eulerian hydrodynamics code with a variety of equations of state and constitutive

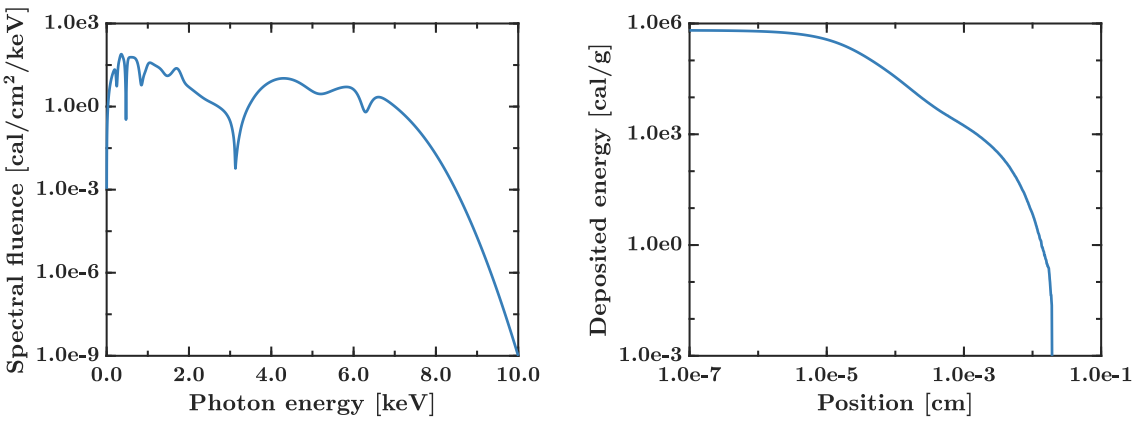

Figure 2.2: Mercury Monte Carlo photon transport code input and output. (a) Input: time-integrated emission spectrum from a Xenon source measured by Dante, re-scaled to 100 cal/cm^2. (b) Output: resulting profile of internal energy deposition within a 1-D slab of Ti-64.

models for a diverse array of materials. The Livermore Equation of State (LEOS) library contains tabulated equation of state data for a large variety of materials [142, 143]. Additionally, experimentally-determined parameters for equation of state and constitutive models such as the Steinberg-Guinan [144] and Steinberg-Lund [145] constitutive models for metals, the Jones-Wilkins-Lee equation of state for high explosives [146], and the Mie-Gruneisen equation of state for shock-compressed solids [147] are stored in the Steinberg-Guinan Equation of State (SGEOS) database [148]. Appropriate equations of state and constitutive data allow us to perform simulations that model the details of the material blow-off, impulse generation, and compression wave propagation to a high degree of fidelity. Figure 2.3 shows momentum and pressure profiles of the compression wave propagating through a 0.05 cm slab of Ti-64 computed by Ares, resulting from the energy deposition profile shown in Figure 2.2b. The figures show a compression wave of fairly complex shape that evolves as it propagates through the sample, reaching the rear surface of the 0.05 cm thick sample around 7 $\times 10^{-2}$ μs. The shape of this compression wave determines how the rear surface is displaced by the wave, as recorded with PDI data in the experiments described

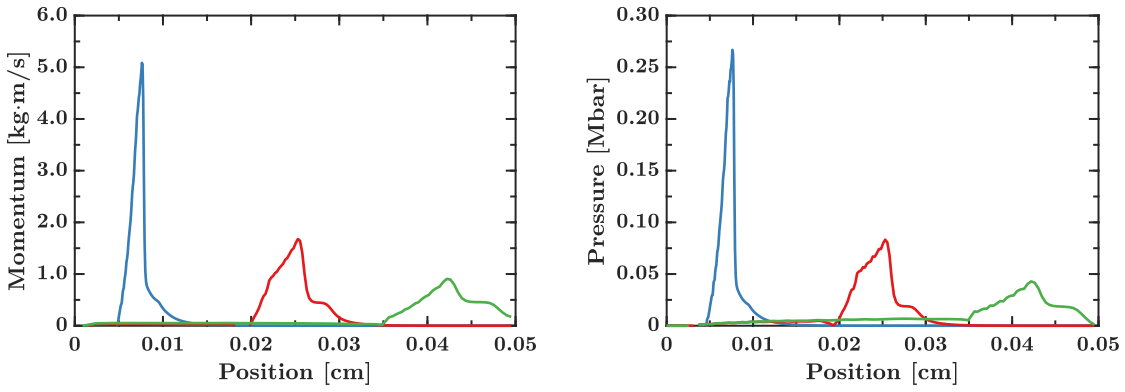

(a) (b)

Figure 2.3: Ares hydrodynamics code output, showing profiles of (a) momentum and (b) pressure from a 1-D simulation of a 0.05 cm Ti-64 slab exposed to radiation from a Xenon source. Profiles depict the propagation of a compression wave through the material at 1×10^{-2} μs (blue), 4×10^{-2} μs (red), 7×10^{-2} μs (green).

in Section 2.3. We note that both of these quantities, momentum and pressure, can be used to calculate the sample impulse with Equation (2.1). We model the Ti-64 with the LEOS and the Steinberg-Guinan constitutive model with material-specific parameters given by the SGEOS database. We utilize experimental data to calibrate the values of parameters not specified by these models, relating to the material's failure in tension, in Section 2.5.2.

2.5.2 Calibration of simulation model parameters

We first compare the PDI data from the NIF experiments to the computational results. A Lagrangian tracer in the Ares simulations tracks the displacement of the sample rear surface as the compression wave interacts with it for comparison to the PDI data. Obtaining agreement with the experiment allows us to fix values of parameters entering Equation (1.31) relating to material properties, so that the sensitivity of the impulse with respect to the radiative spectrum can be assessed. As the rear surface displacement depends on the shape of the compression wave, we find that the displacement results are highly sensitive to the material equation of state and con-

stitutive treatment, and agreement with experimental data was only possible using the most sophisticated models available. In this work, we consider a 0.2 cm thick Al-6061 sample and a 0.05 cm thick Ti-64 sample exposed to a Xenon x-ray source. We describe these materials with the LEOS equation of state and the Steinberg-Guinan constitutive model in the case of Ti-64, while we find that the Johnson-Cook constitutive model [149] gave better agreement for Al-6061. Nominal values for parameters entering these models from the literature are used [148, 150]. We follow a calibration procedure to determine quantities characterizing mechanical failure in tension, i.e., the minimum pressure p_{min} and the minimum compression η_{min} that can be withstood by the material. In this section, we describe the procedure used to determine the values of these parameters that result in the best agreement with the PDI data.

First, we conduct simulations sweeping the parameter space, varying p_{min} and η_{min} within a range to assess the agreement of simulated rear surface displacement to that measured in experiments. This process allows us to assess whether a unique point exists in the parameter space for which good agreement is achieved. For these simulations, the Dante-measured time-integrated Xenon spectrum in Figure 2.2a is used. Integrating this spectrum over frequency, the fluence delivered to each sample is found to be 69 cal/cm^2. Rear-surface displacement Δx for varying η_{min} and p_{min} (measured in Mbar) are shown in Figures 2.4 and 2.5. As the compression wave interacts with the rear surface, the displacement increases suddenly, and then coasts at a constant velocity afterward. The prompt displacement, or the amount that the displacement increases initially, is a direct function of the impulse generated in the sample. So, it is very important that our simulations capture the prompt displacement accurately. As Figures 2.4 and 2.5 show, the shape of the PDI time histories during the prompt displacement and coasting periods are fairly sensitive to the values of these parameters. These results show that for both materials, the best agreement is attained for $\eta_{min} = 0.85$ and p_{min} values below -0.03 Mbar.

We further calibrate the values of η_{min} and p_{min} to agree with the experimental data using the minimization algorithm of Powell [151] implemented in the Python `SciPy` library [152]. We also allow the fluence to vary, to account for uncertainty in the fluence seen by each sample. This uncertainty is due in part to our assumption of isotropy between the Dante and the sample viewing axes, as discussed in Section 2.3. For both materials, we use the initial guesses of η_{min}=0.85, p_{min}=-0.04 Mbar, and a fluence of 69 cal/cm^2. We restrict the optimization to allow η_{min} to vary in the range [0.8,0.9], p_{min} in the range [-0.03,-0.05] Mbar, and the fluence to vary only by 10% of the initial guess. The initial guesses and range used for η_{min} and p_{min} were selected due to the agreement with experimental data shown in Figures 2.4 and 2.5. The range for the fluence was selected as a reasonable zeroth-order estimate for the uncertainty in the total fluence seen by the samples. We calculate the relative error in rear-surface displacement, defined as

$$\text{Relative error} = \left| \frac{\Delta x_{\text{Ares}} - \Delta x_{\text{PDI}}}{\Delta x_{\text{PDI}}} \right|. \tag{2.10}$$

The relative error is assessed at times when displacement is output by Ares, and the PDI data is linearly interpolated between points to these times. The Powell minimization routine minimizes the L_2 norm of the relative error, computed as

$$L_2 = \sqrt{\frac{1}{N} \sum_{i=1}^{N} [\text{Relative error}]_i^2}, \tag{2.11}$$

where N is the number of times in the displacement time-history where the relative error is assessed. The results in Figure 2.6 show that in the Ti-64 case, we achieve an $L_2 = 0.0245$ after 54 optimization iterations, where the values are: $\eta_{min} = 0.849$, $p_{min} = -0.300$ Mbar, and 62.7 cal/cm^2. Figure 2.7 shows the Al-6061 case, where we achieve an L_2=0.142 after 33 optimization iterations, where the values are: η_{min}

= 0.846, p_{min} = -0.450 Mbar, and 75.9 cal/cm^2. The figures indicate that we attain reasonable agreement in both cases, with the relative error (excluding initial times, where error is large in both cases) staying under 10% and 15% in the Ti-64 and Al-6061 cases, respectively.

This calibration fully constrains the material parameters to be used in simulations of radiative generation of impulse for both Ti-64 and Al-6061, allowing us to conduct simulations in which the sample pressure loading, blow-off process, and compression wave propagation are accurate to those observed in experiments, and so we may be confident of the impulse values we calculate from our simulation approach. This result is important because impulse calculated from these simulations will be used to obtain coefficients in a functional form assumed for the $E_f(m)$ function appearing in our models for impulse and impulse-spectrum sensitivity in Section 2.6. The process of calibrating the simulations to agree with experimental data allows us to inform our model with quality data, enabling the model to be used for predictive calculation of impulse and impulse-spectrum sensitivity by those designing experiments.

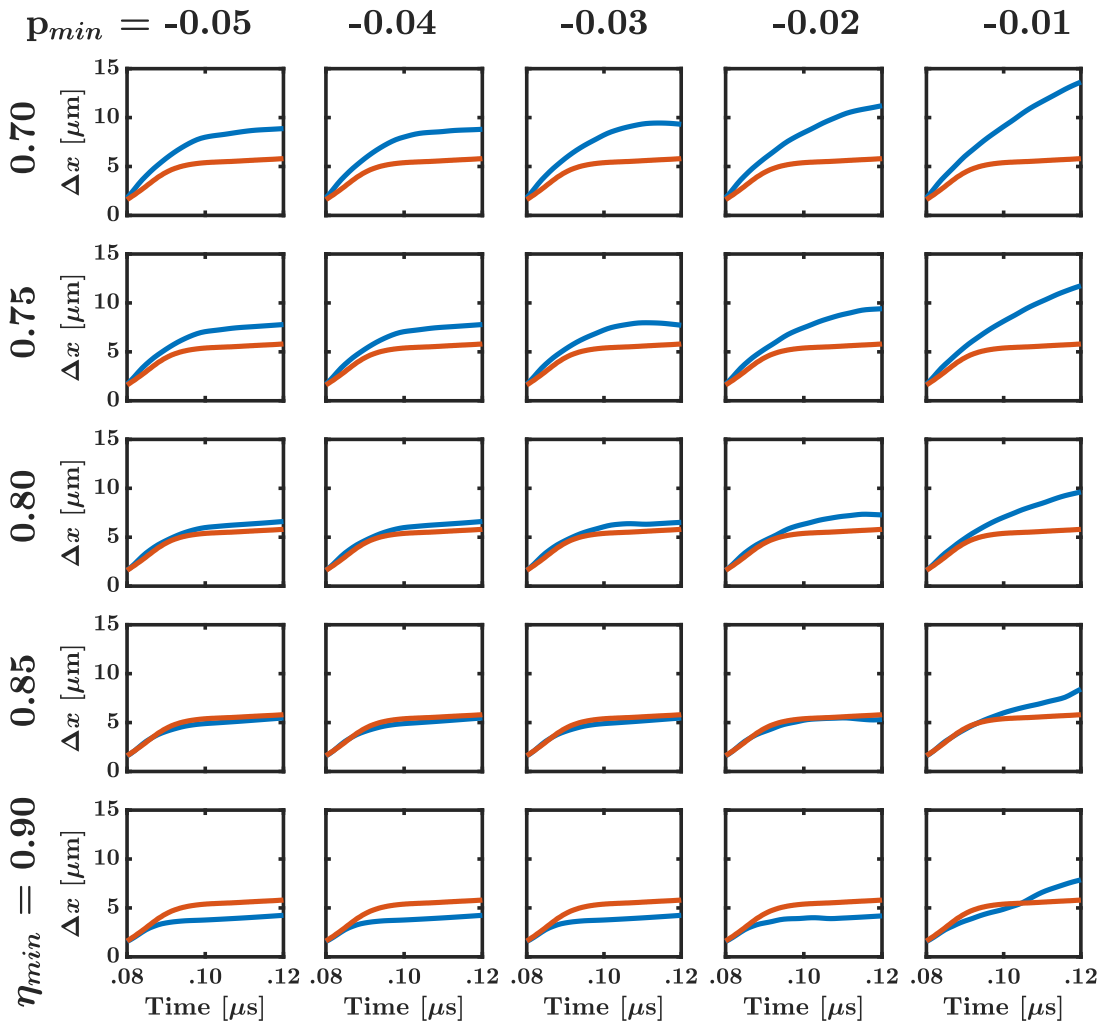

Figure 2.4: Experimental displacement Δx time history from PDI data (red) and Lagrangian tracer from Ares simulations (blue). Tiles show sweep varying values of p_{min} and η_{min} for Ti-64 sample irradiated by a Xenon source at a fluence of 69 cal/cm^2.

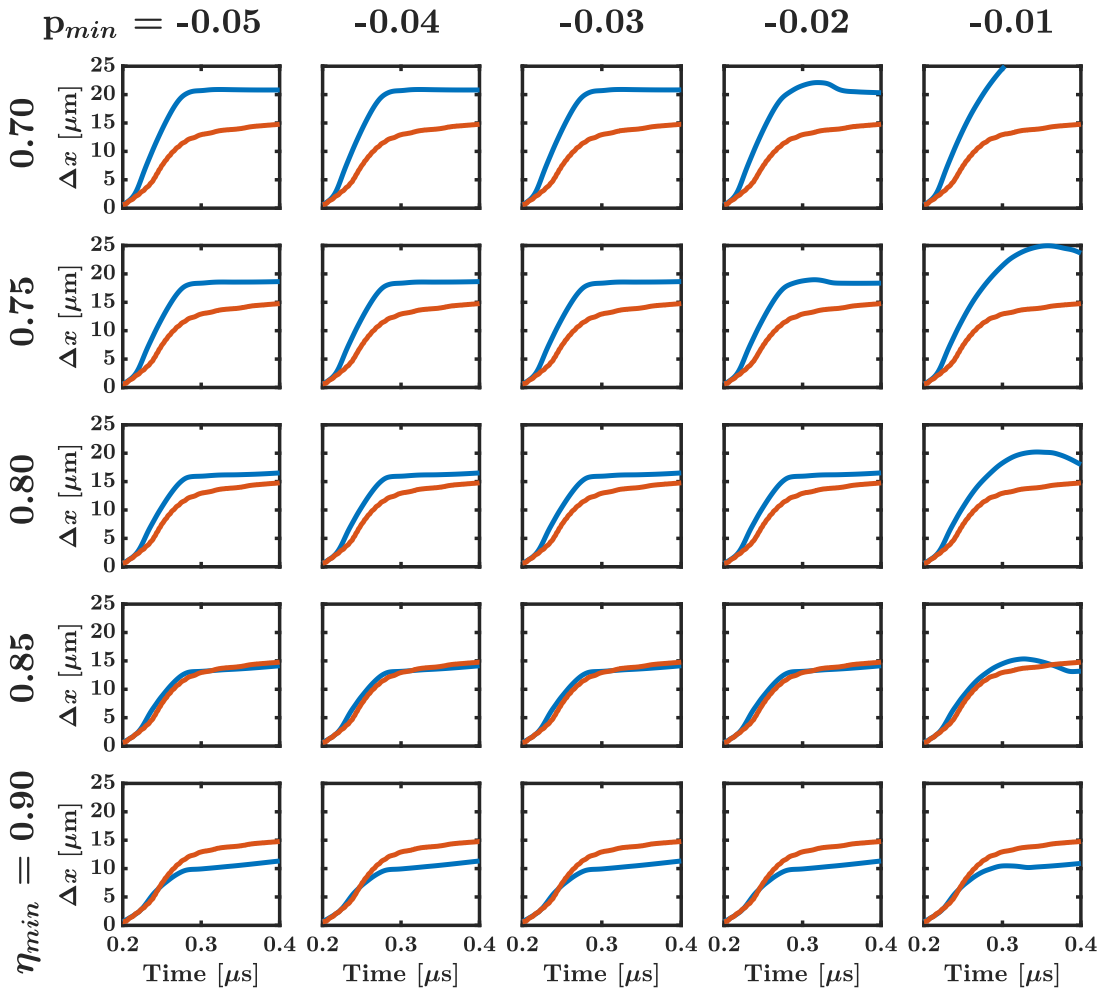

Figure 2.5: Experimental displacement Δx time history from PDI data (red) and Lagrangian tracer from Ares simulations (blue). Tiles show sweep varying values of p_{min} and η_{min} for Al-6061 sample irradiated by a Xenon source at a fluence of 69 cal/cm^2.

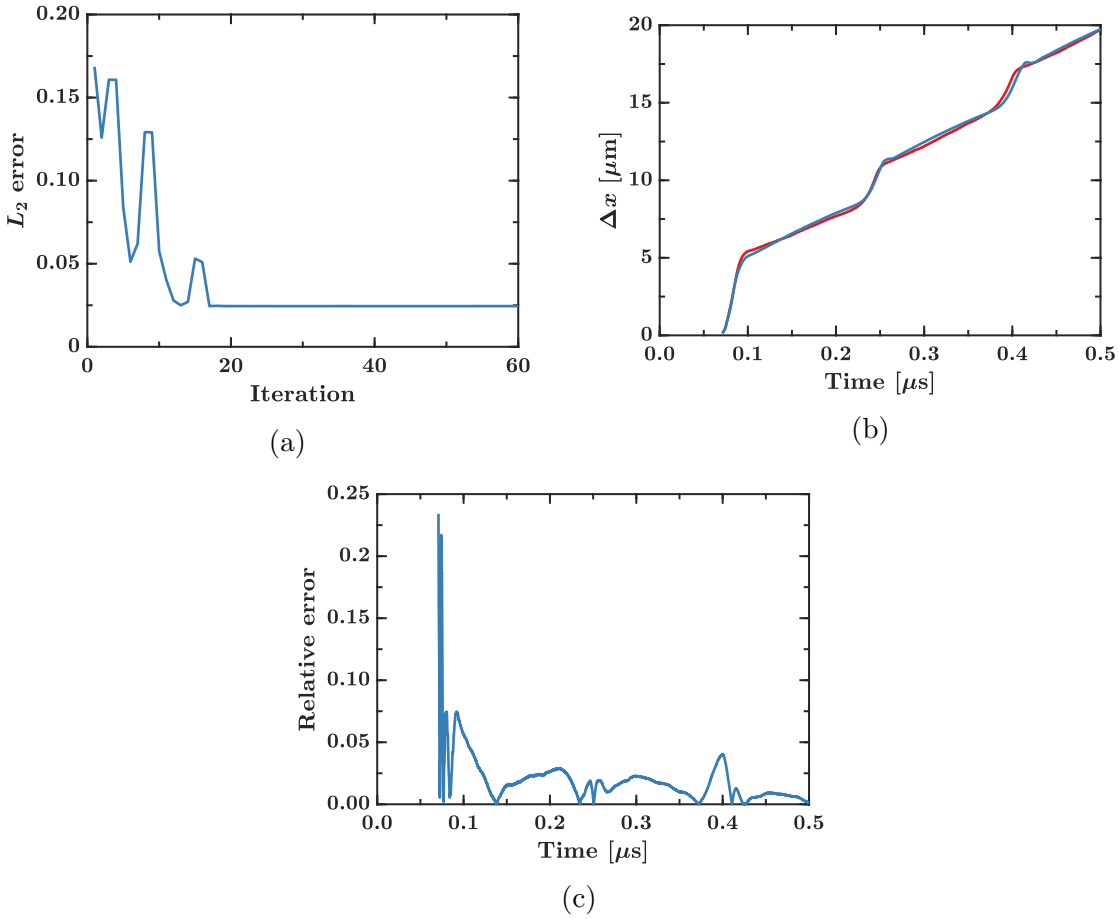

Figure 2.6: Optimization results for Ti-64 sample. (a) L_2 error norm of the relative error over optimization iterations, minimum occurs after 54 iterations. (b) Displacement Δx time-history from PDI data (blue) and Lagrangian tracer from Ares simulation (red) corresponding to the minimal error. (c) Relative error in displacement for simulation corresponding to minimal error.

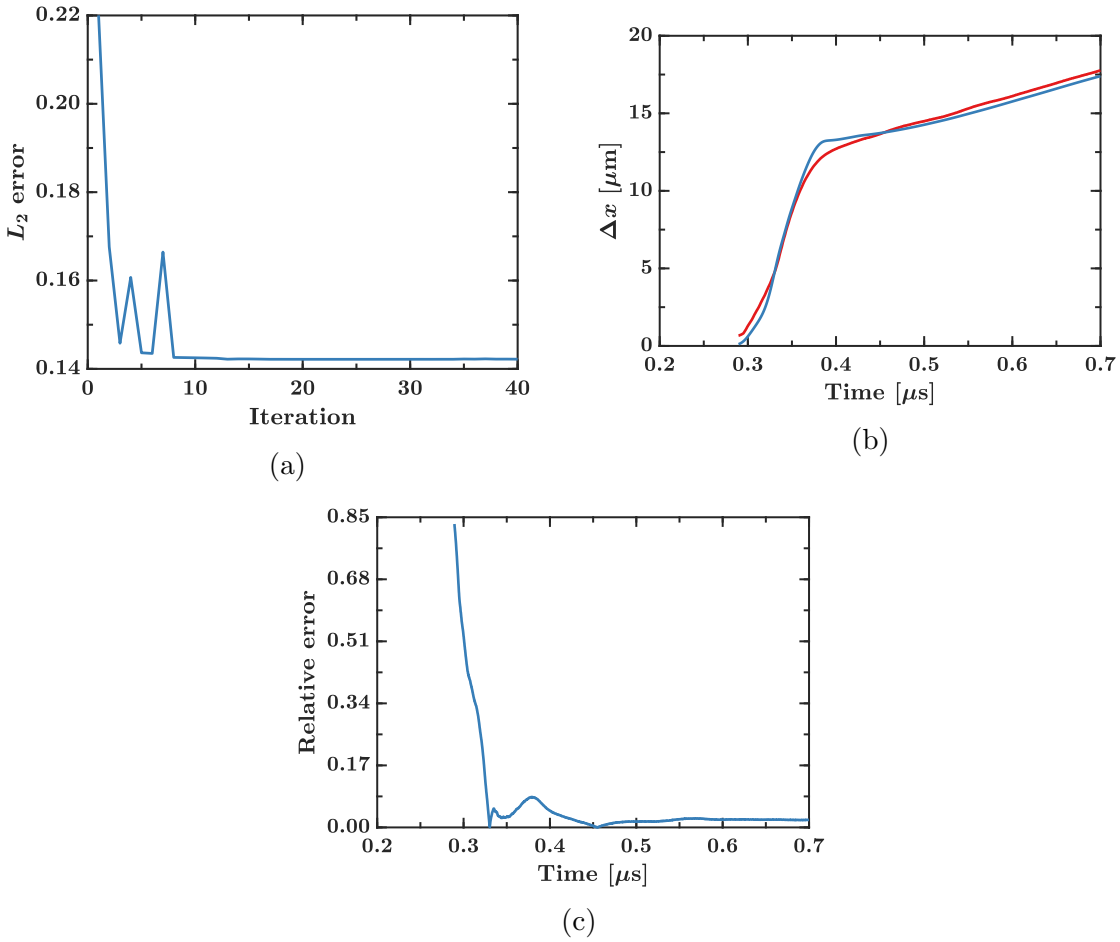

Figure 2.7: Optimization results for Al-6061 sample. (a) L_2 error norm of the relative error over optimization iterations, minimum occurs after 33 iterations. (b) Displacement Δx time-history from PDI data (blue) and Lagrangian tracer from Ares simulation (red) corresponding to the minimal error. (c) Relative error in displacement for simulation corresponding to minimal error.

2.6 Data-driven model for $E_f(m)$ function

We utilize data from the simulation approach described in Section 2.5 to perform a least-squares fit for an assumed functional form of $E_f(m)$. We use the approach described in [119], in which it is assumed that the final blow-off energy can be written as an expansion of the initial deposited energy,

$$E_f(m) = E_f(E(m)) = \sum_{j=0}^{q} c_j [E(m)]^j. \tag{2.12}$$

We now describe our methodology for computing the coefficients c_j. Assume a set of n points of impulse-fluence data (F_i, I_i) for a given source and material, generated via experiment or simulation. In particular, we evaluate the impulse as given by the momentum integral in (2.1) from the simulations described and optimized in Section 2.5 for Ti-64 and Al-6061 exposed to a Xenon x-ray source. We scale the Xenon spectrum shown in Figure 2.2a to different fluences to generate the points (F_i, I_i). Here the initial energy deposition profile for the i-th data point is denoted $E_i(m)$. For each of these data points, we equate two different forms of (2.3),

$$\int_0^{m_i(\mathcal{E}_i)} [E_i(m) - \mathcal{E}_i]\, m\mathrm{d}m = \int_0^{m_i(E_0)} [E_i(m) - E_f(E_i(m))]\, m\mathrm{d}m, \tag{2.13}$$

where $\mathcal{E}_i$ is a constant choice for E_f that forces (2.3) to be equal to I_i. Our implementation uses the bisection method [153] to determine $\mathcal{E}_i$. Here $m_i(\mathcal{E}_i)$ and $m_i(E_0)$ are the Lagrangian coordinate where $E_i(m)$ becomes equal to $\mathcal{E}_i$ and E_0, respectively. E_0 is the zeroth coefficient of the expansion (2.12), i.e., $c_0 \equiv E_0$. As the extent of integration of the right-hand side of Equation (2.13) is $m(E_0)$, E_0 must be treated as

a known quantity. Rearranging, we have

$$\int_0^{m_i(E_0)} E_f(E_i(m))m\mathrm{d}m = \int_{m_i(\mathcal{E}_i)}^{m_i(E_0)} E_i(m)m\mathrm{d}m + \mathcal{E}_i\frac{[m_i(\mathcal{E}_i)]^2}{2}. \tag{2.14}$$

Given that $c_0 \equiv E_0$ is known, we can write:

$$\sum_{j=1}^{M} c_j \int_0^{m_i(E_0)} [E_i(m)]^j m\mathrm{d}m = \int_{m_i(\mathcal{E}_i)}^{m_i(E_0)} E_i(m)m\mathrm{d}m + \frac{1}{2}\Big\{\mathcal{E}_i\left[m_i(\mathcal{E}_i)\right]^2 - E_0\left[m_i(E_0)\right]^2\Big\}. \tag{2.15}$$

For ease of notation, we define the quantities,

$$M_{ij} = \int_0^{m_i(E_0)} \left[E_i(m)\right]^j m\mathrm{d}m, \tag{2.16}$$

$$b_i = \int_{m_i(\mathcal{E}_i)}^{m_i(E_0)} E_i(m)m\mathrm{d}m + \frac{1}{2}\Big\{\mathcal{E}_i\left[m_i(\mathcal{E}_i)\right]^2 - E_0\left[m_i(E_0)\right]^2\Big\}. \tag{2.17}$$

Substituting (2.12) into (2.14), we have the linear system, applying over $i = 1, ..., n$, $j = 1, ..., q$:

$$M_{ij}c_j = b_i \tag{2.18}$$

As $n > q$, this system is over-constrained. We use the standard least-squares method [154] to calculate the vector c_j, which minimizes the quantity $||b_i - M_{ij}c_j||_2$, the Euclidean norm of the residual vector. This vector is:

$$c_j = (M_{ji}M_{ij})^{-1}M_{ji}b_i. \tag{2.19}$$

We note that the choice of E_0 is not important, as long as it is a small enough value that the integration on the right-hand-side of (2.13) is performed over a sufficient portion of the energy deposited: we use the value $E_0 = .001 \times E_{melt}$, where E_{melt} is

Sample	c_1	c_2/E_0	c_3/E_0^2
Ti-64	9.715×10^{-1}	-2.820×10^{-8}	1.474×10^{-15}
Al-6061	9.211×10^{-1}	-2.871×10^{-8}	8.266×10^{-15}

Table 2.1: Nondimensional coefficients of $E_f(m)$ expansion obtained using least-squares method with data from simulations.

the enthalpy of fusion for the material: E_{melt} = 286 J/g for Ti-64 and 380 J/g for Al-6061 [155].

To provide the data for this procedure, we scale the Dante-measured spectrum shown in Figure 2.2a to $m = 5$ fluence values linearly spaced from 100-500 cal/cm^2 and conduct simulations described in Section 2.5 using those spectra. We measure the impulse of the material in the simulation using the momentum integral in Equation (2.1), defining the blow-off/bulk interface coordinate m_B considering material melted at some point in the simulation as blow-off. The coefficients resulting from the least-squares procedure using this procedure are given in Table 1, non-dimensionialized by the value of E_0 for the material.

Figure 2.8 shows the impulse predicted by the BBAY model (2.3) with our proposed $E_f(m)$ expansion using the coefficients given in Table 1. We also plot results using the McCloskey-Thompson model for $E_f(m)$, using the estimated vaporization energy $E_{vap} = 10E_{melt}$ as in Remo et al. [136]. We observe that our approach, by design, does well at predicting impulse from the simulations, which here have been calibrated to agree with experiment. Our approach agrees with the simulated impulse values to a much greater degree of accuracy than does the McCloskey-Thompson model, which we find over-predicts the impulse considerably in accordance with the findings in Remo et al. [136]. So, the BBAY model augmented with our data-driven model for the $E_f(m)$ function can be used for calculation of impulse from nominal x-ray spectra measurements with greater accuracy than the analytical modeling approaches used in previous studies.

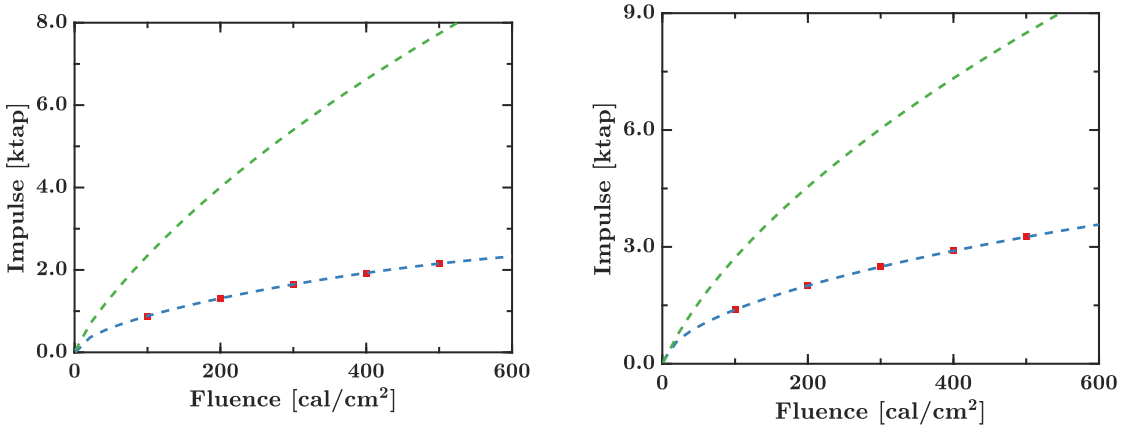

Figure 2.8: Impulse generated in (a) Ti-64 and (b) Al-6061 slabs from exposure to Xenon x-ray source, calculated via the BBAY model with E_f closure (blue dashed line), calculated as in Remo et al. [136] (green dashed line), and from simulations (red squares).

2.7 Results and model verification

In this section, we verify the results of the model by comparing to impulse-spectrum sensitivity values calculated from simulations by brute-force model reevaluation using finite differences [128]. In particular, we evaluate the impulse-spectrum sensitivity by perturbing the spectra, binned from the spectrum shown in Figure 2.2a and re-scaled to the fluence values used in the least-squares approach in Section 2.6. These spectra are used to compute the energy deposition profiles according to Equation (2.7) for use in the semi-analytical model, as well as to initialize Mercury code for the simulations used here. We perturb the spectra used for brute-force sensitivity evaluation using forward finite differences:

$$\frac{\delta I}{\delta F_g} \approx \frac{I(F_g + \Delta F) - I(F_g)}{\Delta F}. \tag{2.20}$$

We find that this procedure works best if the bins are not uniformly spaced in photon energy, but instead are selected to contain equal fluence. Here, ΔF is 16% of the total

fluence. Figure 2.9 shows the impulse-spectrum sensitivity calculated using Equation (2.9), using the fit for $E_f(m)$ in Equation (2.12) with the coefficients given in Table 1, for both Ti-64 and Al-6061 evaluated at the spectra used in Section 2.6. Also in this figure are the sensitivity results obtained from simulations using the approach outlined in Section 2.5.1 with 250 energy groups, which we find to agree well with the semi-analytical model. The edges in sensitivity occurring around 5 keV for Ti-64 and 1.5 keV for Al-6061 correspond to the K-edge transitions observed in the base elements in these alloys, Titanium and Aluminum [156].

The semi-analytical model presented here does well at calculating impulse-spectrum sensitivity without the need for running many simulations varying bin fluences; the sensitivity results evaluated from simulations shown in Figure 2.9 required 2,510 total simulations for each material, while only five simulations were used to fit the $E_f(m)$ function required for the model results. Experimental data could also be used for this procedure. Furthermore, the impulse-spectrum sensitivity contains valuable information about how changes in different portions of the x-ray spectrum change the impulse generated in the material. For example, the sensitivities shown in Figure 2.9 indicate the portions of the spectrum where a change in fluence would lead to the largest change in the impulse. This is useful for applications where one seeks to modify the spectrum seen by the material in order to minimize the imparted impulse, e.g., in design of filters or coatings for damage mitigation.

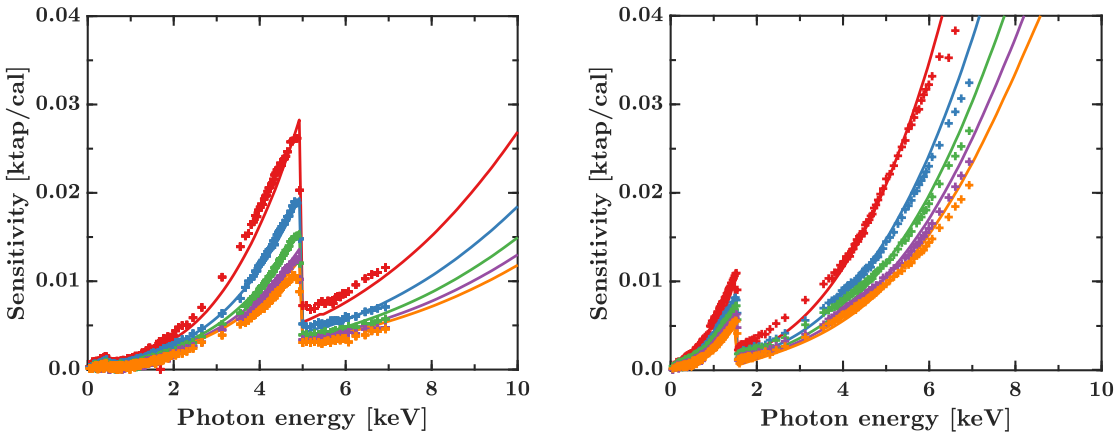

Figure 2.9: Sensitivity of impulse generated in (a) Ti-64 and (b) Al-6061 slabs to Xenon spectrum from semi-analytical impulse-spectrum sensitivity with E_f closure (solid lines) and measured directly from simulations (pluses). Impulse-spectrum sensitivity shown for baseline fluences of 100 cal/cm^2 (red), 200 cal/cm^2 (blue), 300 cal/cm^2 (green), 400 cal/cm^2 (purple), and 500 cal/cm^2 (orange). At points where the lines cannot be seen, they lie under their corresponding markers.

2.8 Application of impulse-spectrum sensitivity

In this section, we use the results of the semi-analytical model for impulse-spectrum sensitivity to constrain the uncertainties in the generated impulse based on uncertainties in the detailed x-ray source spectra. We consider an x-ray source spectrum where, via some statistical methodology, the true value of a group's fluence has been inferred to lie within an interval ΔF_g of some nominal value $\bar{F}_g$. We write the fluence for a group in such a spectrum as $F_g = \bar{F}_g \pm \Delta F_g$, where the quantity ΔF_g is the uncertainty of the fluence of group g. Given this spectrum, we seek to determine the nominal value and uncertainty of the impulse, i.e., $I = \bar{I} + \Delta I$. We calculate the nominal impulse value using the BBAY model (2.1). We use the semi-analytical impulse-spectrum sensitivity model in Equation (2.9) to evaluate the sensitivities $\delta I_g / \delta F_g$ at the nominal spectrum. Then, as a first-order approximation, we write the uncertainty in impulse as

$$\Delta I \approx \frac{\delta I}{\delta F_1}\Delta F_1 + \frac{\delta I}{\delta F_2}\Delta F_2 + ... + \frac{\delta I}{\delta F_G}\Delta F_G, \tag{2.21}$$

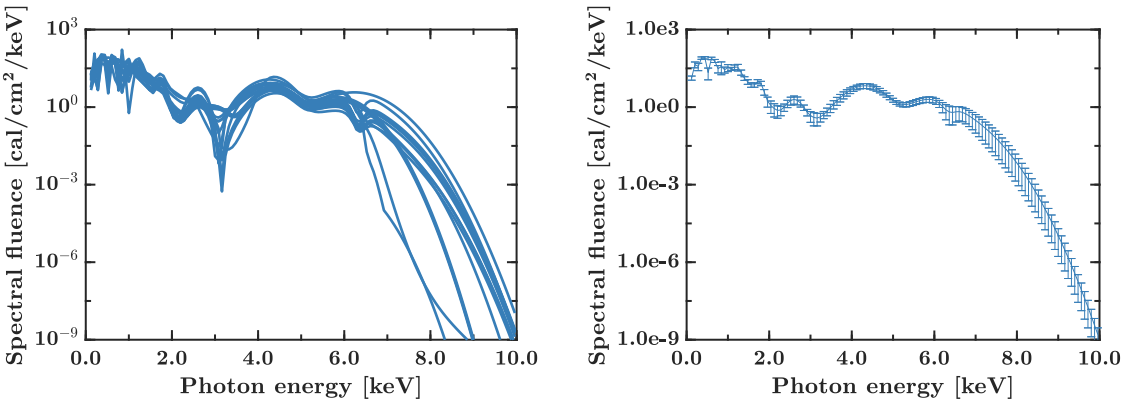

Figure 2.10: Time-integrated unfolded Dante spectra used to determine uncertainty of Xenon spectrum due to shot-to-shot variation. (a) Unfolded data, grouped into 250 groups, (b) nominal spectrum and error bars created from two-sided 90% confidence interval.

where the sensitivities are evaluated at the nominal spectrum.

To demonstrate this methodology, we compute statistical uncertainties of an ensemble of time-integrated Xenon spectra measured by Dante in 17 different experiments on the NIF [131]. As the source characteristics are nominally the same, and the same method was used to unfold the spectra from the unfolded Dante data, we attribute the variations in these x-ray spectra to shot-to-shot variation caused by random fluctuations in the system [125]. We group the raw Dante spectra into 250 photon energy groups. The 17 spectra used are shown in Figure 2.10a. Considerable variation can be observed between these spectra, which are collected from what are nominally the same experiments. We then compute the mean fluence value $\bar{F}_g$ for each bin among the $n_s = 17$ spectra as well as the variance S_g for each group. We establish the uncertainty values of the x-ray fluence of each group using a two-sided 95% confidence interval assuming a Student's t-distribution, which we choose due to the fairly small sample size. We estimate the uncertainty in the fluence group g as $\Delta F_g = t_{95\%} S_g / \sqrt{n_s}$ where the appropriate t-score for a two-sided 95% confidence interval with $n_s - 1 = 16$ degrees of freedom is $t_{95\%} = 2.12$. The mean spectrum, in

units of spectral fluence, with error bars corresponding to the uncertainty estimate is shown in Figure 2.10b. The error bars shown here appear fairly small relative the values of the spectrum, and in many practical cases where less data is available or one is considering different sources of uncertainty, the uncertainty may be much larger.

We then evaluate the nominal impulse using the mean spectrum in (2.3), and the uncertainty in impulse using (2.21), where the semi-analytical sensitivity model (2.9) is used to calculate the sensitivity values at the mean spectrum. This uncertainty quantification procedure results in an impulse estimate of $I = 0.5792 \pm 0.0910$ ktap for Ti-64, and $I = 0.8891 \pm 0.1281$ ktap for Al-6061. The range of these uncertainty estimates correspond to approximately 32% and 28% of the nominal impulse values, respectively, which is significant. We note that our intention in this section is not to perform a rigorous uncertainty quantification study, but to demonstrate the viability of our impulse-spectrum sensitivity model in this context. This exercise also demonstrates that even spectra constrained by relatively small error bars may result in considerable uncertainty in impulse, depending on how the uncertainty values and sensitivity values are distributed in the spectrum. For this reason, it is important to analyze the impulse-spectrum sensitivity when designing experiments where the radiation source is subject to uncertainties.

2.9 Conclusions

In this chapter, we presented a semi-analytical model for impulse-spectrum sensitivity, a quantity that is useful for constraining the uncertainty in impulse generated in materials by intense radiation sources where the source spectrum is subject to uncertainties, as is the case for many HED experiments. Due to the complexity of energy deposition in radiatively-driven blow-off and impulse generation in materials, there is a term in our impulse-spectrum sensitivity model that cannot be known *a priori*, describing the energy of the blown-off material $E_f(m)$. We use a data-driven

approach to model this term using high-fidelity simulations, in which we calibrated material parameters to match data from experiments of x-ray irradiated materials on the National Ignition Facility. Then, we verified our model for impulse-spectrum sensitivity, comparing to results obtained from brute-force reevaluation of sensitivity with finite differences via these same simulations. We found that the procedure for modeling $E_f(m)$ works well, and allows our model to be used for predictive calculation of both impulse and impulse-spectrum sensitivity for a very small computational cost compared to the brute-force approach. Experimental data could also be used to fit the functional form of $E_f(m)$ in our approach. We then demonstrated the viability of this model for uncertainty propagation, employing this sensitivity model to constrain uncertainty in material impulse due to estimates of uncertainty resulting from shot-to-shot variation in experimentally measured x-ray spectra. This demonstration illustrates how simple and straightforward it is to use the semi-analytical impulse-spectrum sensitivity model to constrain impulse relevant to an experiment. Additionally, this example showed that seemingly slight uncertainty in source spectra can cause relatively large uncertainties in impulse, and so it is important to study the impulse-spectrum sensitivity function when designing experiments in which spectral uncertainties exist and the impulse should be estimated/constrained. As the development of high-fluence x-ray sources continues and radiatively-generated impulse in materials is further explored, it is our hope that this model provides a useful tool for design of future experiments.

CHAPTER III

Numerical Methods for Multi-Material Radiation Hydrodynamics

3.1 Abstract

In multifluid simulations that model thermal transport, both pressure and temperature errors may arise independently at material interfaces without careful treatment. Particularly, in radiation hydrodynamics simulations, temperature errors caused by a physically inconsistent treatment may be amplified through the source term and result in large errors in every state variable within a few time steps. Additionally, the nonlinear diffusion operator may act to propagate these errors through the domain, and the non-conservative products representing work done by the radiation field provide a further mechanism to amplify these errors. These errors can pollute the solution, affecting the evolution of small-scale flow features, and depending on the optical properties of the fluid they can even cause unphysical values of density, pressure, and/or temperature. We present a discontinuous Galerkin method for multi-material flows in radiation hydrodynamics that prevents both pressure and temperature errors at interfaces via a conservative and high-order accurate limiting scheme. Our overall scheme is arbitrarily high-order accurate, respects conservation, and prevents pressure and temperature errors at material interfaces and material contacts. In ad-

dition, our method is compact, requiring communication only between neighboring cells. We apply a physics-based discontinuity sensor for the radiation hydrodynamics equations to limit only cells adjacent to discontinuities in the solution. We verify the properties of this method using simple one-dimensional multifluid test problems. We then apply the method to a two-dimensional problem relevant to high-energy density (HED) science.

3.2 Introduction

Many HED phenomena (e.g., inertial confinement fusion, stellar supernovae) involve flows of plasmas made up of different species in which a wide range of scales are present [157]. The study of these flows relies heavily on numerical simulation to represent radiation transport, ionization physics, and complex equation of state and opacity relationships in complex three-dimensional geometries [158, 159]. For example, comparison of quantities measured in inertial confinement fusion experiments to simulation results has made apparent that predictive simulation efforts must account fully for these multiphysics effects [28, 160, 161]. While the application of Reynolds-averaged Navier-Stokes (RANS) [162], large-eddy simulation (LES) [163, 164], and direct numerical simulation (DNS) [165] techniques to turbulent flows of traditional fluids has been richly documented, the study of turbulent flows in HED systems is dominated by the use of RANS models [166, 167]. It has been noted recently that explicit LES — involving the use of a subgrid-scale model — has not been applied to any HED problem [168], and a very limited number of studies examine aspects of HED flows with fully-resolved DNS [169]. RANS models are not suitable in a variety of HED problems depending on the geometry, the physics, and range of length scales [170, 171]. As a result, modeling parameters must be calibrated for a specific case, often using results from experiments [172] or simulations using a more sophisticated turbulence treatment [173]. In the case of HED systems, these experiments are ex-

pensive, and the diagnostics available often cannot probe all quantities necessary to constrain the calibration. Due to these limitations, we are interested in numerical methods appropriate for efficient direct numerical simulation of turbulent mixing in HED problems, with an emphasis on multiphysics systems that model flows coupled to radiative transport.

The discontinuous Galerkin (DG) method is an arbitrarily high-order accurate discontinuous finite-element method that uses polynomial basis functions to support the solution in each cell. As these basis functions are only supported on one cell in the computational domain, inter-cell fluxes are handled using approximate Riemann solvers as in the finite volume framework. For this reason, the discontinuous Galerkin method is well-suited for execution on large parallel architectures, as increasing the order of accuracy, even on unstructured meshes, does not increase the stencil size and introduce latency due to communication time. Additionally, the DG discretization for hyberbolic equations [174] is superconvergent in the cell-average error, converging at a rate of $2P + 1$, where P is the polynomial order of the basis [175]. Alternative schemes based on the use of the recovery operator are available for discretizing hyperbolic and parabolic equations that enable even higher convergence rates without extending the computational stencil [176]. The DG method can be naturally applied on unstructured meshes, which is particularly valuable in solving practical problems with complex geometries. Achieving high-order accuracy on unstructured meshes is expensive and complicated for finite-volume methods [177], and has not been achieved for finite difference methods. As with other high-order methods, the DG method requires a limiting procedure to capture discontinuities. One early limiting approach was the total-variation-bounded approach of Cockburn and Shu [178], which truncates the high-order basis representation at discontinuities. Others have suggested limiting approaches for the DG method that are high-order accurate [179, 180]. Particularly promising are limiting schemes based on hierarchical reconstruction (HR) [181, 182],

which is high-order accurate, conservative, and naturally adaptable to unstructured grids. Our interests lie in the discontinuous Galerkin scheme due to its efficiency in parallel execution at arbitrarily high orders of accuracy. The DG method has been applied to the single fluid radiation-hydrodynamics equations by previous authors [183, 184, 185]. Many previously proposed DG approaches for classical multi-material flows have either lacked high-order accuracy, not conserved energy, or suffered from a physically inconsistent treatment of interfaces [186, 187, 188]. As of this writing, the DG method has not been applied to multi-material radiation hydrodynamics flows in a manner that overcomes these difficulties.

Typically, Eulerian methods for solving multi-component flows fall under the categories of either interface capturing or interface tracking methods. Interface tracking schemes include level-set [189] and volume-of-fluid [190] approaches, which are used in some HED simulation codes [79, 158, 159, 191]. However, due to potential conservation errors and challenges with interface reconstruction, we do not pursue interface tracking approaches here. Interface capturing schemes are descendants of shock capturing schemes, representing interfaces as abrupt changes in material properties regularized on the grid across a few grid cells. Additional mass conservation equations must be solved with each additional component; however, it has been shown that only a particular form of these transport equations prevents spurious pressure errors from arising at interfaces when solving the compressible Euler equations [192, 193]. Furthermore, when thermal transport is included in the model (e.g., as in the compressible Navier Stokes equations), care must be taken to prevent spurious temperature errors as well [194]. As the material interface is a linearly degenerate field, unlike a shockwave, care must be taken to prevent the interface from over-diffusing, which can be addressed by use of high-order accurate solution-adaptive [194, 195, 196] or sharpening [197, 198] approaches that selectively apply or seek to reverse numerical diffusion, respectively.

In solving transport equations for the discontinuous material properties themselves, Abgrall [192] first showed that for ideal gases governed by the Euler equations, an equation for a specific function of the adiabatic index γ must be solved in advection form to avoid pressure oscillations and preserve mechanical equilibrium for isolated interfaces. This approach was extended to the stiffened gas equation of state by Shyue [193], who also introduced a scheme transporting the mass fraction (in advection form) of one of the fluids and calculating the material properties of the mixture fluid from this quantity. This concept has been extended to Weighted Essentially Non-Oscillatory methods [199, 200] and high-order finite differences [195, 201]. The approach of Henry de Frahan et al. [196] introduced a limiting procedure based on HR limiting that eliminates pressure oscillations using the γ-based method for the Euler equations. Johnsen and Ham [202] demonstrated that temperature errors arise from solving certain forms of transport equations as well, in the form of temperature spikes at material interfaces and contacts, and suggest remedies for the γ and mass fraction approaches. Models involving the transport of volume fraction, including the seven-equation [203] and five-equation [204, 205] models, show promise in solving various multifluid problems [206, 207, 208]. Furthermore, the five-equations approach has been extended to multifluid flows governed by the compressible Navier-Stokes equations via a method that prevents pressure and temperature errors simultaneously in a high-order finite volume scheme [194].

In many applications, it is important that errors in pressure and temperature are prevented, as they may propagate to other flow variables and pollute the solution. For example, in simulations of hydrodynamic instabilities, these errors can cause the growth due to physical instability of purely numerical, unphysical flow features. In turbulence simulations, they may affect important small-scale flow features, affecting the turbulent energy cascade. Furthermore, in situations where the transport coefficients depend on temperature, such as Sutherland's Law for temperature-dependent

viscosity [209], temperature errors may be further amplified by the transport mechanism, leading to severely incorrect temperature fields. This can be especially problematic in simulations that model phase change, reacting flow, or other thermal processes. The effect of pressure and temperature errors in multi-material radiation hydrodynamics has been considered [191], but has not been addressed in a manner that conserves material energy at the interface or avoids in interface reconstruction.

The objective of this work is to develop a robust, efficient, physically consistent, and accurate method for high-resolution simulations of HED systems. To this end, we propose a DG scheme to solve multi-material flows governed by the two-temperature radiation-hydrodynamics equations with a grey non-equilibrium radiation diffusion model [25, 63, 210]. Our approach can be extended to three-temperature models that account for the energies ion and electron fluids separately [79], as well as multigroup radiation transport [25, 63, 210]. To model material interfaces, we consider interface-capturing approaches based on the γ-based model of Abgrall [192], the volume fraction (five-equations model) [204, 205], and the mass fraction model [193]. This development results in a scheme that achieves high-order accuracy with a compact stencil even on unstructured meshes, conserves mass/momentum/energy, and prevents spurious pressure and temperature errors at material interfaces. Previous applications of the DG method to multi-material flows with thermal transport have not possessed these properties; the method we present is novelly well-suited for studies of hydrodynamic instabilities and turbulent mixing in HED systems, meeting all of the criteria for a method favorable for DNS. The remainder of this chapter is organized as follows. In Section 3.3, we present the physical model used here for multi-material radiation hydrodynamics. In Section 3.4, we describe the numerical models we employ for interface capturing. In Section 3.5, we present our DG discretization, as well at the HR limiting scheme. In Section 3.6, we analyze the cause of pressure and temperature errors at interfaces, and propose a strategy to prevent them. This strategy pertains

to the transport equations solved for each interface-capturing approach, as well as the manner in which the solution is limited using the HR limiting scheme. In Section 3.7, we provide results for one-dimensional test problems, verifying the properties of our approach. We also provide results for a two-dimensional problem to demonstrate the extension of the method to higher dimensions.

3.3 Physical model

3.3.1 Radiation-hydrodynamics model

We consider the grey non-equilibrium diffusion model of radiation hydrodynamics, derived in Appendix A and discussed in detail in Section 1.3:

$$\frac{\partial}{\partial t}\rho + \frac{\partial}{\partial x_j}(\rho u_j) = 0, \tag{3.1a}$$

$$\frac{\partial}{\partial t}\rho u_i + \frac{\partial}{\partial x_j}\left[\rho u_i u_j + (p + p_R)\delta_{ij}\right] = 0, \tag{3.1b}$$

$$\frac{\partial}{\partial t}E + \frac{\partial}{\partial x_j}\left[u_j(E + p)\right] + u_j\frac{\partial}{\partial x_j}p_R = -S_R, \tag{3.1c}$$

$$\frac{\partial}{\partial t}E_R + \frac{\partial}{\partial x_j}\left[u_j(E_R + p_R)\right] - u_j\frac{\partial}{\partial x_j}p_R - \frac{\partial}{\partial x_j}\left[D_R\frac{\partial}{\partial x_j}E_R\right] = S_R, \tag{3.1d}$$

where ρ is the fluid mass density, u_j is the velocity, p is the fluid pressure, p_R is the radiation pressure, E is the total fluid energy density, and E_R is the radiation energy density. The fluid total energy density is composed of internal and kinetic energies: $E = \rho e + \frac{1}{2}\rho u_j u_j$, where e is the fluid internal energy. This two-temperature model treats the fluid as one species, effectively assuming that energy coupling between electrons and ions is instantaneous. The approach we develop in this work can be extended to three-temperature models that solve separate energy equations for the ion and electron fluids. We discuss extension to the multigroup radiation diffusion model in Appendix C.

We use the flux-limited diffusion model of Morel [72]:

$$D_R = \frac{c}{\sqrt{(3\kappa_R)^2 + (\frac{1}{E_R}\frac{\partial E_R}{\partial x_j})^2}}, \tag{3.2}$$

where κ_R is the Rosseland mean opacity. Radiation diffusion models assume an optically thick fluid where the radiation field is isotropic (i.e., $p_R = \frac{1}{3}E_R$), which is a valid assumption in sufficiently dense systems. The form of flux-limited diffusion we use in (3.2) adjusts the diffusion coefficient such that the correct solution is attained in the both limits of optically thick and thin limits, as discussed in Section 1.3.2. However, problems featuring material interfaces between optically thick and thin systems may involve transition regions where the optical depth is on the order of unity. As the material interfaces in this work are represented as discontinuities in different quantities, regularized over a few grid cells, these transition regions are typically small using our approach. However, the problems considered in this work involve optically thick systems where $L\kappa_R$ is very small.

The non-equilibrium source term is given as:

$$S_R = c\kappa_P(B - E_R), \tag{3.3}$$

where B is the frequency-integrated Planck intensity evaluated at the material temperature T, $B = a_R T^4$. Under the conditions of interest, the Planck mean opacity κ_P drives the radiation field and the material to equilibrium in a local sense via photoabsorption and emission processes. In general, the Planck and Rosseland mean opacities are functions of density and temperature: $\kappa_R = \kappa_R(\rho, T)$, $\kappa_P = \kappa_P(\rho, T)$. To provide a more realistic treatment of radiation-material interaction, we calculate the opacities using the inverse Bremsstrahlung form [211],

$$\kappa = \kappa_0 T^{-7/2}\rho^2. \tag{3.4}$$

This model for the opacity dependence is used for the problems in this chapter unless otherwise stated. In this chapter, we limit ourselves to systems where grey treatment of radiation transport is sufficient. These are typically near-Planckian systems where free-free (i.e., inverse Bremsstrahlung) absorption dominates. Furthermore, the model in system (3.1) neglects viscosity, heat conduction, and mass diffusion.

An equation of state relating internal energy to pressure and temperature is required to close the system. For simplicity, we consider the ideal gas law,

$$p = \rho R T, \tag{3.5}$$

where the gas constant per unit mass, R, is given in terms of the gas constant per mole, R_u, by

$$R = \frac{R_u}{M}. \tag{3.6}$$

Here the molar mass of an ion species is $M = A m_p N_A/(\mathcal{Z}+1)$, where A is the atomic mass, m_p is the mass of a proton, N_A is Avogadro's number, and the average ionization is $\mathcal{Z}$. Defining the internal energy as

$$e = c_v T, \tag{3.7}$$

we can write the ideal gas law in terms of pressure or temperature,

$$\rho e = \frac{p}{\gamma - 1} = \rho c_v T, \tag{3.8}$$

where γ is the ratio of specific heats. We note that the approach used here can be extended to other equations of state.

3.3.2 Multifluid modeling

Our work is based on interface capturing, where the same equations are solved throughout the domain and abrupt changes in constitutive variables (eg. γ, c_v, κ_P, κ_R) represent material interfaces. The volume fraction $\alpha^{(l)}$ is the volume of fluid l divided by the total volume in a control volume, and the mass fraction $z^{(l)}$ is the mass of fluid l divided by the total mass in a control volume. By species conservation, $\sum_l \alpha^{(l)} = \sum_l z^{(l)} = 1$. The mixture density is written

$$\rho = \sum_l \rho^{(l)} \alpha^{(l)} = \sum_l \rho z^{(l)}. \tag{3.9}$$

The specific internal energy of the mixture e is

$$e = \sum_l z^{(l)} e^{(l)} \qquad \text{and} \qquad \rho e = \sum_l \rho^{(l)} \alpha^{(l)} e^{(l)}. \tag{3.10}$$

Therefore, the mass and volume fractions are related by

$$z^{(l)} = \rho^{(l)} \alpha^{(l)} / \rho. \tag{3.11}$$

The adiabatic index of the mixture is given in terms of mass fraction as,

$$\left(\frac{1}{\gamma - 1}\right)\frac{1}{M} = \sum_l z^{(l)} \left(\frac{1}{\gamma^{(l)} - 1}\right)\frac{1}{M^{(l)}}. \tag{3.12}$$

For the pressure-based and temperature-based ideal gas law, the mixture internal energy density in terms of volume and mass fractions is,

$$\rho e = \frac{p}{\gamma - 1} = \sum_l \alpha^{(l)} \frac{p^{(l)}}{\gamma^{(l)} - 1} = \frac{p}{\gamma - 1} = \sum_l z^{(l)} \frac{\rho p^{(l)}}{\rho^{(l)}(\gamma^{(l)} - 1)}, \tag{3.13a}$$

$$\rho e = \rho c_v T = \sum_l \alpha^{(l)} \rho^{(l)} c_v^{(l)} T^{(l)} = \sum_l \rho z^{(l)} c_v^{(l)} T^{(l)}. \tag{3.13b}$$

In the numerically diffused interface region, we assume isobaric ($p^{(l)} = p$) and isothermal ($T^{(l)} = T$) behavior,

$$\rho e = \frac{p}{\gamma - 1} = p \sum_l \alpha^{(l)} \frac{1}{\gamma^{(l)} - 1} = p \sum_l z^{(l)} \frac{\rho}{\rho^{(l)}(\gamma^{(l)} - 1)}, \tag{3.14a}$$

$$\rho e = \rho c_v T = T \sum_l \alpha^{(l)} \rho^{(l)} c_v^{(l)} = T \sum_l \rho z^{(l)} c_v^{(l)}. \tag{3.14b}$$

The isobaric and isothermal assumptions applies to the numerical mixture region, where the mixing occurs at a sub-grid level due to numerical dissipation. Finally, we consider the mixture opacity to be weighted by mass fraction,

$$\kappa_R = \sum_l z^{(l)} \kappa_R^{(l)}, \qquad \kappa_P = \sum_l z^{(l)} \kappa_P^{(l)}. \tag{3.15}$$

3.4 Numerical model

This methodology relies on numerical dissipation to stabilize interfaces, resulting in numerical mixture regions proportional to the mesh size in which the interface is smeared. We consider three distinct approaches multifluid flows:

- The γ approach [192, 193, 194]. It was shown that spurious pressure and temperature oscillations at interfaces can be prevented by solving the equations

$$\frac{\partial}{\partial t}\left(\frac{1}{\gamma - 1}\right) + u_j \frac{\partial}{\partial x_j}\left(\frac{1}{\gamma - 1}\right) = 0, \tag{3.16a}$$

$$\frac{\partial}{\partial t}(\rho c_v) + \frac{\partial}{\partial x_j}(\rho c_v u_j) = 0, \tag{3.16b}$$

  along with the compressible Navier-Stokes equations using an appropriate discretization. The quantities $1/(\gamma - 1)$ and ρc_v transported via (3.16a) and (3.16b) are used to compute pressure and temperature, respectively. As the γ-based ap-

proach involves solution of equations for the equation of state quantities γ and c_v themselves, no mixture rule is required, and the material properties entering the equation of state are used directly to calculate p and T from ρe. One can recover the volume or mass fractions using this approach, assuming that there are only two fluids present in the mixture regions with distinct γ and c_v values. For equations of state involving additional parameters, additional equations need to be solved.

- The volume fraction (five-equations model) approach [205, 212]. This approach requires transport of the volume fraction of fluid l, denoted $\alpha^{(l)}$,

$$\frac{\partial}{\partial t}\alpha^{(l)} + u_j \frac{\partial}{\partial x_j}\alpha^{(l)} = \Gamma_{ll'} \frac{\partial}{\partial x_j} u_j, \qquad \Gamma_{ll'} = \frac{\alpha^{(l)}\alpha^{(l')}\left[\rho^{(l')}(c_s^{(l')})^2 - \rho^{(l)}(c_s^{(l)})^2\right]}{\alpha^{(l)}\rho^{(l')}(c_s^{(l')})^2 + \alpha^{(l')}\rho^{(l)}(c_s^{(l)})^2} \tag{3.17a}$$

$$\frac{\partial}{\partial t}(\rho^{(l)}\alpha^{(l)}) + \frac{\partial}{\partial x_j}(\rho^{(l)}\alpha^{(l)}u_j) = 0, \tag{3.17b}$$

where $c_s^{(l)}$ is the hydrodynamic sound speed in fluid l [204]. Here, (3.17a) is used to calculate pressure and (3.17b) to calculate temperature according to mixing laws. The source term $\Gamma_{ll'}$ is required for thermodynamic consistency [213], and is zero in the limit of an infinitely-sharp interface. This approach is especially useful for flows requiring tabular data for material properties.

- The mass fraction approach [193, 202]. This approach requires transport of the mass fraction of fluid l, denoted $z^{(l)}$,

$$\frac{\partial}{\partial t} z^{(l)} + u_j \frac{\partial}{\partial x_j} z^{(l)} = 0, \tag{3.18a}$$

$$\frac{\partial}{\partial t}(\rho z^{(l)}) + \frac{\partial}{\partial x_j}(\rho z^{(l)} u_j) = 0. \tag{3.18b}$$

Equation (3.18a) is equivalent to (3.16a) if the molar masses of the two fluids

is the same, which is not true in general. Johnsen and Ham [202] noticed that errors occur if temperature is computed using (3.18a), and introduced (3.18b) to calculate temperature instead.

3.5 DG discretization

We use the discontinuous Galerkin method to discretize the system (3.1). Though we do not utilize the multigroup approach in this chapter, we discuss extending the numerical method in this section to the multigroup equations in Appendix C. Without loss of generality, we rewrite the one-dimensional form of the equations as an unsteady transport equation for a vector of state quantities $\mathbf{q}$ with divergence-form hyperbolic flux terms, non-conservative product terms, a diffusion term, and a source term:

$$\frac{\partial}{\partial t}\mathbf{q} + \mathbf{h}(\mathbf{q})\frac{\partial \mathbf{q}}{\partial x} + \frac{\partial}{\partial x}\mathbf{f}(\mathbf{q}) = \frac{\partial}{\partial x}\mathbf{g}(\mathbf{q}, \frac{\partial \mathbf{q}}{\partial x}) + \mathbf{s}(\mathbf{q}). \tag{3.19}$$

We discretize the solution domain Ω into E number of cells Ω_e where $\Omega = \cup_{e=1}^{e=E}\Omega_e$. We denote the locations of the edges of cell e as $x_{e\pm 1/2}$. In each cell e, the solution $\mathbf{q}$ is approximated by the finite-series expansion $\mathbf{q}^h$ in terms of basis functions ϕ_j^e as follows,

$$\mathbf{q}(x)|_{x\in\Omega_e} \approx \mathbf{q}^h(x)|_{x\in\Omega_e} = \mathbf{q}_e^h = \sum_{j=0}^{P} \widehat{\mathbf{q}}_e^j \phi_e^j(x). \tag{3.20}$$

Where $\widehat{\mathbf{q}}_e^j$ are the solution degrees of freedom and a Lagrange basis is used.

We use the DG method to discretize Equation (3.19). The weak form of Equation (3.19) is obtained by taking the inner product of the equation with test function

$\phi_e^k(x)$:

$$\int_{\Omega_e} \phi_e^k \frac{\partial \mathbf{q}_e^h}{\partial t} \mathrm{d}x + \left[\phi_e^k \mathbf{f}^* - \{\phi_e^k\}(\mathbf{hq})^* - \phi_e^k \mathbf{g}^*\right]_{x_{e-1/2}}^{x_{e+1/2}} - \int_{\Omega_e} \frac{\partial \phi_e^k}{\partial x} \left[\mathbf{f}(\mathbf{q}_e^h) - \mathbf{g}(\mathbf{q}_e^h, \boldsymbol{\sigma}_e)\right] \mathrm{d}x + \int_{\Omega_e} \phi_e^k \left[\mathbf{h}(\mathbf{q}_e^h) \frac{\partial \mathbf{q}_e^h}{\partial x} - \mathbf{s}(\mathbf{q}_e^h)\right] \mathrm{d}x = 0, \tag{3.21}$$

where $\{\xi\} = \frac{1}{2}(\xi_L + \xi_R)$, with L and R denoting the left and right cells at the cell edge. Equation (3.21) can be written in semi-discrete form:

$$M_e^{jk} \frac{\mathrm{d}\widehat{\mathbf{q}}_e^j}{\mathrm{d}t} + \mathbf{R}_{f,e}^k(\mathbf{q}^h) + \mathbf{R}_{h,e}^k(\mathbf{q}^h) + \mathbf{R}_{g,e}^k(\mathbf{q}^h) + \mathbf{R}_{s,e}^k(\mathbf{q}^h) = 0, \tag{3.22}$$

where the mass matrix for the cell e is

$$M_e^{jk} = \int_{\Omega_e} \phi_e^j \phi_e^k \mathrm{d}x, \tag{3.23}$$

and the $\mathbf{R}_e^k$ vectors contain the residual vector contributions from the divergence-form hyperbolic flux, non-conservative product, parabolic, and source terms, respectively. Multiplying Equation (3.22) by the inverse of the mass matrix, we have the semi-discrete form of the discontinuous Galerkin spatial discretization,

$$\frac{\mathrm{d}\widehat{\mathbf{q}}_e^j}{\mathrm{d}t} + \mathbf{D}_{f,e}^j(\mathbf{q}^h) + \mathbf{D}_{h,e}^j(\mathbf{q}^h) + \mathbf{D}_{g,e}^j(\mathbf{q}^h) + \mathbf{D}_{s,e}^j(\mathbf{q}^h) = 0, \tag{3.24}$$

where the D_j^e vectors are the DG spatial discretization operators for each term corresponding to the j-th unknown in cell e. We advance the semi-discrete system (3.24) in time using the standard explicit four-stage fourth-order accurate Runge-Kutta method [214]. We now describe how each term on the right-hand side of Equation (3.24) is calculated.

3.5.1 Advective terms

The residual vector for cell e used to discretize hyperbolic fluxes written in divergence form is:

$$\mathbf{R}^k_{f,e}(\mathbf{q}^h) = \left[\phi^k_e \mathbf{f}^*\right]_{x_{e-1/2}}^{x_{e+1/2}} - \int_{\Omega_e} \frac{\partial \phi^k_e}{\partial x} \mathbf{f}(\mathbf{q}^h) \mathrm{d}x \tag{3.25}$$

The numerical flux function $\mathbf{f}^*$ from the edge term approximately solves the Riemann problem at the cell edges, where the solution is double-valued, to provide a unique flux to be passed between these cells. Common choices of Riemann solvers include the Roe [215], HLL [216], and Rusanov [217] fluxes. For the results shown in this paper, we use the Rusanov flux:

$$\mathbf{f}^*|_{x_{e+1/2}} = \frac{\mathbf{f}(\mathbf{q}^h_R) + \mathbf{f}(\mathbf{q}^h_L)}{2} - \frac{s}{2}(\mathbf{q}^h_R - \mathbf{q}^h_L), \tag{3.26}$$

where s is the maximum wave-speed in the system. For the hyperbolic part of the system (3.1), the wave-speeds are $\lambda_1 = u - a$, $\lambda_2 = u$, $\lambda_3 = u$, $\lambda_4 = u + a$, where the radiation hydrodynamic sound speed is $a = \sqrt{c_s^2 + c_R^2}$. Here, the hydrodynamic sound speed is $c_s = \sqrt{\gamma p/\rho}$ and the radiation sound speed is $c_R = \sqrt{\frac{1}{3}(E_R + p_R)/\rho}$. The volume integral in Equation (3.25) is calculated by numerical quadrature.

System (3.1) contains work terms that appear in the radiation and material energy equations as non-conservative products. Additionally, as described in Section 3.6.1, transport equations for material properties and/or mixture fractions in advection form, involving non-conservative products, need to be solved to prevent pressure and temperature errors across material interfaces and contact waves. Del Maso et al. [218] established the definition of weak solutions for non-conservative products. This concept was later implemented for the discontinuous Galerkin method [219]. The

residual vector discretizing non-conservative products for cell e is

$$\mathbf{R}^k_{h,e}(\mathbf{q}^h) = -\left[\{\phi^k_e\}(\mathbf{hq})^*\right]_{x_{e-1/2}}^{x_{e+1/2}} + \int_{\Omega_e} \phi^k_e \mathbf{h}(\mathbf{q}) \frac{\partial \mathbf{q}^h}{\partial x} \mathrm{d}x. \tag{3.27}$$

The edge term in this equation is evaluated as

$$(\mathbf{hq})^*|_{x_{e+1/2}} = \int_0^1 \mathbf{h}(\boldsymbol{\varphi}(\tau; \mathbf{q}_L, \mathbf{q}_R)) \frac{\partial \boldsymbol{\varphi}}{\partial \tau}(\tau; \mathbf{q}_L, \mathbf{q}_R) \mathrm{d}\tau, \tag{3.28}$$

using a linear path between interface states, $\boldsymbol{\varphi}(\tau; \mathbf{q}_L, \mathbf{q}_R) = (\mathbf{q}_R - \mathbf{q}_L)\tau + \mathbf{q}_L$. We analytically evaluate the integral in Equation (3.28), and evaluate the volume integral term on the right-hand side of Equation (3.27) by numerical quadrature.

3.5.2 Diffusion terms

We use the BR-II scheme [220] for discretizing diffusion terms, written in the mixed form [221]. The residual vector containing diffusive contributions is given as

$$\mathbf{R}^k_{g,e}(\mathbf{q}^h) = -\left[\phi^k_e \mathbf{g}^*\right]_{x_{e-1/2}}^{x_{e+1/2}} + \int_{\Omega_e} \mathbf{g}(\mathbf{q}^h, \boldsymbol{\sigma}_e) \frac{\partial \phi^k_e}{\partial x} \mathrm{d}x. \tag{3.29}$$

Here the auxiliary variable $\boldsymbol{\sigma}_e(x)$ is an approximation of the gradient of $\mathbf{q}$ within Ω_e, supported by the same set of basis functions as in Equation (3.20),

$$\boldsymbol{\sigma}(x)|_{x\in\Omega_e} = \boldsymbol{\sigma}_e = \sum_{j=0}^{P} \widehat{\boldsymbol{\sigma}}^j_e \phi^j_e(x). \tag{3.30}$$

Here $\mathbf{q}^*$ and $\boldsymbol{\sigma}^*$ are the solution and gradient values at the cell edge, respectively, used to evaluate $\mathbf{g}^* = \mathbf{g}(\mathbf{q}^*, \boldsymbol{\sigma}^*)$. In each cell e we enforce the auxiliary variable to be

weakly equivalent to the gradient of the DG solution:

$$\int_{\Omega_e} \phi_e^k \boldsymbol{\sigma}_e \mathrm{d}x = \int_{\Omega_e} \phi_e^k \frac{\partial \mathbf{q}^h}{\partial x} \mathrm{d}x. \tag{3.31}$$

Applying integration by parts yields:

$$\int_{\Omega_e} \phi_e^k \boldsymbol{\sigma}_e \mathrm{d}x = \left[\phi_e^k \mathbf{q}^*\right]_{x_{e-1/2}}^{x_{e+1/2}} - \int_{\Omega_e} \frac{\partial \phi_e^k}{\partial x} \mathbf{q}^h \mathrm{d}x. \tag{3.32}$$

To define the common edge solution value, the BR-II method uses the arithmetic average of adjacent solution values at the edge: $\mathbf{q}^* = \{\mathbf{q}^h\}$. Consider the edge between the cells Ω_e and Ω_{e+1}, located at $x_{e+1/2}$. For the common solution gradient at the edge, the left and right-hand localized gradients are formed in a manner that combines the solution in Ω_e and Ω_{e+1}. These gradients are here given as:

$$\mathbf{g}_{R,e} = \sum_{j=0}^{P} \widehat{\mathbf{g}}_{R,e}^j \phi_e^j, \quad \mathbf{g}_{L,e+1} = \sum_{j=0}^{P} \widehat{\mathbf{g}}_{L,e+1}^j \phi_{e+1}^j, \tag{3.33}$$

$$\int_{\Omega_e} \phi_e^k \mathbf{g}_{R,e} \mathrm{d}x = \chi \left[\phi_e^k (\mathbf{q}^* - \mathbf{q}_e^h)\right]_{x_{e-1/2}}^{x_{e+1/2}} - \int_{\Omega_e} \phi_e^k \frac{\partial \mathbf{q}_e^h}{\partial x} \mathrm{d}x, \tag{3.34}$$

$$\int_{\Omega_{e+1}} \phi_e^k \mathbf{g}_{L,e+1} \mathrm{d}x = \chi \left[\phi_e^k (\mathbf{q}^* - \mathbf{q}_{e+1}^h)\right]_{x_{e+1/2}}^{x_{e+3/2}} - \int_{\Omega_{e+1}} \phi_e^k \frac{\partial \mathbf{q}_{e+1}^h}{\partial x} \mathrm{d}x. \tag{3.35}$$

Here χ is a stabilization parameter, taken as $\chi = 2$ in 1-D [220]. The interfacial gradient $\boldsymbol{\sigma}^*$ at $x_{e+1/2}$ is calculated as $\boldsymbol{\sigma}^*|_{x_{e+1/2}} = \frac{1}{2}(\mathbf{g}_{R,e} + \mathbf{g}_{L,e+1})|_{x_{e+1/2}}$. We note that the method for multi-material radiation hydrodynamics outlined in this chapter can be readily coupled with other diffusion discretizations for DG, such as the local discontinuous Galerkin scheme [222] or the compact gradient recovery scheme [223].

3.5.3 Source terms

The residual vector containing source contributions for cell e is,

$$\mathbf{R}^k_{s,e}(\mathbf{q}^h) = -\int_{\Omega_e} \phi^k_e \mathbf{s}(\mathbf{q}^h) \mathrm{d}x. \tag{3.36}$$

Like all other cell-interior integrals, we evaluate this term directly using numerical quadrature.

3.5.4 Hierarchical reconstruction limiting

For problems featuring discontinuous solutions, limiting procedures are required to damp the oscillations caused by high-order methods. We follow a two-step approach: we first identify discontinuities and, in these flagged cells, we apply the hierarchical reconstruction (HR) limiting procedure [181, 182] to limit the solution, which preserves high-order accuracy. The procedure involves recomputing solution degrees of freedom, from those associated with the highest-order to the lowest-order basis contribution, using a MUSCL [224] or WENO [225] approach. To perform this procedure, we re-cast our DG approximation in Equation (3.20) in terms of Taylor polynomials:

$$\mathbf{q}^h_e(x) = \sum_{j=0}^{P} \widehat{\mathbf{q}}^{T,j}_e \frac{x^j}{j!}. \tag{3.37}$$

In practice, the transformation between the basis representation degrees of freedom $\widehat{\mathbf{q}}^j_e$ and the Taylor degrees of freedom $\widehat{\mathbf{q}}^{T,j}_e$ is performed with a matrix multiplication that can be pre-computed. To calculate the j-th limited coefficient, which we denote here as $\widetilde{\widehat{\mathbf{q}}^{T,j}_e}$, we calculate the $(j-1)$-th derivative of $\mathbf{q}^h_e(x)$ and write it in terms of a linear polynomial $L_e(x)$ and a higher-order polynomial $R_e(x)$: $\partial^{j-1}/\partial x^{j-1}\mathbf{q}^h_e(x) =$

$L_e(x) + R_e(x)$. We approximate the cell averages in cell e and its neighbors as:

$$\overline{L}_{e-1} = \overline{\frac{\partial^{j-1}\mathbf{q}^h_{e-1}}{\partial x^{j-1}}} - \overline{\overline{R}}_e, \quad \overline{L}_e = \overline{\frac{\partial^{j-1}\mathbf{q}^h_{e}}{\partial x^{j-1}}} - \overline{\overline{R}}_e, \quad \overline{L}_{e+1} = \overline{\frac{\partial^{j-1}\mathbf{q}^h_{e+1}}{\partial x^{j-1}}} - \overline{\overline{R}}_e, \tag{3.38}$$

where $\overline{\overline{R}}_e$ is the cell average of cell e's higher-order polynomial with limited higher-order degrees of freedom, which we treat as if it extends into the neighboring cell. We combine these cell averages using the MUSCL approach to reconstruct the new linear polynomial L_e, and in turn, the limited coefficient $\widetilde{\widehat{\mathbf{q}}^{T,j}_e}$. The inverse matrix multiplication is then used to recompute $\widetilde{\widehat{\mathbf{q}}^{j}_e}$. This procedure preserves cell averages, so results in an overall conservative method when coupled with a conservative DG discretization, like the one we employ in Equation (3.25). We apply the limiting procedure to flagged cells at each Runge-Kutta sub-step.

3.6 Preventing pressure and temperature errors

As we have discussed, in applications where small-scale flow features are important, such as the study of hydrodynamic instabilities and turbulence, it is important to prevent pressure and temperature errors that pollute the solution. In particular, as the source term in Equations (3.1c) and (3.1d) explicitly depends on temperature and the the source and diffusion terms depend implicitly on temperature through the opacities via Equation (3.4), preventing temperature errors is crucial in radiation hydrodynamics. In this work, we distinguish between the three following types of discontinuities:

- single-fluid contact discontinuity: (uniform u, $p + p_R$, γ, c_v, discontinuous ρ, T)
- material contact discontinuity: (uniform u, $p + p_R$, discontinuous ρ, T, γ, c_v)
- material interface: (uniform u, p, p_R, T, discontinuous ρ, γ, c_v)

Using the DG approach with HR limiting described in Section 3.5, the case of the single-fluid contact does not require special treatment. However, it has been shown that careful treatment is required for material contacts and material interfaces due to pressure and temperature errors generated by physically inconsistent discretization. Specifically, these errors have been observed in the form of pressure oscillations and temperature spikes that form at both material interfaces and contacts [202]. Pressure oscillations cause issues even for the Euler equations, where the the pressure affects the momentum through the flux in the momentum equation, and then the density through the continuity equation. However, temperature is not a quantity that appears explicitly in the Euler equations, so temperature spikes do not affect other variables. In systems that model thermal transport, such as the compressible Navier-Stokes equations, special treatment is required to prevent temperature spikes, which will propagate errors to other flow variables [194]. In our case, the radiation-hydrodynamics equations have terms representing material/radiation interaction that may amplify errors in the temperature fields, making a physically consistent treatment especially important.

When designing a DG method for multi-material flows in radiation hydrodynamics, there are two potential sources of pressure and temperature errors: (i) the form of the extra mass conservation equation(s), and (ii) the limiting scheme applied at elements containing material interfaces. In this section, we analyze the origins of pressure and temperature errors in multi-material radiation hydrodynamics simulations using our approach. First, we adapt the analysis of Abgrall [192] to identify the form of the transport equations that must be solved for the γ-based, volume fraction, and mass fraction approaches to prevent pressure and temperature errors for material interfaces in multi-material radiation hydrodynamics flows. Next, we extend the approach of Henry de Frahan et al. [196] to analyze the cause of pressure and temperature errors due to the limiting scheme for the γ-based, volume fraction, and

mass fraction approaches. We then design an approach based on HR limiting to prevent pressure and temperature errors based on the approach in this same reference. We address the case of the material contact in Section 3.7, where we solve a test problem to show that our scheme avoids pressure oscillations and temperature spikes for material contacts as well.

3.6.1 Preventing errors caused by form of transport equations

We consider the 1-D advection at constant velocity of a material interface in thermomechanical equilibrium, situated at initial time between neighboring cells Ω_{e-1} and Ω_e. Initially, p, u, T, and E_R are uniform while ρ and the material properties vary in general across the interface: $u_{e-1} = u_e = u > 0$, $p_{e-1} = p_e = p$, and $T_{e-1} = T_e = T$, while $\rho_{e-1} \neq \rho_e$, $\gamma_{e-1} \neq \gamma_e$ and $(c_v)_{e-1} \neq (c_v)_e$. We assume the radiation field is initially in equilibrium with the material, where $E_R = a_R T^4$. In this case, the the source, parabolic, and non-conservative product terms in Equations (3.1c) and (3.1d) are identically zero initially. The exact solution after a single time-step gives the velocity, pressure, and temperature as unchanged, while the interface has advected some distance $u\Delta t$, where Δt is the size of the time-step. This analysis makes use of the properties derived in Appendix C.

The semi-discrete form of the continuity equation (3.1a) reduces to

$$\frac{\mathrm{d}\widehat{\rho}_e^j}{\mathrm{d}t} + D_{f,e}^j(\rho u) = 0. \tag{3.39}$$

Since the velocity is uniform, we apply property (D.1),

$$\frac{\mathrm{d}\widehat{\rho}_e^j}{\mathrm{d}t} + u D_{f,e}^j(\rho) = 0. \tag{3.40}$$

For the momentum equation (3.1b),

$$\frac{\mathrm{d}(\widehat{\rho u})_e^j}{\mathrm{d}t} + D_{f,e}^j(\rho u^2 + p + p_R) = 0. \tag{3.41}$$

Applying properties (D.1) and (D.2), this equation becomes,

$$\frac{\mathrm{d}(\widehat{\rho u})_e^j}{\mathrm{d}t} = -u^2 D_{f,e}^j(\rho). \tag{3.42}$$

We thus obtain,

$$\frac{\mathrm{d}(\widehat{\rho u})_e^j}{\mathrm{d}t} = u\frac{\mathrm{d}\widehat{\rho}_e^j}{\mathrm{d}t}. \tag{3.43}$$

Therefore, the condition that velocity remain constant at the following time step is obeyed.

The material energy equation, (3.1c), becomes, in the case of thermomechanical equilibrium,

$$\frac{\mathrm{d}\widehat{E}_e^j}{\mathrm{d}t} + D_{f,e}^j(u(E+p)) = 0, \tag{3.44}$$

where we make use of the properties (D.3) and (D.5). Writing the total energy as $\widehat{E}_e^j = (\widehat{\rho e})_e^j + \frac{1}{2}u^2\widehat{\rho}_e^j$, we use the momentum and continuity equations to reduce Equation (3.44) to:

$$\frac{\mathrm{d}(\widehat{\rho e})_e^j}{\mathrm{d}t} + uD_{f,e}^j(\rho e) = 0. \tag{3.45}$$

3.6.1.1 γ-based approach

Inserting the pressure-based equation of state, $\big(\widehat{\rho e}\big)_e^j = p\big(\widehat{\frac{1}{\gamma-1}}\big)_e^j$, into Equation (3.45) yields,

$$\frac{\mathrm{d}}{\mathrm{d}t}\left[p\left(\widehat{\frac{1}{\gamma-1}}\right)_e^j\right] + upD_{f,e}^j\left(\frac{1}{\gamma-1}\right) = 0. \tag{3.46}$$

Expanding the temporal derivative,

$$\left[\frac{\mathrm{d}p}{\mathrm{d}t}\left(\widehat{\frac{1}{\gamma-1}}\right)_e^j\right] + p\left\{\frac{\mathrm{d}}{\mathrm{d}t}\left(\widehat{\frac{1}{\gamma-1}}\right)_e^j + uD_{f,e}^j\left(\frac{1}{\gamma-1}\right)\right\} = 0. \tag{3.47}$$

We observe that the term in braces is the semi-discrete form of the equation

$$\frac{\partial}{\partial t}\left(\frac{1}{\gamma-1}\right) + u\frac{\partial}{\partial x}\left(\frac{1}{\gamma-1}\right) = 0. \tag{3.48}$$

This equation states that the function $\frac{1}{\gamma-1}$ is advected by the flow. If we ensure that this result is enforced, Equation (3.47) implies that $\frac{\mathrm{d}p}{\mathrm{d}t} = 0$ and the pressure remains constant at the following time step. We use this equation to transport $\frac{1}{\gamma-1}$ and to calculate pressure for the γ-based approach.

Inserting the temperature-based equation of state, $\left(\widehat{\rho e}\right)_e^j = T\left(\widehat{\rho c_v}\right)_e^j$, into Equation (3.45) yields,

$$\frac{\mathrm{d}}{\mathrm{d}t}\left[T\left(\widehat{\rho c_v}\right)_e^j\right] + TD_{f,e}^j\left(\rho c_v u\right) = 0. \tag{3.49}$$

Expanding the temporal derivative,

$$\left[\frac{\mathrm{d}T}{\mathrm{d}t}\left(\widehat{\rho c_v}\right)_e^j\right] + T\left\{\frac{\mathrm{d}}{\mathrm{d}t}\left(\widehat{\rho c_v}\right)_e^j + D_{f,e}^j\left(\rho c_v u\right)\right\} = 0. \tag{3.50}$$

We observe that the term in braces is the semi-discrete form of the equation

$$\frac{\partial}{\partial t}\left(\rho c_v\right) + \frac{\partial}{\partial x}\left(\rho c_v u\right) = 0. \tag{3.51}$$

This equation states that the function ρc_v is conserved. If we ensure that this result is enforced, Equation (3.50) implies that $\frac{\mathrm{d}T}{\mathrm{d}t} = 0$ and the temperature remains constant at the following time step. We use this equation to transport c_v and to calculate temperature for the γ-based model.

3.6.1.2 Volume fraction approach

Inserting the pressure-based equation of state, $\left(\widehat{\rho e}\right)_e^j = p\sum_l \left(\widehat{\frac{\alpha^{(l)}}{\gamma^{(l)}-1}}\right)_e^j$, into Equation (3.45) yields,

$$\frac{\mathrm{d}}{\mathrm{d}t}\left[p\sum_l\left(\widehat{\frac{\alpha^{(l)}}{\gamma^{(l)}-1}}\right)_e^j\right] + upD_{f,e}^j\left(\sum_l \frac{\alpha^{(l)}}{\gamma^{(l)}-1}\right) = 0. \tag{3.52}$$

Expanding the temporal derivative,

$$\left[\frac{\mathrm{d}p}{\mathrm{d}t}\sum_l\left(\widehat{\frac{\alpha^{(l)}}{\gamma^{(l)}-1}}\right)_e^j\right] + p\sum_l\left\{\frac{\mathrm{d}}{\mathrm{d}t}\left(\widehat{\frac{\alpha^{(l)}}{\gamma^{(l)}-1}}\right)_j^e + uD_{f,e}^j\left(\frac{\alpha^{(l)}}{\gamma^{(l)}-1}\right)\right\} = 0. \tag{3.53}$$

Noting that the fluid equation of state property $\gamma^{(l)}$ is a constant, the term in braces is the semi-discrete form of the equation,

$$\frac{\partial}{\partial t}\alpha^{(l)} + u\frac{\partial}{\partial x}\alpha^{(l)} = 0, \tag{3.54}$$

for each fluid species. This equation states that $\alpha^{(l)}$ is advected by the flow. If we ensure that this result is enforced, Equation (3.53) implies that $\frac{\mathrm{d}p}{\mathrm{d}t} = 0$ and the pressure remains constant at the following time step. We use this equation to transport $\alpha^{(l)}$ and to calculate pressure in the volume fraction approach. This equation does not include the source term in Equation (3.17a), required for thermodynamic consistency, because the dilatation of the flow in this analysis is zero.

Inserting the temperature-based equation of state, $\left(\widehat{\rho e}\right)_e^j = T\sum_l \left(\widehat{\rho^{(l)}\alpha^{(l)}c_v^{(l)}}\right)_e^j$, into Equation (3.45) yields,

$$\frac{\mathrm{d}}{\mathrm{d}t}\left[T\sum_l\left(\widehat{\rho^{(l)}\alpha^{(l)}c_v^{(l)}}\right)_e^j\right] + TD_{f,e}^j\Big(\sum_l \rho^{(l)}\alpha^{(l)}c_v^{(l)}u\Big) = 0. \tag{3.55}$$

Expanding the temporal derivative,

$$\left[\frac{\mathrm{d}T}{\mathrm{d}t}\sum_l \left(\widehat{\rho^{(l)}\alpha^{(l)}c_v^{(l)}}\right)_e^j\right] + T\sum_l \left\{\frac{\mathrm{d}}{\mathrm{d}t}\left(\widehat{\rho^{(l)}\alpha^{(l)}c_v^{(l)}}\right)_e^j + D_{f,e}^j\left(\rho^{(l)}\alpha^{(l)}c_v^{(l)}u\right)\right\} = 0. \quad (3.56)$$

Noting that the fluid equation of state property $c_v^{(l)}$ a constant, we observe that the term in braces is the semi-discrete form of the equation,

$$\frac{\partial}{\partial t}(\rho^{(l)}\alpha^{(l)}) + \frac{\partial}{\partial x}(\rho^{(l)}\alpha^{(l)}u) = 0, \quad (3.57)$$

for each fluid species. This equation states that $\rho^{(l)}\alpha^{(l)}$, the mass of fluid l, is conserved. If we ensure that this result is enforced, Equation (3.56) implies that $\frac{\mathrm{d}T}{\mathrm{d}t} = 0$ and the temperature remains constant at the following time step. We use this equation to transport $\rho^{(l)}\alpha^{(l)}$ and to calculate temperature in the volume fraction approach.

3.6.1.3 Mass fraction approach

Inserting the pressure-based equation of state, $\left(\widehat{\rho e}\right)_e^j = p\sum_l \left(\widehat{\frac{\rho z^{(l)}}{\rho^{(l)}(\gamma^{(l)}-1)}}\right)_e^j$, Equation (3.45) becomes

$$\frac{\mathrm{d}}{\mathrm{d}t}\left[p\sum_l \left(\frac{\widehat{\rho z^{(l)}}}{\rho^{(l)}(\gamma^{(l)}-1)}\right)_e^j\right] + upD_{f,e}^j\left(\sum_l \frac{\rho z^{(l)}}{\rho^{(l)}(\gamma^{(l)}-1)}\right) = 0. \quad (3.58)$$

Expanding the temporal derivative,

$$\left[\frac{\mathrm{d}p}{\mathrm{d}t}\sum_l \left(\frac{\widehat{\rho z^{(l)}}}{\rho^{(l)}(\gamma^{(l)}-1)}\right)_e^j\right] + p\sum_l \left\{\frac{\mathrm{d}}{\mathrm{d}t}\left(\frac{\widehat{\rho z^{(l)}}}{\rho^{(l)}(\gamma^{(l)}-1)}\right)_e^j + uD_{f,e}^j\left(\frac{\rho z^{(l)}}{\rho^{(l)}(\gamma^{(l)}-1)}\right)\right\} = 0. \quad (3.59)$$

Noting that the fluid equation of state property $\gamma^{(l)}$ is a constant, we observe that the term in braces is the semi-discrete form of the equation

$$\frac{\partial}{\partial t}\left(\frac{\rho z^{(l)}}{\rho^{(l)}}\right) + u\frac{\partial}{\partial x}\left(\frac{\rho z^{(l)}}{\rho^{(l)}}\right) = 0, \quad (3.60)$$

for each fluid species. This equation states that $\rho z^{(l)}/\rho^{(l)}$ is advected by the flow. If we ensure that this is enforced, Equation (3.59) implies that $\frac{\mathrm{d}p}{\mathrm{d}t} = 0$ and the pressure remains constant at the following time step. We use this equation to transport $\rho z^{(l)}/\rho^{(l)}$ and to calculate pressure in the mass fraction approach.

Inserting the temperature-based equation of state, $\big(\widehat{\rho e}\big)_e^j = T\sum_l \big(\widehat{\rho z^{(l)} c_v^{(l)}}\big)_e^j$, Equation (3.45) becomes:

$$\frac{\mathrm{d}}{\mathrm{d}t}\left[T\sum_l \big(\widehat{\rho z^{(l)} c_v^{(l)}}\big)_e^j\right] + TD_{f,e}^j\Big(\sum_l (\rho z^{(l)} c_v^{(l)} u\Big) = 0. \tag{3.61}$$

Expanding the temporal derivative,

$$\left[\frac{\mathrm{d}T}{\mathrm{d}t}\sum_l \big(\widehat{\rho z^{(l)} c_v^{(l)}}\big)_e^j\right] + T\sum_l \left\{\frac{\mathrm{d}}{\mathrm{d}t}\big(\widehat{\rho z^{(l)} c_v^{(l)}}\big)_e^j + D_{f,e}^j\big(\rho z^{(l)} c_v^{(l)} u\big)\right\} = 0. \tag{3.62}$$

Noting that the fluid equation of state property $c_v^{(l)}$ is a constant, we observe that the term in braces is the semi-discrete form of the equation,

$$\frac{\partial}{\partial t}\big(\rho z^{(l)}\big) + \frac{\partial}{\partial x}\big(\rho z^{(l)} u\big) = 0. \tag{3.63}$$

for each fluid species. This equation states that $\rho z^{(l)}$, the mass of fluid l, is conserved. If we ensure that this is enforced, (3.62) implies that $\frac{\mathrm{d}T}{\mathrm{d}t} = 0$ and the pressure remains constant at the following time step. We use this equation to transport $\rho z^{(l)}$ and to calculate pressure in the mass fraction approach. We observe that, via Equation (3.11), the mass fraction and volume fraction approaches developed here are equivalent.

3.6.2 Preventing errors caused by limiting procedure

Solving the model equations as described in the previous section is not a sufficient condition to preserve thermomechanical equilibrium at material interfaces; a limiting scheme must be devised that does not introduce pressure and temperature errors. In

this section, we demonstrate that applying the HR limiting scheme directly to the total material energy introduces pressure and temperature oscillations at interfaces, and we derive a scheme to overcome these drawbacks. We require a limiting scheme that is (i) conservative, (ii) non-oscillatory, and (iii) high-order accurate. To describe the issue and the remedy we take here, we follow the development in Henry de Frahan et al. [196] and consider the variables Q, X, Y, and Z expressed as Taylor polynomials as in Equation (3.37) as functions of x. In this section, it should be assumed that all variable degrees of freedom correspond to the Taylor polynomial form rather than the DG basis form, and the superscript T is dropped. The variables are assumed to be related by some algebraic function f: $Q = f(X, Y, Z)$.

By construction, HR limiting satisfies condition (iii). For requirement (i), the limiting procedure must not change the cell-average value of the solution in each cell, so $\int_{\Omega_e} Q \mathrm{d}x = \int_{\Omega_e} \widetilde{Q} \mathrm{d}x$. For requirement (ii), if $Z(x)$ is equal to a constant $Z(x) = a$, that constant must be recovered after limiting through the function f, i.e., $\widetilde{Z} = f^{-1}(\widetilde{X}, \widetilde{Y}, \widetilde{Q}) = a$. However, we must design our limiting procedure around two nonlinear properties of the HR limiting procedure, which we verify in Appendix D: (i) limiting is not necessarily distributive, i.e., limiting a sum of functions is not equivalent to the sum of functions individually limited, and (ii) limiting a product of functions is not necessarily conservative. In other words, we have: $\widetilde{X + Y} \neq \widetilde{X} + \widetilde{Y}$, and $\int_{\Omega_e} \widetilde{X}\widetilde{Y} \mathrm{d}x \neq \int_{\Omega_e} XY \mathrm{d}x$. We propose to overcome these difficulties as follows:

(i) *Distributive property.* If $Q(x) = f(X, Y, a) = aX + Y$, and we limit to obtain $\widetilde{Q} = \widetilde{aX + Y}$ as well as $\widetilde{X}$, $\widetilde{Y}$, in general we cannot recover the value of a by calculating

$$\widetilde{a} = f^{-1}(\widetilde{X}, \widetilde{Y}, \widetilde{Q}) = \frac{1}{\widetilde{X}}(\widetilde{Q} - \widetilde{Y}) = \frac{1}{\widetilde{X}}(\widetilde{aX + Y} - \widetilde{Y}) \neq a. \tag{3.64}$$

This result is due to the nonlinear property of limiting sums. However, if we are to calculate the value of $\widetilde{Q}$ directly from the limited values of $\widetilde{aX}$, $\widetilde{Y}$ in the first place,

we can naturally recover a,

$$\widetilde{a} = f^{-1}(\widetilde{X}, \widetilde{Y}, \widetilde{Q}) = \frac{1}{\widetilde{X}}(\widetilde{Q} - \widetilde{Y}) = \frac{1}{\widetilde{X}}(\widetilde{aX} + \widetilde{Y} - \widetilde{Y}) = a. \tag{3.65}$$

This methodology ensures that the constant a is recovered, and that the procedure is non-oscillatory.

(ii) *Conservation of a product.* In general, if $Q = f(X, Y, Z) = XY$, and $\widetilde{Q} = \widetilde{X}\widetilde{Y}$, then $\int_{\Omega_e} Q \mathrm{d}x \neq \int_{\Omega_e} \widetilde{Q} \mathrm{d}x$. Using the chain rule, we express the degrees of freedom of $Q = XY$,

$$\widehat{Q}^0 = \widehat{X}^0 \widehat{Y}^0, \tag{3.66a}$$

$$\widehat{Q}^1 = \widehat{X}^1 \widehat{Y}^0 + \widehat{X}^0 \widehat{Y}^1, \tag{3.66b}$$

$$\widehat{Q}^2 = \widehat{X}^2 \widehat{Y}^0 + 2\widehat{X}^1 \widehat{Y}^1 + \widehat{X}^0 \widehat{Y}^2, \tag{3.66c}$$

$$... \tag{3.66d}$$

$$\widehat{Q}^n = \sum_{k=0}^{n} \binom{n}{k} \widehat{X}^{(n-k)} \widehat{Y}^k, \tag{3.66e}$$

where $\binom{n}{k}$ is the binomial coefficient. We then reconstruct the limited degrees of freedom of Q using those of X and Y,

$$\widetilde{\widehat{Q}^n} = \sum_{k=0}^{n} \binom{n}{k} \widetilde{\widehat{X}^{(n-k)}} \widetilde{\widehat{Y}^k}. \tag{3.67}$$

We impose conservation, requiring $\int_{\Omega_e} \widetilde{Q} \mathrm{d}x = \int_{\Omega_e} Q \mathrm{d}x$. Enforcing this requirement results in the constraints,

$$\sum_{k=0,2,4,...} \frac{2}{(k+1)!} (\widetilde{\widehat{Q}^k} - \widehat{Q}^k) = 0. \tag{3.68}$$

This requirement gives $P + 2$ constraints for only $P + 1$ degrees of freedom. We

combine the constraints for $k = 2, 4, ...$ degrees of freedom into that for $k = 0$, and reconstruct the limited degrees of freedom of Q from those of X and Z as,

$$\widetilde{\widehat{Q}^n} = \sum_{k=1}^{n} \binom{n}{k} \widetilde{\widehat{X}^{(n-k)}} \widetilde{\widehat{Y}^k}, \quad \text{for} \quad n = 1, ..., P, \tag{3.69a}$$

$$\widetilde{\widehat{Q}^0} = \widehat{Q}^0 - \sum_{k=2,4,...} \frac{1}{(k+1)!} (\widetilde{\widehat{Q}^k} - \widehat{Q}^k). \tag{3.69b}$$

Using this approach, if $Z = a$, then $Z_0 = a$ and $Z_k = 0$ for $k > 0$, therefore $\widetilde{Q} = a\widetilde{X}$, guaranteeing this procedure is non-oscillatory. The procedure also enforces conservation, so that the cell-average value of Q is not changed by the limiting procedure. This procedure also preserves high-order accuracy by construction.

We consider three adjacent 1-D cells numbered $e-1$, e, $e+1$, where a material interface in thermomechanical equilibrium advecting at a constant speed u is present in cell e. Initially, p, u, T, and E_R are uniform while ρ and the material properties vary in general across the interface: $u_{e-1} = u_e = u_{e+1} = u > 0$, $p_{e-1} = p_e = p_{e+1} = p$, and $T_{e-1} = T_e = T_{e+1} = T$, while $\rho_{e-1} \neq \rho_e \neq \rho_{e+1}$, $\gamma_{e-1} \neq \gamma_e \neq \gamma_{e+1}$ and $(c_v)_{e-1} \neq (c_v)_e \neq (c_v)_{e+1}$. For the volume fraction approach, $(\alpha^{(l)})_{e-1} \neq (\alpha^{(l)})_e \neq (\alpha^{(l)})_{e+1}$, $(\rho^{(l)}\alpha^{(l)})_{e-1} \neq (\rho^{(l)}\alpha^{(l)})_e \neq (\rho^{(l)}\alpha^{(l)})_{e+1}$, and similarly for the mass fraction approach. We assume the radiation field is initially in equilibrium, with $E_R = a_R T^4$. In this case, the source, parabolic, and non-conservative product terms are identically zero initially. Without loss of generality, we consider a $P = 1$ representation using hierarchical reconstruction limiting with a minmod reconstruction. In each cell, the solution is represented by a linear expansion:

$$\begin{aligned} \rho(x) &= \widehat{\rho}^0 + \widehat{\rho}^1 x, \qquad & \rho u(x) &= (\widehat{\rho u})^0 + (\widehat{\rho u})^1 x, \\ E(x) &= \widehat{E}^0 + \widehat{E}^1 x, \qquad & E_R(x) &= (\widehat{E_R})^0 + (\widehat{E_R})^1 x. \end{aligned} \tag{3.70}$$

After limiting, the solution is:

$$\begin{aligned} \widetilde{\rho}(x) &= \widetilde{\widehat{\rho}}^0 + \widetilde{\widehat{\rho}}^1 x, \qquad & \widetilde{\rho u}(x) &= \widetilde{(\widehat{\rho u})^0} + \widetilde{(\widehat{\rho u})^1} x, \\ \widetilde{E}(x) &= \widetilde{\widehat{E}^0} + \widetilde{\widehat{E}^1} x, \qquad & \widetilde{E_R}(x) &= \widetilde{(\widehat{E_R})^0} + \widetilde{(\widehat{E_R})^1} x. \end{aligned} \tag{3.71}$$

For density, the limiting procedure leads to $\widetilde{\widehat{\rho}}_e^0 = \widehat{\rho}_0^e$ and $\widetilde{\widehat{\rho}}_e^1 = \frac{1}{2}\text{minmod}(\widehat{\rho}_e^0 - \widehat{\rho}_{e-1}^0, \widehat{\rho}_{e+1}^0 - \widehat{\rho}_e^0)$. For momentum density, the limiting procedure preserves a constant velocity, $\widetilde{(\rho u)}_e = u\widetilde{\rho}_e$. To this point, the analysis is common to all three approaches (γ-based, volume fraction, mass fraction). As the material energy is examined, we consider each model individually.

3.6.2.1 γ approach

With the γ-based approach, the additional state variables are expanded linearly:

$$\left(\frac{1}{\gamma-1}\right)(x) = \widehat{\left(\frac{1}{\gamma-1}\right)}^0 + \widehat{\left(\frac{1}{\gamma-1}\right)}^1 x, \qquad (\rho c_v)(x) = \widehat{(\rho c_v)}^0 + \widehat{(\rho c_v)}^1 x. \tag{3.72}$$

After limiting these variables,

$$\widetilde{\left(\frac{1}{\gamma-1}\right)}(x) = \widetilde{\widehat{\left(\frac{1}{\gamma-1}\right)}}^0 + \widetilde{\widehat{\left(\frac{1}{\gamma-1}\right)}}^1 x, \qquad \widetilde{(\rho c_v)}(x) = \widetilde{\widehat{(\rho c_v)}}^0 + \widetilde{\widehat{(\rho c_v)}}^1 x. \tag{3.73}$$

Limiting the total energy density using the pressure-wise form of the equation of state,

$$\begin{aligned} \widetilde{\widehat{E}_e^1} = \frac{1}{2}\text{minmod}\Bigg\{ & p\left[\widehat{\left(\frac{1}{\gamma-1}\right)}_e^0 - \widehat{\left(\frac{1}{\gamma-1}\right)}_{e-1}^0\right] + \frac{u^2}{2}(\widehat{\rho}_e^0 - \widehat{\rho}_{e-1}^0), \\ & p\left[\widehat{\left(\frac{1}{\gamma-1}\right)}_{e+1}^0 - \widehat{\left(\frac{1}{\gamma-1}\right)}_e^0\right] + \frac{u^2}{2}(\widehat{\rho}_{e+1}^0 - \widehat{\rho}_e^0)\Bigg\}. \end{aligned} \tag{3.74}$$

Because $\text{minmod}(x_1+y_1, x_2+y_2) \neq \text{minmod}(x_1, x_2)+\text{minmod}(y_1, y_2)$, we cannot factor out the p from this equation, and we cannot assure that mechanical equilibrium is maintained. Limiting of the total energy density using the temperature-wise form of the equation of state produces:

$$\widetilde{\widehat{E}_e^1} = \frac{1}{2}\text{minmod}\Bigg\{ T\left[\widehat{(\rho c_v)}_e^0 - \widehat{(\rho c_v)}_{e-1}^0\right] + \frac{u^2}{2}(\widehat{\rho}_e^0 - \widehat{\rho}_{e-1}^0), \\ T\left[\widehat{(\rho c_v)}_{e+1}^0 - \widehat{(\rho c_v)}_e^0\right] + \frac{u^2}{2}(\widehat{\rho}_{e+1}^0 - \widehat{\rho}_e^0)\Bigg\}. \quad (3.75)$$

We cannot factor out T from this equation, and therefore cannot assure that thermal equilibrium is maintained.

However, we can enforce thermomechanical equilibrium by using HR limiting in a manner consistent with our goals. Extending the approach of Henry de Frahan et al. [196], we limit $E = \rho e + K$ in a manner that allows a constant pressure and temperature to be recovered. For the γ-based approach, we limit ρ, ρu, p, T, $1/(\gamma-1)$ and ρc_v, such that the total energy is reconstructed as follows:

$$\begin{aligned} \widetilde{\widehat{E}_e^n} &= \widetilde{\widehat{\rho e}_e^n} + \widetilde{\widehat{K}_e^n} \qquad \text{for } n = 1,\ 2,\ ...,\ P, \\ \widetilde{\widehat{E}_e^0} &= \widehat{E}_e^0 - \sum_{k=2,4,...} \frac{1}{(k+1)!}(\widetilde{\widehat{E}_e^k} - \widehat{E}_e^k), \end{aligned} \quad (3.76)$$

where the constraint on $n = 0$ enforces conservation of total energy. We reconstruct the kinetic energy $\widetilde{K}$ using the limited values $\widetilde{\rho}$ and $\widetilde{\rho u}$. The internal energy is calculated as:

$$\widetilde{\widehat{\rho e}_e^n} = \sum_{k=0}^{n} \binom{n}{k} \widetilde{\widehat{p}_e^{n-k}} \left(\widetilde{\frac{1}{\gamma-1}}\right)_e^k. \quad (3.77)$$

This limiting procedure is guaranteed to maintain pressure equilibrium and conserve mass, momentum, and energy. This form of the internal energy is used to compute

the pressure. We also calculate the internal energy as

$$\widetilde{\widehat{\rho e}_e^n} = \sum_{k=0}^{n} \binom{n}{k} \widetilde{\widehat{T}_e^{n-k}} \widetilde{(\widehat{\rho c_v})_e^k}. \tag{3.78}$$

This limiting procedure is guaranteed to maintain temperature equilibrium and conserve material energy. This form of the internal energy is used to compute the temperature.

3.6.2.2 Volume fraction approach

With the volume fraction approach, the additional state variables are expanded linearly:

$$\alpha^{(l)}(x) = (\widehat{\alpha^{(l)}})^0 + (\widehat{\alpha^{(l)}})^1 x, \qquad \rho^{(l)}\alpha^{(l)}(x) = (\widehat{\rho^{(l)}\alpha^{(l)}})^0 + (\widehat{\rho^{(l)}\alpha^{(l)}})^1 x. \tag{3.79}$$

After limiting these variables,

$$\widetilde{\alpha^{(l)}}(x) = \widetilde{(\widehat{\alpha^{(l)}})^0} + \widetilde{(\widehat{\alpha^{(l)}})^1} x, \qquad \widetilde{\rho^{(l)}\alpha^{(l)}}(x) = (\widetilde{\widehat{\rho^{(l)}\alpha^{(l)}}})_e^0 + \widetilde{(\widehat{\rho^{(l)}\alpha^{(l)}})}^1 x. \tag{3.80}$$

Limiting of the total energy density using the pressure-wise form of the equation of state gives,

$$\begin{aligned}\widetilde{\widehat{E}_e^1} = \frac{1}{2}\text{minmod}\Bigg\{ & p\left[\sum_l \left(\frac{\widehat{\alpha^{(l)}}}{\gamma^{(l)}-1}\right)_e^0 - \sum_l \left(\frac{\widehat{\alpha^{(l)}}}{\gamma^{(l)}-1}\right)_{e-1}^0\right] + \frac{u^2}{2}(\widehat{\rho}_e^0 - \widehat{\rho}_{e-1}^0) \\ & p\left[\sum_l \left(\frac{\widehat{\alpha^{(l)}}}{\gamma^{(l)}-1}\right)_{e+1}^0 - \sum_l \left(\frac{\widehat{\alpha^{(l)}}}{\gamma^{(l)}-1}\right)_e^0\right] + \frac{u^2}{2}(\widehat{\rho}_{e+1}^0 - \widehat{\rho}_e^0)\Bigg\}.\end{aligned} \tag{3.81}$$

Because $\text{minmod}(x_1+y_1, x_2+y_2) \neq \text{minmod}(x_1, x_2)+\text{minmod}(y_1, y_2)$, we cannot factor out the p from this equation, and we cannot assure that mechanical equilibrium is maintained. Limiting of the total energy density using the temperature-wise form of

the equation of state produces:

$$\widetilde{\widehat{E}_e^1} = \frac{1}{2}\text{minmod}\Bigg\{ T\left[\sum_l \widehat{(\rho^{(l)}\alpha^{(l)}c_v^{(l)})}_e^0 - \sum_l \widehat{(\rho^{(l)}\alpha^{(l)}c_v^{(l)})}_{e-1}^0\right] + \frac{u^2}{2}(\widehat{\rho}_e^0 - \widehat{\rho}_{e-1}^0)$$
$$T\left[\sum_l \widehat{(\rho^{(l)}\alpha^{(l)}c_v^{(l)})}_{e+1}^0 - \sum_l \widehat{(\rho^{(l)}\alpha^{(l)}c_v^{(l)})}_e^0\right] + \frac{u^2}{2}(\widehat{\rho}_{e+1}^0 - \widehat{\rho}_e^0)\Bigg\}. \quad (3.82)$$

We cannot factor out the T from this equation, and we cannot assure that thermal equilibrium is maintained.

However, we can enforce thermomechanical equilibrium by using HR limiting in a manner consistent with our goals. For the volume fraction method, we limit ρ, ρu, p, T, $\alpha^{(l)}$ and $\rho^{(l)}\alpha^{(l)}$, such that the total energy is reconstructed as follows:

$$\begin{aligned} \widetilde{\widehat{E}_e^n} &= \widetilde{\widehat{\rho e}_e^n} + \widetilde{\widehat{K}_e^n}, \quad \text{for} \quad n = 1, ..., P, \\ \widetilde{\widehat{E}_e^0} &= \widehat{E}_e^0 - \sum_{k=2,4,...} \frac{1}{(k+1)!}(\widetilde{\widehat{E}_e^k} - \widehat{E}_e^k), \end{aligned} \quad (3.83)$$

where the constraint on $n = 0$ enforces conservation of total energy. We reconstruct the kinetic energy K according to the limited values $\widetilde{\rho}$ and $\widetilde{\rho u}$. The internal energy is calculated as:

$$\widetilde{\widehat{\rho e}_e^n} = \sum_l \sum_{k=0}^{n} \binom{n}{k} \widetilde{\widehat{p}_e^{n-k}} \widetilde{(\widehat{\alpha^{(l)}})_e^k} \left(\frac{1}{\gamma^{(l)} - 1}\right). \quad (3.84)$$

This limiting procedure is guaranteed to maintain pressure equilibrium and conserve mass, momentum, and energy. This form of the internal energy is used to compute the pressure. We also calculate the internal energy as

$$\widetilde{\widehat{\rho e}_e^n} = \sum_l \sum_{k=0}^{n} \binom{n}{k} \widetilde{\widehat{T}_e^{n-k}} \widetilde{(\widehat{\rho^{(l)}\alpha^{(l)}})_e^k} c_v^{(l)}. \quad (3.85)$$

This limiting procedure is guaranteed to maintain temperature equilibrium and conserve material energy. This form of the internal energy is used to compute the temperature.

3.6.2.3 Mass fraction approach

With the mass fraction approach, the additional state variables are expanded linearly:

$$(\frac{\rho z^{(l)}}{\rho^{(l)}})(x) = (\frac{\widehat{\rho z^{(l)}}}{\rho^{(l)}})^0 + (\frac{\widehat{\rho z^{(l)}}}{\rho^{(l)}})^1 x, \qquad \rho z^{(l)}(x) = (\widehat{\rho z^{(l)}})^0 + (\widehat{\rho z^{(l)}})^1 x. \tag{3.86}$$

After limiting these variables,

$$(\widetilde{\frac{\rho z^{(l)}}{\rho^{(l)}}})(x) = (\frac{\widetilde{\widehat{\rho z^{(l)}}}}{\rho^{(l)}})^0 + (\frac{\widetilde{\widehat{\rho z^{(l)}}}}{\rho^{(l)}})^1 x, \qquad \widetilde{\rho z^{(l)}}(x) = (\widetilde{\widehat{\rho z^{(l)}}})^0 + (\widetilde{\widehat{\rho z^{(l)}}})^1 x. \tag{3.87}$$

Limiting of the total energy density using the pressure-wise form of the equation of state gives,

$$\begin{aligned}\widetilde{E}_1^e = \frac{1}{2}\text{minmod}\Bigg\{ & p\left[\sum_l \left(\frac{\widehat{\rho z^{(l)}}}{\rho^{(l)}(\gamma^{(l)}-1)}\right)_e^0 - \sum_l \left(\frac{\widehat{\rho z^{(l)}}}{\rho^{(l)}(\gamma^{(l)}-1)}\right)_{e-1}^0\right] + \frac{u^2}{2}(\widehat{\rho}_e^0 - \widehat{\rho}_{e-1}^0), \\ & p\left[\sum_l \left(\frac{\widehat{\rho z^{(l)}}}{\rho^{(l)}(\gamma^{(l)}-1)}\right)_{e+1}^0 - \sum_l \left(\frac{\widehat{\rho z^{(l)}}}{\rho^{(l)}(\gamma^{(l)}-1)}\right)_e^0\right] + \frac{u^2}{2}(\widehat{\rho}_{e+1}^0 - \widehat{\rho}_e^0)\Bigg\}.\end{aligned} \tag{3.88}$$

Because $\text{minmod}(x_1+y_1, x_2+y_2) \neq \text{minmod}(x_1, x_2)+\text{minmod}(y_1, y_2)$, we cannot factor out the p from this equation, and we cannot assure that mechanical equilibrium is maintained. Limiting of the total energy density using the temperature-wise form of the equation of state produces:

$$\begin{aligned}\widetilde{E}_1^e = \frac{1}{2}\text{minmod}\Bigg\{ & T\left[\sum_l (\widehat{\rho z^{(l)} c_v^{(l)}})_e^0 - \sum_l (\widehat{\rho z^{(l)} c_v^{(l)}})_{e-1}^0\right] + \frac{u^2}{2}(\widehat{\rho}_e^0 - \widehat{\rho}_{e-1}^0), \\ & T\left[\sum_l (\widehat{\rho z^{(l)} c_v^{(l)}})_{e+1}^0 - \sum_l (\widehat{\rho z^{(l)} c_v^{(l)}})_e^0\right] + \frac{u^2}{2}(\widehat{\rho}_{e+1}^0 - \widehat{\rho}_e^0)\Bigg\}.\end{aligned} \tag{3.89}$$

However, we can enforce thermomechanical equilibrium by using HR limiting in a manner consistent with our goals. We cannot factor out the T from this equation,

and we cannot assure that temperature equilibrium is maintained.

For the volume fraction method, we limit ρ, ρu, p, T, $\rho z^{(l)}/\rho^{(l)}$ and $\rho z^{(l)}$, such that the total energy is reconstructed as follows:

$$\begin{aligned}\widetilde{\widehat{E}_e^n} &= \widetilde{\widehat{\rho e}_e^n} + \widetilde{\widehat{K}_e^n}, \quad \text{for} \quad n = 1, ..., P, \\ \widetilde{\widehat{E}_e^0} &= \widehat{E}_e^0 - \sum_{k=2,4,...} \frac{1}{(k+1)!}(\widetilde{\widehat{E}_e^k} - \widehat{E}_e^k),\end{aligned} \tag{3.90}$$

where the constraint on $n = 0$ enforces conservation of total energy. We reconstruct the kinetic energy K according to the limited values of ρ and ρu. The internal energy is calculated as:

$$\widetilde{\widehat{\rho e}_e^n} = \sum_l \sum_{k=0}^{n} \binom{n}{k} \widetilde{\widehat{p}_e^{n-k}} \left(\frac{\widetilde{\widehat{\rho z^{(l)}}}}{\rho^{(l)}} \right)_e^k \left(\frac{1}{\gamma^{(l)} - 1} \right). \tag{3.91}$$

This limiting procedure is guaranteed to maintain pressure equilibrium and conserve mass, momentum, and material energy. This form of the internal energy is used to compute the pressure. We also calculate the internal energy as

$$\widetilde{\widehat{\rho e}_e^n} = \sum_l \sum_{k=0}^{n} \binom{n}{k} \widetilde{\widehat{T}_e^{n-k}} (\widetilde{\widehat{\rho z^{(l)}}})_e^k c_v^{(l)}. \tag{3.92}$$

This limiting procedure is guaranteed to maintain temperature equilibrium and conserve material energy. This form of the internal energy is used to compute the temperature.

The limiting procedure described for each model enables us to simultaneously prevent pressure and temperature errors at interfaces. The form of equations (3.76), (3.83), (3.90) guarantees that the total material energy is conserved with respect to this limiting procedure, i.e., $\int_{\Omega_e} E \mathrm{d}x = \int_{\Omega_e} \widetilde{E} \mathrm{d}x$. For the remainder of this work, we refer to this procedure as pT-limiting to distinguish it from other approaches.

As we have assumed that the radiation field is isotropic, we may directly apply HR limiting to the radiation energy density without issue. However, if this was not the case, as with variable Eddington tensor methods [74], this limiting procedure could be extended to ensure oscillations in radiation pressure are not introduced.

3.6.3 Solution-adaptive approach

In general, limiting procedures reduce the order of accuracy of the method. Therefore, it is advantageous to apply limiting only where it is necessary to reduce oscillations to thereby reduce the amount of numerical dissipation introduced [226]. Numerical dissipation may be problematic when simulating broadband problems such as interfacial instabilities or turbulence. To effectively control the application of dissipation, we follow a solution-adaptive approach based on a discontinuity sensor, which identifies the computational cells in which discontinuities are located. It is critical that this sensor be discerning and compact, as the efficiency, accuracy, and stability of the overall scheme rely on its ability to apply limiting where required. The DG method offers important advantages over other methods. The compact stencil allows limiting to be applied at flagged cells while the optimal order of accuracy can be achieved in the very next cell. We extend the sensor of Henry de Frahan et al. [196] to radiation hydrodynamics, which requires one additional sensor evaluation to detect nonlinear radiative heat waves.

First we detect contact waves, where L and R denote the cell-average value in the left and right cell of an edge, respectively. The sensor quantity is:

$$\xi = \frac{|\Delta\alpha_2^*|}{\rho_L + \rho_R}, \qquad \Xi = \frac{2\xi}{(1+\xi)^2}, \tag{3.93}$$

where $\Delta\alpha_2^*$ is the Roe-averaged wave strength associated with the contact wave in

the system (3.1),

$$\Delta\alpha_2^* = \Delta\rho - \frac{\Delta(p + p_R)}{(a^*)^2}. \tag{3.94}$$

The the Roe-averaged sound speed is $a^* = \sqrt{(c_s^*)^2 + (c_R^*)^2}$, where the Roe-averaged hydrodynamic sound speed c_s^* is calculated from the Roe-averaged enthalpy and velocity as in the familiar hydrodynamic case, and $c_R^* = \sqrt{\frac{1}{3}h_R^*}$, where the radiation enthalpy $h_R = \frac{E_R + p_R}{\rho}$ is to be Roe-averaged. Similarly, we use a sensor to detect material interfaces:

$$\zeta = \frac{|\gamma_R - \gamma_L|}{\gamma_L + \gamma_R}, \qquad Z = \frac{2\zeta}{(1+\zeta)^2}. \tag{3.95}$$

We use this sensor regardless of the interface capturing model we use, so $\gamma_{L/R}$ must be calculated from the cell-average value of $\alpha^{(l)}$ or $\rho z^{(l)}/\rho^{(l)}$. We use the threshold value of 0.01 for these sensors; if Ξ or Z are greater than this value, we limit both cells L and R.

To detect shockwaves, we test the Lax entropy condition, given by:

$$u_L - a_L > u^* - a^* > u_R - a_R, \tag{3.96}$$

which is true for a physical shockwave. If this condition is satisfied, then we use the sensor

$$\phi = \frac{|p_R - p_L|}{p_L + p_R}, \qquad \Phi = \frac{2\phi}{(1+\phi)^2}, \tag{3.97}$$

with a threshold of 0.001. Lastly, we introduce a final sensor to detect nonlinear radiative heat waves, which form naturally from nonlinear diffusive processes and require limiting. This sensor is given by,

$$\psi = \frac{|(p_R)_R - (p_R)_L|}{(p_R)_L + (p_R)_R}, \qquad \Psi = \frac{2\psi}{(1+\psi)^2}. \tag{3.98}$$

We use a threshold of 0.01 for this sensor.

3.7 Verification

To numerically demonstrate the properties of our method outlined above, we solve the radiation-hydrodynamics equations in System (3.1) non-dimensionalized using the convention in Section 1.3.3 for a series of test problems. We evaluate the L_∞ error norm of the variable q to demonstrate convergence rates:

$$L_\infty(q) = \max_{e=1,\dots,N_e} \Big| \frac{1}{\Delta x} \int_{\Omega_e} (q - q_{exact}) \mathrm{d}x \Big|. \tag{3.99}$$

We evaluate this integral using $2P+1$ quadrature points. For each problem in this section, we use the non-dimensional parameter values $1/\mathcal{R} = 1$ and $c/a_0 = 10^2$. In each case, simulations are run with a Courant-Friedrichs-Lewy number of 0.85 and a von Neumann number of 0.45.

3.7.1 High-order accuracy – smooth distribution in γ

We report the convergence of our method using a smooth 1-D interface advection problem similar to that used in Ref. [196] to demonstrate that our proposed scheme is high-order accurate while preventing spurious pressure and temperature errors. We initialize a 1-D periodic domain $x \in [-1, 1]$ in thermomechanical equilibrium:

$$\begin{pmatrix} \rho \\ u \\ p \\ \gamma \end{pmatrix} = \begin{pmatrix} 1 + 0.2\cos(3\pi x) \\ 1.0 \\ 1.0 \\ 1.4 + 0.2\cos(\pi x) \end{pmatrix}. \tag{3.100}$$

We initialize the radiation pressure as $p_R = p$, from which we compute the radiation energy density $E_R = 3p_R$, and the corresponding equilibrium temperature $T = (E_R)^{1/4}$, which gives $T \approx 1.316$. We show results for the γ-based method only, as the convergence rate results for volume/mass fraction are the same. We set

constant and uniform opacities such that $D_R = \sigma_P = 10^{-4}$ initially.

The L_∞ error for T, p, $1/(\gamma - 1)$, and ρc_v vs. cell size Δx are shown in Figure 3.1 after one period of advection without limiting, with direct limiting of the state variables $\mathbf{q}^h$, and with pT-limiting for $P = 2$. For this problem, we limit all elements at each Runge-Kutta sub-step for the cases shown with limiting. Our DG method without limiting converges at a rate of $2P+1$, which is the expected ideal rate for the discontinuous Galerkin method as described in Section 3.5.1. As we solve the appropriate forms of the transport equations derived in Section 3.6.1, no errors affect the pressure and temperature fields in this case and the errors in these variables are near machine precision. The DG method with limiting of the state variables $\mathbf{q}^h$ converges at a rate of $P + 1$, which is the expected rate for the discontinuous Galerkin method with the HR limiting scheme. This manner of applying HR limiting introduces errors in the pressure and temperature fields, as we have demonstrated, and these variables now feature significant errors that converge at the expected rate. The DG method with the pT limiting scheme converges with an order of accuracy of $P + 1$, indicating that our pT limiting scheme, including reconstruction of the total material energy, converges at the ideal rate for HR limiting. As this limiting scheme is designed to prevent errors in pressure and temperature, the errors in these variables are near machine precision once again. This test problem demonstrates that our overall method, including pT limiting, is high-order accurate.

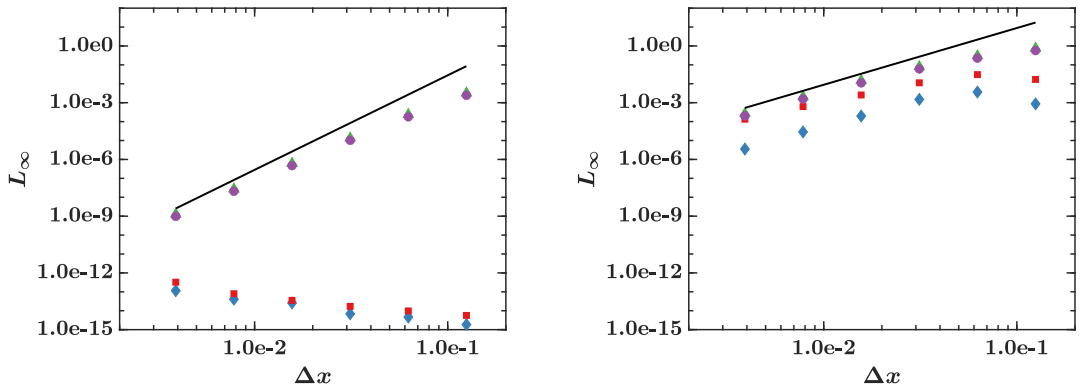

(a) No limiting

(b) Limiting $\mathbf{q}^h$

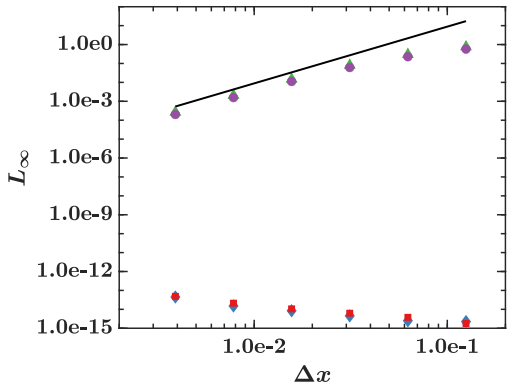

(c) pT limiting

Figure 3.1: Normalized L_∞ error norm for the 1-D smooth advection problem without limiting (a), with direct limiting of the state variables $\mathbf{q}^h$ (b), and with pT limiting (c). Errors are shown for material pressure (blue diamonds), temperature (red squares), $1/(\gamma-1)$ (green triangles), and ρc_v (purple circles). Guide lines shows slopes of $2P+1$ (a,b) and $P+1$ (c).

3.7.2 Preserving thermomechanical equilibrium – sharp interface advection

We consider the advection of a 1-D sharp interface to demonstrate that our overall scheme preserves thermomechanical equilibrium for material interfaces. We initialize

a periodic domain $x \in [-1, 1]$ according to:

$$(\rho,\ u,\ p,\ \gamma) = \begin{cases} (1.0,\ 1.0,\ 1.0,\ 5/3), & |x| < 0.5 \\ (0.1,\ 1.0,\ 1.0,\ 7/5), & \text{otherwise.} \end{cases} \tag{3.101}$$

The radiation pressure is $p_R = p$, from which we compute the radiation energy density and the equilibrium temperature as in the verification problem in Section 3.7.1. To highlight the effect of optical properties of the material, we consider two cases of opacities. These opacities are set such that, initially,

$$(D_R,\ \sigma_P) = \begin{cases} (10^{-4},\ 10^{-4}), & \text{(a) weak source/diffusion,} \\ (1,\ \ \ \ \ \ 1), & \text{(b) strong source/diffusion.} \end{cases} \tag{3.102}$$

We use a uniform mesh of 128 cells with $P = 2$. The volume and mass fraction approaches we derived are mathematically equivalent, so we show results for the γ and volume fraction approaches. To demonstrate the errors that can occur and their mechanisms of propagation, we compare our pT limiting procedure with three other approaches: (i) direct limiting of the state variables $\mathbf{q}^h$, (ii) limiting for pressure equilibrium only as in Equations (3.77) and (3.84), and (iii) limiting for temperature equilibrium only as in Equations (3.78) and (3.85). For this problem, we limit all elements at each Runge-Kutta sub-step. Each approach uses the transport equations derived in Section 3.6.1, so that the sole source of pressure and temperature errors is the limiting procedure.

The Figures 3.2 and 3.4 show pointwise error profiles after one period of advection for the four approaches for the γ-based and volume fraction approaches, respectively. As the mass fraction and volume fraction approaches are mathematically equivalent, we do not show results for mass fraction. The L_∞ errors in Figures 3.3 and 3.5 show how these errors develop over time. Significant errors from the interface treatment

have developed from all methods except pT limiting. These errors in temperature and pressure cause errors in velocity through the pressure in the momentum equation (3.1b). The magnitude and growth rate of the errors are much larger with strong source/diffusion effects. We note that the mechanism of propagation of temperature errors is different from that of pressure errors, as temperature does not appear in the divergence-form hyperbolic fluxes of the system (3.1). Temperature errors propagate to other variables through the radiation-material interaction terms. As the importance of these terms decreases, temperature errors become inconsequential to the other flow variables, as is the case in simulations of the Euler equations. This is why the pressure and velocity L_∞ errors are nearly equivalent in the case of limiting for pressure equilibrium only and pT limiting for the weak radiation case. The radiation-hydrodynamics equations contain physical mechanisms that make a physically consistent treatment of temperature especially critical. We conclude that the pT limiting scheme maintains thermomechanical equilibrium to an acceptable margin of error for the problem under consideration.

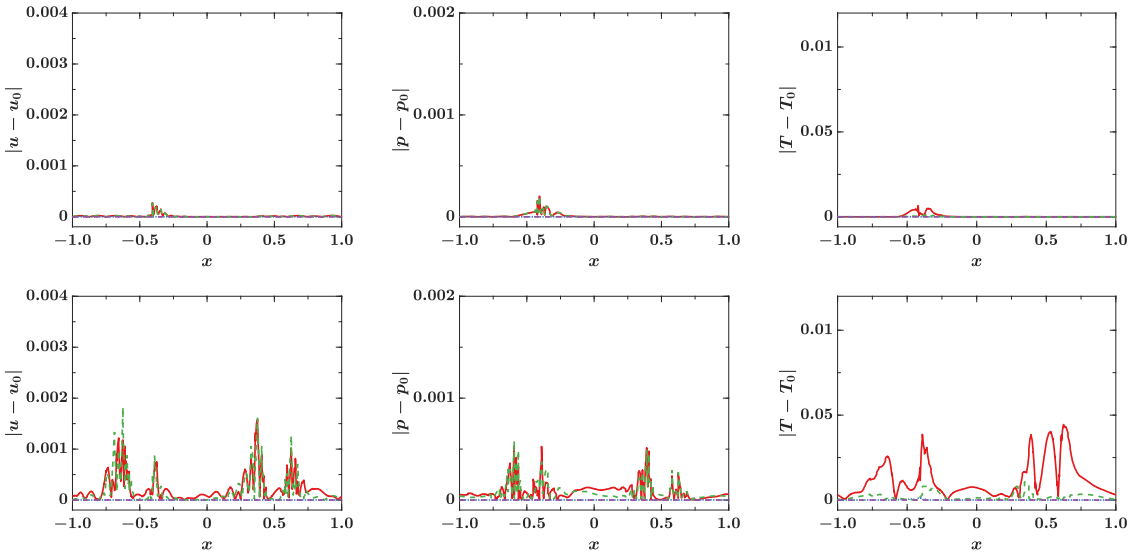

Figure 3.2: Pointwise error for the 1-D sharp interface advection problem with the γ-based method for weak source/diffusion (top row) and strong source/diffusion (bottom row) effects. Limiting schemes: direct limiting of state variables $\mathbf{q}^h$ (red solid line), pressure equilibrium only (green dashed line), temperature equilibrium only (blue dotted line), pT limiting (purple dashed line).

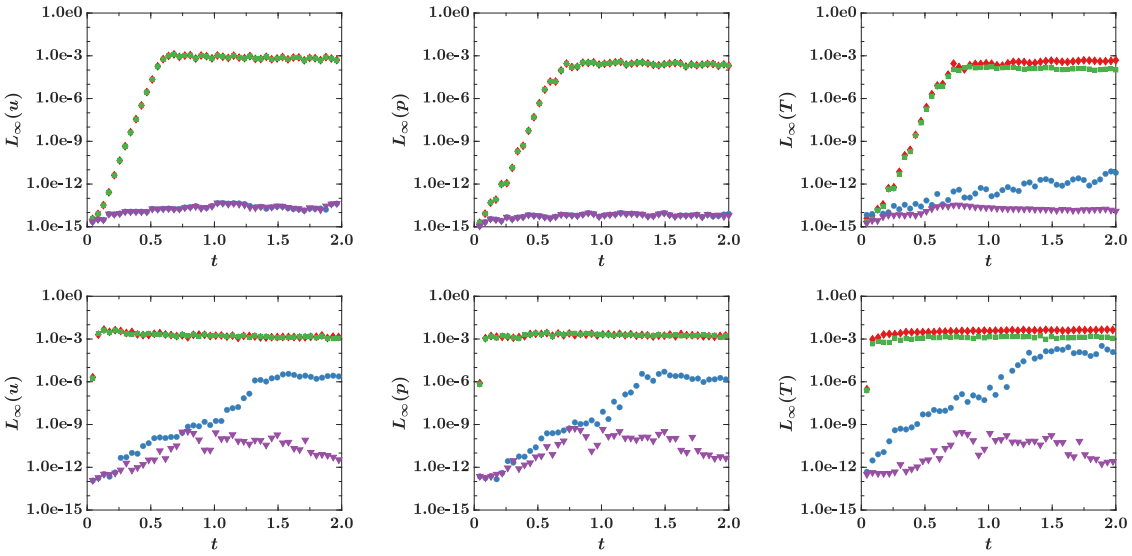

Figure 3.3: L_∞ error vs. time for the 1-D sharp interface advection problem with the γ-based method for weak source/diffusion (top row) and strong source/diffusion (bottom row) effects. Limiting schemes: direct limiting of state variables $\mathbf{q}^h$ (red solid line), pressure equilibrium only (green dashed line), temperature equilibrium only (blue dotted line), pT limiting (purple dashed line

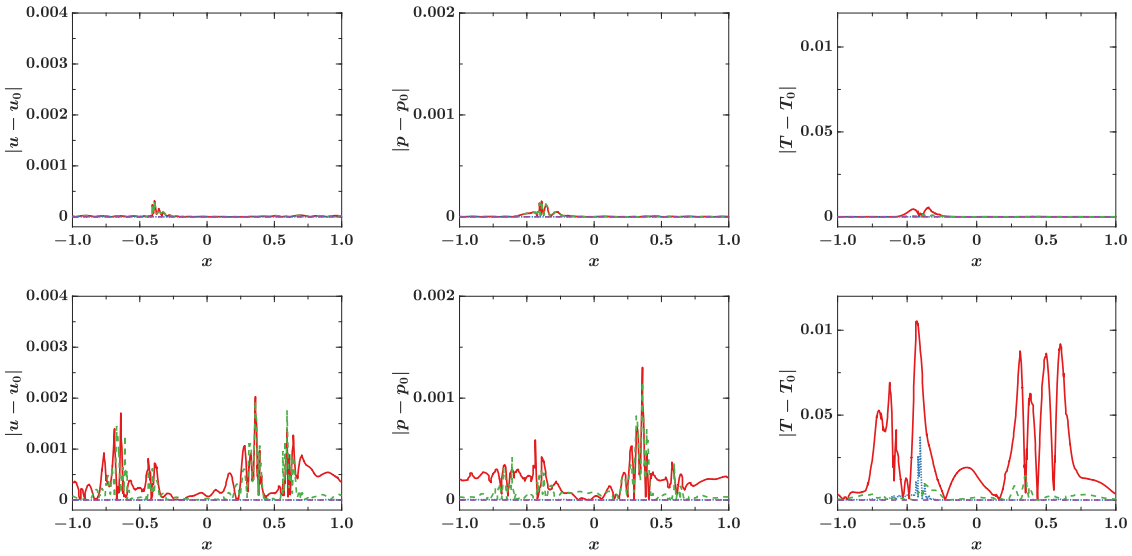

Figure 3.4: Pointwise error for the 1-D sharp interface advection problem with the volume fraction method for weak source/diffusion (top row) and strong source/diffusion (bottom row) effects. Limiting schemes: conserved variables (red solid line), pressure equilibrium only (green dashed line), temperature equilibrium only (blue dotted line), pT limiting (purple dashed line

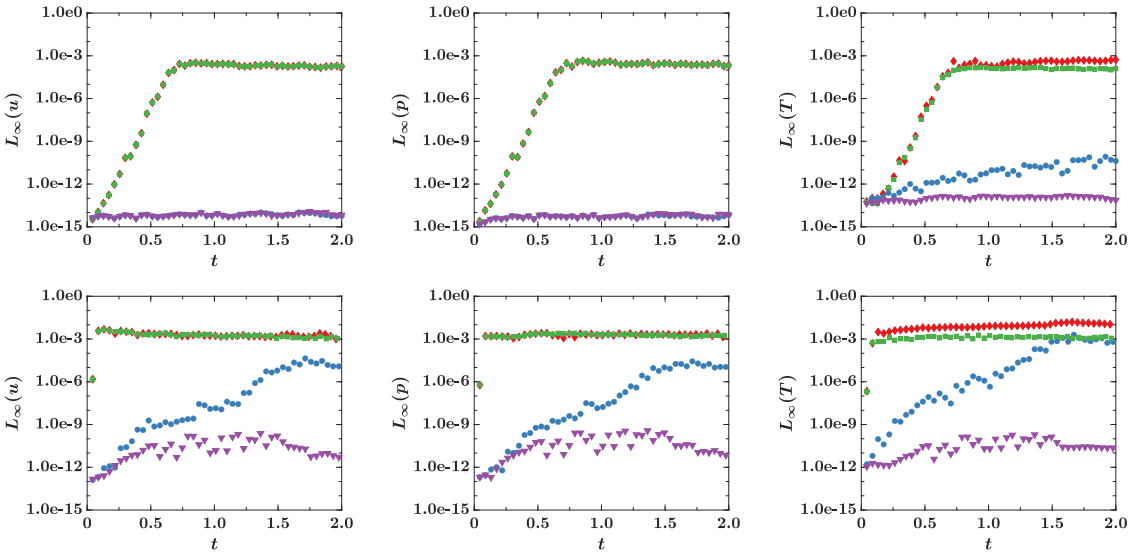

Figure 3.5: L_∞ error vs. time for the 1-D sharp interface advection problem with the volume fraction method for weak source/diffusion (top row) and strong source/diffusion (bottom row) effects. Limiting schemes: conserved variables (red solid line), pressure equilibrium only (green dashed line), temperature equilibrium only (blue dotted line), pT limiting (purple dashed line

3.7.3 Multifluid radiative shock tube

To demonstrate the applicability of our method to HED problems, we consider a 1-D shock tube problem, as shock tubes are commonly used in HED physics to study radiative shockwaves [6] and hydrodynamic instabilities [227, 228]. We modify the shock tube problem of Swesty and Myra [229] with 1-D initial conditions in $x \in [-1, 1]$ given by:

$$(\rho,\ u,\ p,\ \gamma,\ E_R) = \begin{cases} (1.0,\ 0.0,\ 1.0,\ 5/3,\ 1.0), & x < 0.5, \\ (0.125,\ 0.0,\ 0.1,\ 7/5,\ 0.1), & x > 0.5. \end{cases} \tag{3.103}$$

We initialize the temperature in equilibrium with the radiation field. We define opacities such that, initially, $(D_R,\ \sigma_P) = (10^{-4},\ 10^{-4})$. We solve this problem with 128 cells with $P = 2$, and compare to a reference solution computed with 512 cells. For this numerical test, we use the sensor developed in Section 3.6.3. Figure 3.6 shows the results using the γ-based model at time $t = 0.16$, and Figure 3.7 shows the results using the volume fraction model. For our pT limiting approach, no errors are visible at the material contact, located near $x = 0.65$, for either approach, and the interface and shock appear well-captured with this resolution. These results indicate that our approach resolves material contacts, as well as material interfaces, without generating temperature errors in the form of spikes or pressure errors in the form of oscillations.

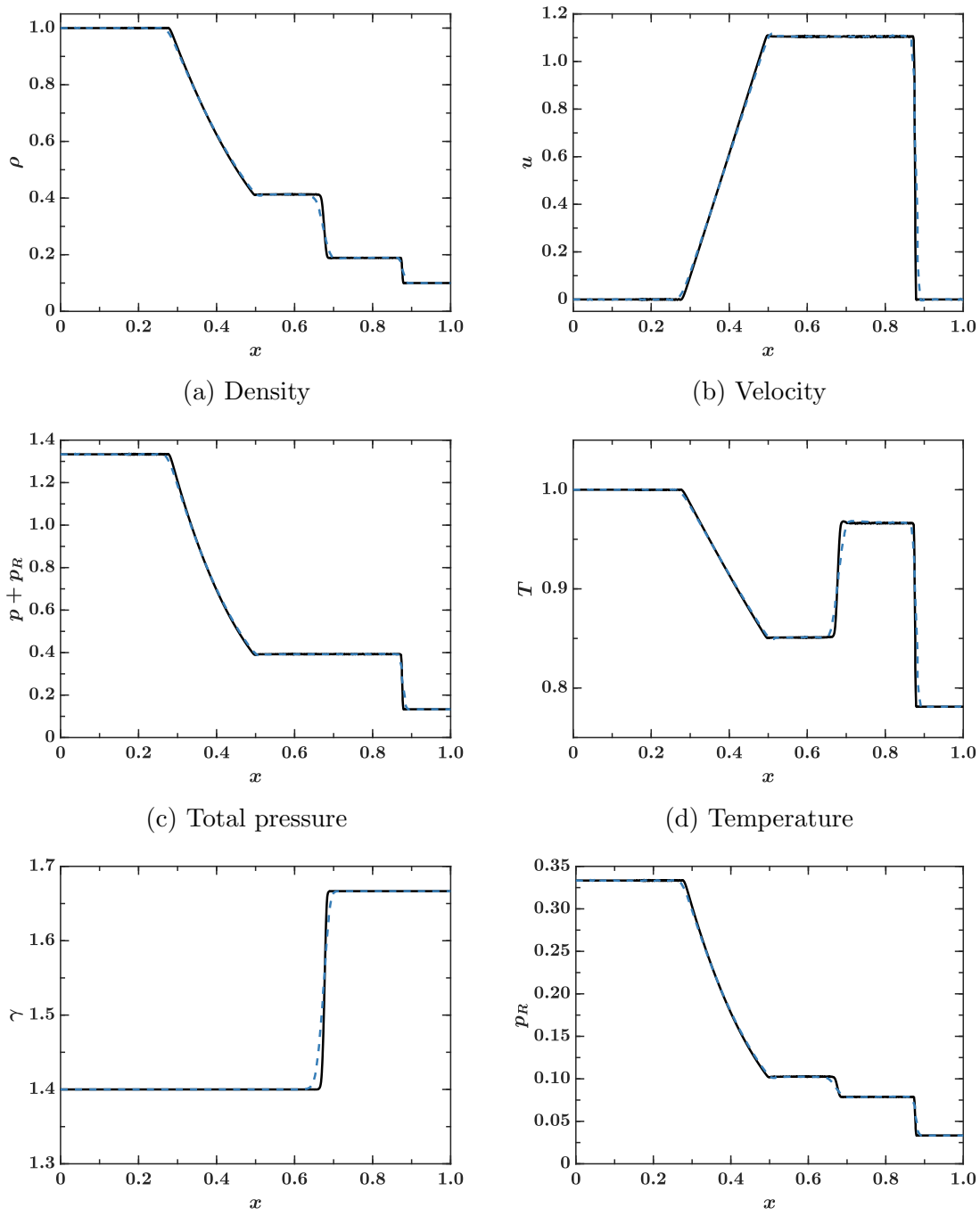

(a) Density

(b) Velocity

(c) Total pressure

(d) Temperature

(e) Ratio of specific heats

(f) Radiation pressure

Figure 3.6: Profiles for 1-D multifluid radiative shock tube problem for the γ-based approach at time $t = 0.16$. Shown here is our approach for preserving thermomechanical equilibrium (purple dashed line). Reference solution given by solid black line.

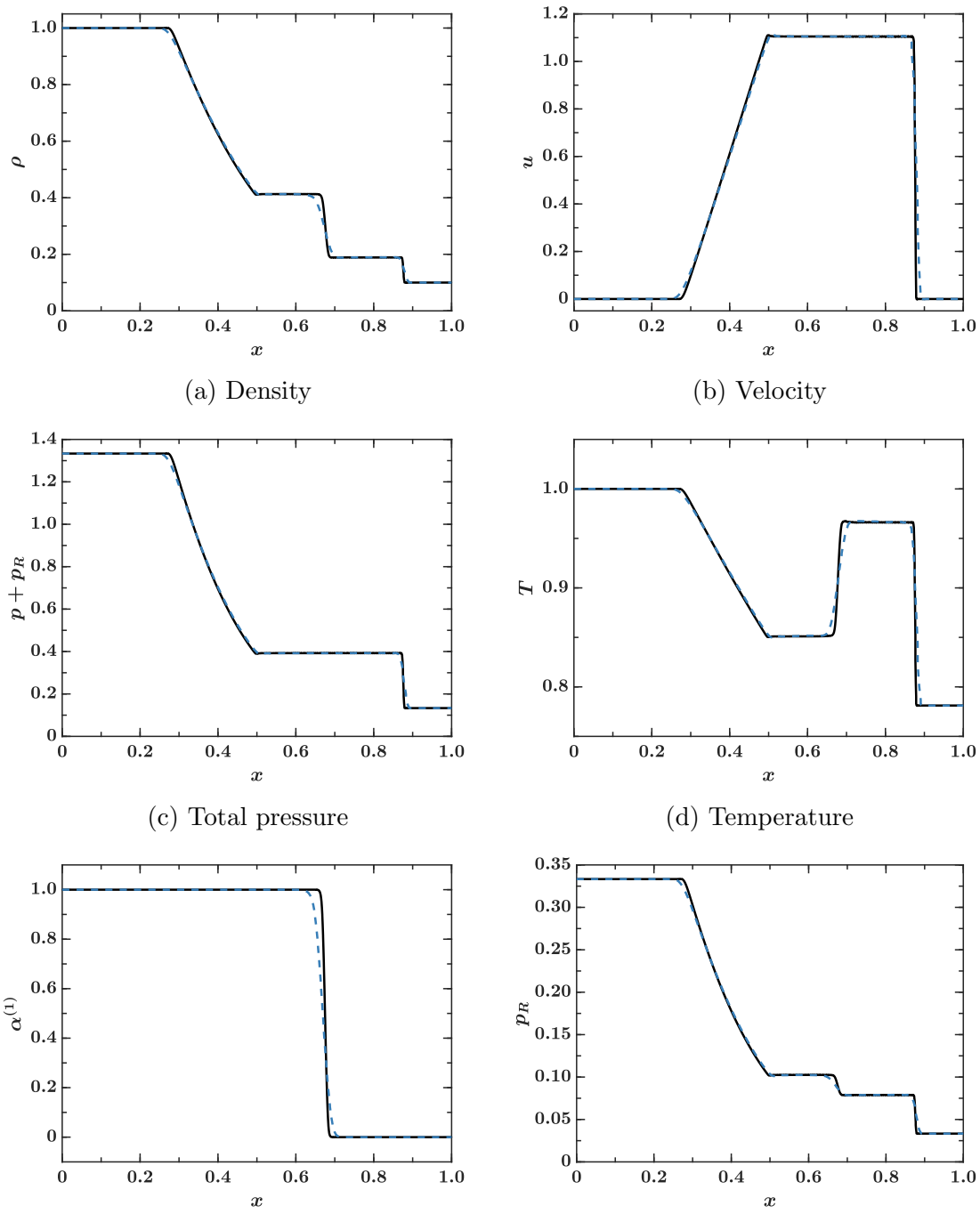

(a) Density

(b) Velocity

(c) Total pressure

(d) Temperature

(e) Volume fraction

(f) Radiation pressure

Figure 3.7: Profiles for 1-D multifluid radiative shock tube problem for the volume fraction approach at time $t = 0.16$. Shown here is our approach for preserving thermomechanical equilibrium (purple dashed line). Reference solution given by solid black line.

3.7.4 Multifluid blast wave

We consider the two-dimensional expansion of a hot, dense gas into a surrounding medium. Blast waves are relevant to HED phenomena, including core-collapse supernovae [56] and nuclear explosions [230]. We initialize a 2-D domain $x, y \in [0, 2]$ with the conditions:

$$(\rho,\ u,\ v,\ p,\ \gamma,\ E_R) = \begin{cases} (1.0,\ 0,\ 0,\ 1.0,\ \ 5/3,\ 1.0), & r < R_0, \\ (0.1,\ 0,\ 0,\ 0.01,\ 7/5,\ 0.1), & r > R_0. \end{cases} \tag{3.104}$$

where $r = \sqrt{x^2 + y^2}$, and the dense gas has an initial radius $R_0 = 1$. We smear the initial discontinuity in volume fraction across a few cells using a hyperbolic tangent function, following the approach in Ref. [231]. We define the opacities such that, initially, $(D_R,\ \sigma_P) = (10^{-4},\ 10^{-2})$ in the region $r < R_0$, and $(D_R,\ \sigma_P) = (10^{-3},\ 10^{-3})$ in the region $r > R_0$. These opacity values correspond to a higher opacity in the expanding dense gas. The mixture opacities are calculated according to Equation (3.15). We solve this problem on a structured 60×60 rectangular mesh with a $P = 1$ tensor product basis [232], using the volume fraction approach and our pT limiting scheme with the sensor developed in Section 3.6.3. Figure 3.8 shows results of the blast wave at time $t = 0.40$. We observe that no oscillations are visible in the pressure, and the temperature monotonically varies across the material contact, located near $r = 1.5$. We plot profiles along the 45° line in Figure 3.9, where we observe that the pressure is non-oscillatory and the temperature profile is free of spikes/overshoots. This problem demonstrates that our method extends to two-dimensions, and can be used to study HED flows of practical importance.

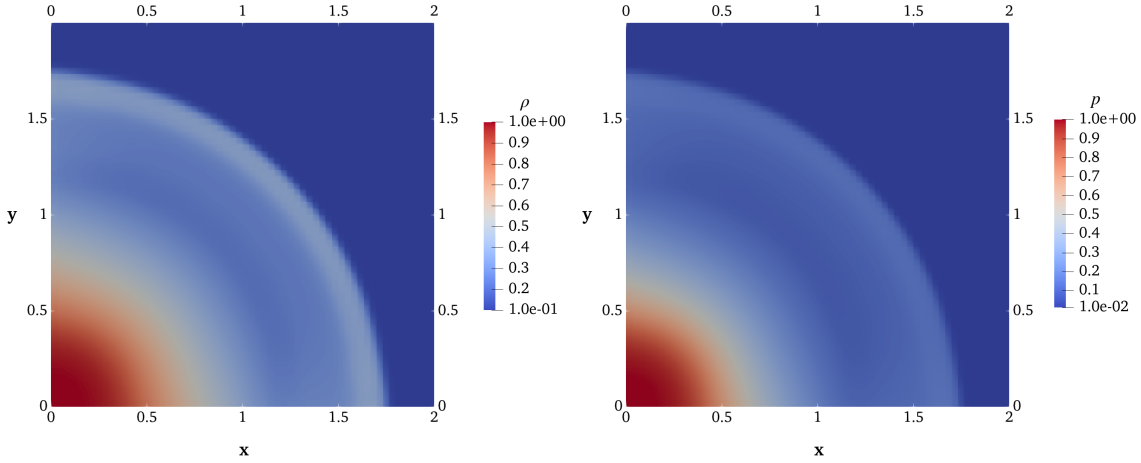

(a) Density

(b) Material pressure

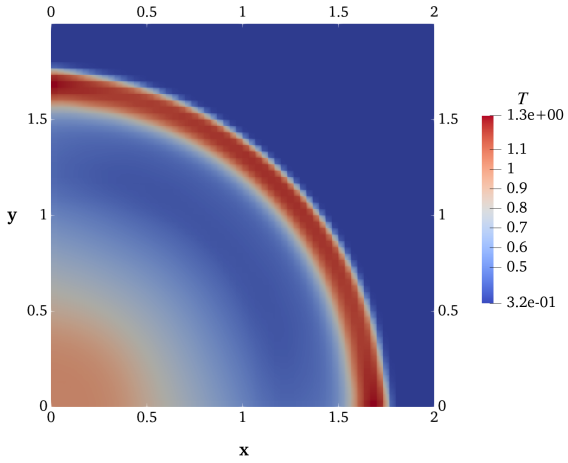

(c) Temperature

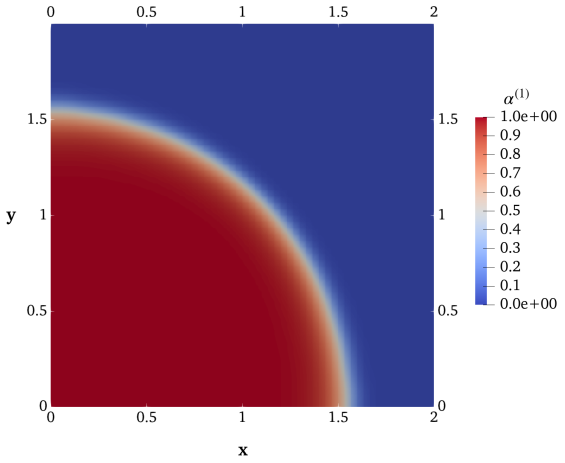

(d) Volume fraction

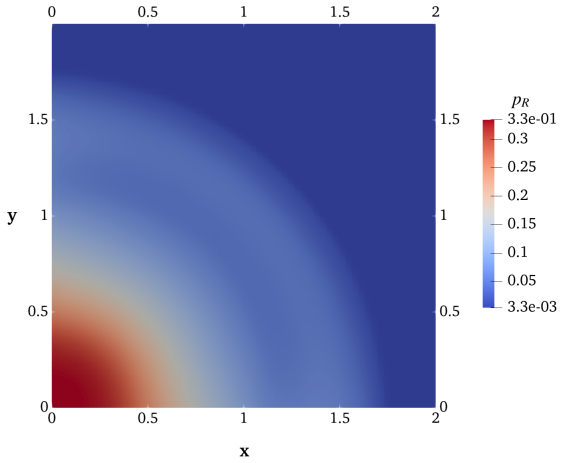

(e) Radiation pressure

Figure 3.8: State variables for 2-D multifluid blast wave problem at time $t = 0.40$.

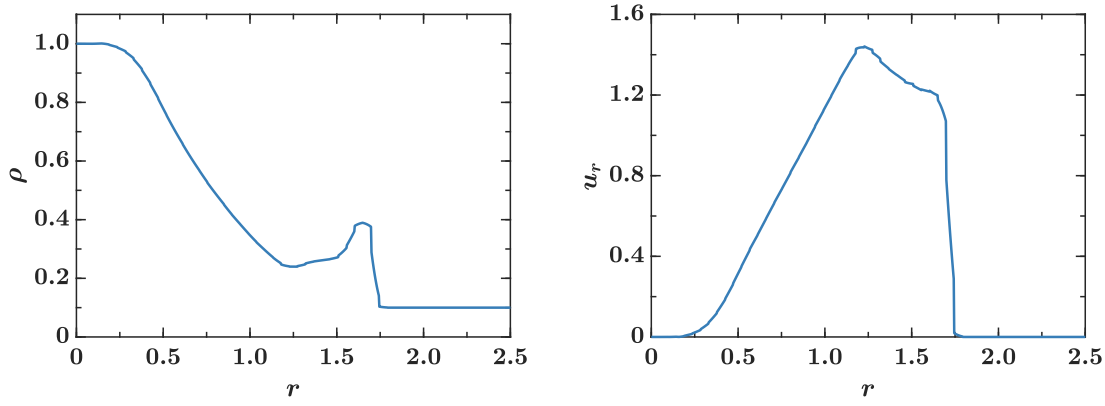

(a) Density (b) Velocity

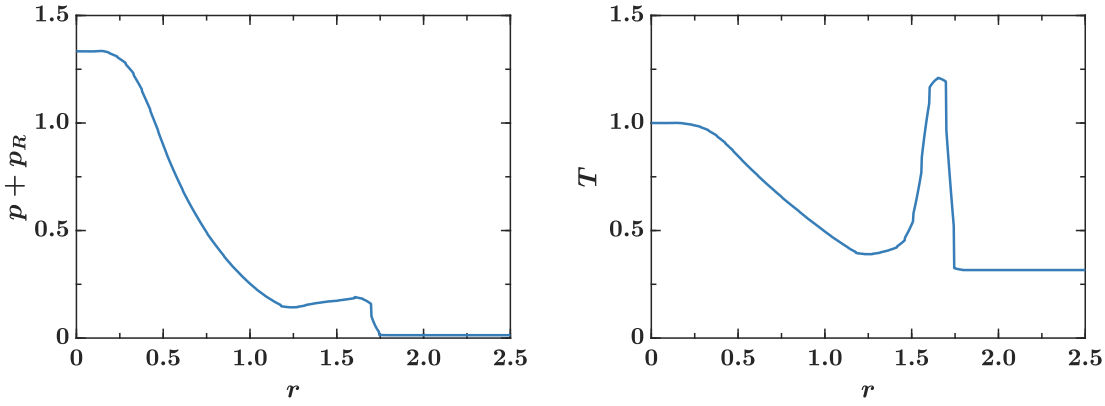

(c) Total pressure (d) Temperature

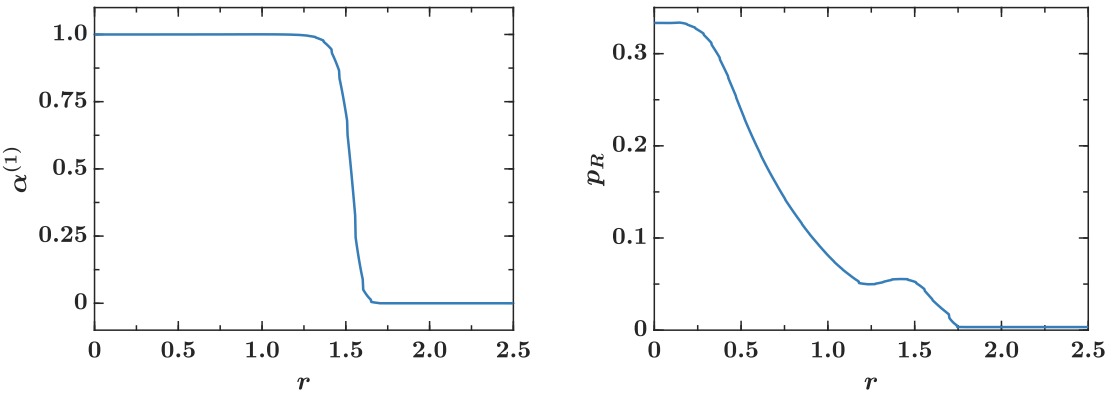

(e) Volume fraction (f) Radiation pressure

Figure 3.9: Lineout profiles for 2-D multifluid blast wave problem at time $t = 0.40$.

3.8 Conclusion

In this chapter, we presented a numerical method based on the discontinuous Galerkin (DG) scheme for computing multi-material flows governed by the radiation-hydrodynamics equations. We derive a method for the γ-based, volume fraction (i.e., five-equations model), and mass fraction approaches for interface capturing. The method is high-order accurate, conservative, compact, and prevents the development of unphysical errors in pressure and temperature at material interfaces and contacts. Preventing these errors is particularly important for the study of hydrodynamic instabilities and turbulent mixing, as temperature errors generated by inconsistent approaches propagate via the source, radiation diffusion, and radiation-material work terms to pollute other flow variables and affect small-scale flow features. This method is naturally adaptable to unstructured meshes, and is well-suited for scaling to large parallel computing architectures. These advantageous properties of our scheme rely on (i) the solution of additional mass conservation equations in the proper DG form for each interface-capturing approach, and (ii) the application of HR limiting in an appropriate manner to avoid pressure and temperature oscillations simultaneously. We develop a physics-based discontinuity sensor for the radiation-hydrodynamics equations to ensure that limiting is applied at discontinuities only. We demonstrate the properties of the method using one-dimensional verification problems, and applied the method to a 2-D problem relevant to HED science. This work demonstrates the potential for application of high-order methods based on interface capturing to be applied to HED science. Our approach can be readily extended to more complex physical models, including more extensive (or tabular, in the case of the volume-fraction approach) equations of state, three-temperature models, multigroup diffusion models, and variable Eddington tensor models.

CHAPTER IV

Summary and Future Work

4.1 Summary

This dissertation has introduced novel approaches in analytical modeling and numerical simulation in the field of high-energy-density (HED) science. Specifically, we have addressed two important deficiencies in available methods for the study of interaction between fluid flows and radiation fields. The objectives of this dissertation were to address these deficiencies by (i) developing a modeling approach for predicting the impulse and uncertainty in impulse in materials irradiated by x-ray sources subject to uncertainty, and (ii) developing an approach for numerical simulation of multi-material radiation hydrodynamics suitable for the study of mixing at material interfaces. The accomplishment of these objectives has ramifications in the field of HED physics, and enables high-fidelity study of phenomena with applications in astrophysics and inertial confinement fusion.

To accomplish the first objective:

- We derived a semi-analytical model for impulse-spectrum sensitivity from the Bethe, Bade, Averell and Yos (BBAY) model for impulse generation in an irradiated material. Both the BBAY model and the derived impulse-spectrum

sensitivity model require the energy of the blown-off material, $E_f(m)$, which is not known in general due to the complex partitioning of energy that occurs in the blow-off process.

- We utilized the Mercury Monte Carlo transport code and the Ares hydrodynamic code to conduct high-fidelity simulations of the x-ray deposition and blow-off processes for two materials of interest. We optimized these simulations to match data obtained from experiments on the NIF. These simulations were then used to obtain a fit to the $E_f(m)$ function using a fitting procedure that requires only the impulse and fluence for a few blow-off realizations.

- We augmented the BBAY and sensitivity models with the $E_f(m)$ function obtained from the fitting procedure and found that the sensitivity model obtains good agreement with the sensitivity evaluated directly from simulations. The fitting procedure for the model requires a small fraction of the simulations required by the sensitivity evaluations, and can also use experimental data as an input.

- We demonstrated the utility of this modeling approach in designing robust experiments by applying it to a source with an uncertain spectrum. First, we characterized the spectral uncertainty of an x-ray source due to shot-to-shot variation from an ensemble of spectral measurements. Then, we used this spectral uncertainty estimate to constrain the uncertainty in the impulse using our model.

This work enables low-cost prediction of important quantities relevant to the radiation-generated impulse in materials. It is our hope that our modeling approach will be useful in the study of these systems, as well as in the design of robust experiments in

this area.

To accomplish the second objective:

- We developed a numerical approach for the multi-material radiation-hydrodynamic equations based on the discontinuous Galerkin (DG) method. The discontinuous Galerkin method is arbitrarily high-order accurate, naturally extends to unstructured meshes, and is compact, enabling it to scale well on large parallel computing architectures.

- We derived the forms of transport equations that must be solved to prevent spurious pressure and temperature oscillations at material interfaces using the γ-based, volume fraction, and mass fraction approaches to interface capturing.

- We extended the solution-adaptive limiting approach of Ref. [196] to radiation hydrodynamics. This approach uses hierarchical reconstruction (HR) limiting in a manner that prevents spurious pressure and temperature oscillations and preserves cell-average values. We also extended the discontinuity sensor to the radiation-hydrodynamics equations. This limiting approach is high-order accurate, non-oscillatory, and conservative.

- We demonstrated with one-dimensional validation problems that our overall approach is high-order accurate and prevents oscillations at interfaces. By comparison with other approaches, we showed that appropriate treatment is especially important in radiation hydrodynamics, as mechanisms are present in the governing equations that amplify errors caused by inconsistent treatments.

- We applied our method to a two-dimensional blast wave problem relevant to HED physics.

This work introduces a method with favorable properties for performing high-resolution studies of hydrodynamic instabilities and turbulent mixing in HED systems. It is our hope that this work encourages the further application of high-order methods to the field of HED science.

4.2 Future work

This thesis invites several opportunities for improvements in the approaches to both objectives. Here, we discuss limitations of this work and related potential extensions, both in methodology as well as in application to a broader range of problems.

4.2.1 Improvements to x-ray blow-off modeling approach

Potential for improvement exists in our modeling approach. While directly differentiating the BBAY model is a straightforward approach to describing the impulse-spectrum sensitivity, more sophisticated methods for evaluating the sensitivity in a computationally feasible manner may exist. For example, variance decomposition methods [98] and Monte Carlo methods [99] could provide a more accurate evaluation of the sensitivity with reasonable cost. However, it is not clear that these methods could use only experimentally-obtained impulse/fluence data as inputs. Furthermore, our method for fitting the $E_f(m)$ function could be improved by more sophisticated methods for data-driven modeling, such as modal decomposition [233] and empirical dynamic modeling [234].

More research is needed to verify the limitations of our model. For example, the limitations of extending the model to a wider range of materials and sources, as well as higher radiation fluences, have not been studied. The BBAY model has been applied to describe blow-off caused by energy deposition from electron beams as well [119]. The case of laser-driven x-ray blow-off is currently being studied [235] experimentally. It would be interesting to apply our modeling approach to systems driven by particle

and laser beams. This would likely require using a different approach for evaluating the deposited energy $E(m)$, but theoretically the BBAY model should be applicable to these systems, as the fundamental assumptions are valid in these cases as well.

4.2.2 Improvements to multi-material radiation hydrodynamics approach

A major limitation of our approach to computing radiation hydrodynamics with the diffusion assumption is the time-stepping restrictions imposed by the nonlinear diffusion term and the potentially stiff source term. Typically, these difficulties can be overcome by implicit time-stepping methods, which often offer stability properties that are independent of the time-step size [214]. However, this approach is at odds with our approach for multi-material flows (which necessarily includes a specially-designed limiting scheme), which would be quite difficult to adapt to implicit time-stepping. The issue of these contrasting requirements has been addressed by previous authors [79, 81, 191] by the use of implicit time-stepping for the diffusive and/or source terms, while the advective terms are treated explicitly. However, these implicit-explicit approaches are more difficult to apply to high-order methods. A promising solution is offered by diagonally-implicit Runge-Kutta time-stepping methods, which have been applied to DG [236] as well as to the radiation transport equation [237]. However, as of this writing, no author has applied these methods to the full radiation-hydrodynamics equations.

Another area for potential improvement in this work is in the model equations themselves. While we have proposed an extension to multigroup radiation diffusion, the assumption of radiation diffusion in general severely limits the types of problems that can be addressed. For example, radiation diffusion cannot follow shadows, a limitation that in some cases can result in net forces in the wrong direction [73]. While other methods for radiation transport, such as variable Eddington tensor [74], discrete ordinates [75] and Monte Carlo [76] methods, are more expensive, they may

be worthwhile in circumventing these issues.

The numerical method developed in this thesis offers several key advantages that are essential for direct numerical simulation of turbulent mixing in radiation hydrodynamics flows. Therefore, this scheme could be applied to study several interesting problems of importance to HED physics that may develop into turbulent flows, including the phenomenon of reshock in the Richtmeyer-Meshkov instability [168], the shock-driven Kelvin-Helmholtz instability [166], and even hydrodynamic instabilities in capsule implosions [28]. Any one of these problems could also be used as a framework for a systematic comparison to methods based on interface tracking, which may provide evidence supporting the further development of one of these approaches.

APPENDICES

APPENDIX A

Derivation of Radiation Hydrodynamics Equations

Here we derive the equations of radiation hydrodynamics as they are used throughout the present dissertation. We follow the derivations in [25, 191, 238].

A.1 Description of radiative transfer

In this derivation, we employ the particle description for electromagnetic radiation. While this description does not allow for a useful explanation of certain wave phenomena such as diffraction and dispersion, we are concerned chiefly with energy and momentum exchange between radiation and material particles. For these considerations, the particle description is most useful, and it is widely used in describing systems at densities typical of HED applications. The derivation detailed here is consistent among many sources in the literature [63, 91, 210, 239].

Photons carry energy and momentum with them, despite being massless. They may exert pressure upon surfaces, as well as exchange energy with other particles through a variety of mechanisms, such as photoabsorption and inelastic scattering. We assume that photons, between interactions with matter, travel at the speed of light c in the direction given by the unit vector $\mathbf{n}$. Each photon carries with it energy

$e = h\nu$, where h is Planck's constant and ν is the photon's frequency, as well as momentum $p = e/c$. However, we do not bother ourselves with a photon-by-photon description of radiative transport here, as this approach requires solution techniques that are very computationally expensive. In order to obtain a model that is tractable for computational solution, we rely instead upon distribution functions.

A.1.1 Specific intensity and radiative transfer equation

A distribution function often used to describe a radiation field is the specific intensity $I(\mathbf{x}, t; \mathbf{n}, \nu)$. It can be defined in terms of the energy crossing a differential element of surface d$\mathbf{s}$ into the solid angle element dω, in the frequency element dν, in time dt,

$$\delta E_s = I(\mathbf{x}, t; \mathbf{n}, \nu)\mathbf{n} \cdot \mathrm{d}\mathbf{s}\mathrm{d}\omega\mathrm{d}\nu\mathrm{d}t. \tag{A.1}$$

As such, this quantity has dimensions of energy per unit solid angle per unit time per unit area per unit frequency. We note that the differential element of solid angle, dω, can be written in terms of spherical coordinates as $\mathrm{d}\omega = \sin(\theta)\mathrm{d}\theta\mathrm{d}\phi$, where ϕ is the azimuthal spherical angle and θ is the polar angle. The integral over all solid angles is written here as $\oint_{4\pi} \mathrm{d}\omega = 4\pi$. The specific intensity is governed by the radiative transfer equation:

$$\frac{1}{c}\frac{\partial I}{\partial t} + \mathbf{n} \cdot \nabla I = \eta - \chi I. \tag{A.2}$$

in which the right-hand side describes interaction with matter through thermal absorption, thermal emission, and scattering. This equation can also be derived from quantum electrodynamics [240]. The emissivity $\eta(\mathbf{x}, t; \mathbf{n}, \nu)$ represents the addition of radiative energy to the radiation field due to the scattering and thermal emission of photons. The extinction coefficient, $\chi(\mathbf{x}, t; \mathbf{n}, \nu)$ governs the removal of radiative energy from the radiation field from scattering and thermal absorption of photons.

A.1.2 Moments of the radiative transfer equation

We define moments of the specific intensity with respect to the photon propagation direction $\mathbf{n}$. The zeroth moment is the spectral radiation energy density,

$$E_\nu(\mathbf{x}, t; \nu) = \frac{1}{c} \oint_{4\pi} I(\mathbf{x}, t; \mathbf{n}, \nu) \mathrm{d}\omega. \tag{A.3}$$

The first moment is the spectral radiation flux,

$$\mathbf{F}_\nu(\mathbf{x}, t; \nu) = \oint_{4\pi} I(\mathbf{x}, t; \mathbf{n}, \nu) \mathbf{n} \mathrm{d}\omega, \tag{A.4}$$

and the second moment is the spectral radiation pressure tensor,

$$\underline{\underline{\mathbf{P}_\nu}}(\mathbf{x}, t; \nu) = \frac{1}{c} \oint_{4\pi} I(\mathbf{x}, t; \mathbf{n}, \nu) \mathbf{n}\mathbf{n} \mathrm{d}\omega. \tag{A.5}$$

We use the subscript ν to indicate that a quantity has spectral dependence. Such dependence can be removed by integration over frequency, as in calculating the radiation energy density, $E_R(\mathbf{x}, t) = \int_0^\infty E_\nu(\mathbf{x}, t; \nu) \mathrm{d}\nu$. Taking the zeroth moment of Equation (A.2), we obtain an equation governing the spectral radiation energy density,

$$\frac{\partial E_\nu}{\partial t} + \nabla \cdot \mathbf{F}_\nu = \oint_{4\pi} (\eta - \chi I) \mathrm{d}\omega. \tag{A.6}$$

Integrating over frequency, we obtain a statement of energy balance for the radiation field,

$$\frac{\partial E_R}{\partial t} + \nabla \cdot \mathbf{F}_R = \int_0^\infty \oint_{4\pi} (\eta - \chi I) \mathrm{d}\omega \mathrm{d}\nu, \tag{A.7}$$

where the two terms in the integral on the right-hand side account for addition and removal of radiation energy, respectively, via interaction with matter. We denote the

energy source term, the right-hand side of Equation (A.7), as

$$S_E = \int_0^\infty \oint_{4\pi} \left[\eta(\mathbf{x}, t; \mathbf{n}, \nu) - \chi(\mathbf{x}, t; \mathbf{n}, \nu) I(\mathbf{x}, t; \mathbf{n}, \nu)\right] \mathrm{d}\omega \mathrm{d}\nu. \tag{A.8}$$

Taking the first moment of Equation (A.2), we obtain

$$\frac{1}{c^2}\frac{\partial \mathbf{F}_\nu}{\partial t} + \nabla \cdot \underline{\underline{\mathbf{P}_\nu}} = \frac{1}{c} \oint_{4\pi} (\eta - \chi I)\mathbf{n} \mathrm{d}\omega. \tag{A.9}$$

Integrating over frequency, we obtain a law governing the flux of the radiation field,

$$\frac{1}{c^2}\frac{\partial \mathbf{F}_R}{\partial t} + \nabla \cdot \underline{\underline{\mathbf{P}_R}} = \frac{1}{c} \int_0^\infty \oint_{4\pi} (\eta - \chi I)\mathbf{n} \mathrm{d}\omega \mathrm{d}\nu. \tag{A.10}$$

We denote the flux source term, the right-hand side of Equation (A.10), as

$$\mathbf{S}_F = \int_0^\infty \oint_{4\pi} \left[\eta(\mathbf{x}, t; \mathbf{n}, \nu) - \chi(\mathbf{x}, t; \mathbf{n}, \nu) I(\mathbf{x}, t; \mathbf{n}, \nu)\right] \mathbf{n} \mathrm{d}\omega \mathrm{d}\nu. \tag{A.11}$$

We see from the system formed by Equations (A.7) and (A.10) that in taking successive moments of the radiative transfer equation, we continue to introduce still higher moment quantities of the specific intensity, so in general we cannot obtain a closed system of equations using this process alone. This closure problem will be discussed further in Section A.4.1.

A.2 Radiation-material interaction terms

The source terms given by Equations (A.8) and (A.11) encode interaction between the radiation field and intervening material. In general, these terms include effects from thermal absorption and emission as well as scattering. Thermal processes couple radiation quantities to the local state of the material, as the absorption/emission of

photons causes transitions in electron energy states. In contrast, scattering is generally non-local as scattered photons can travel through many mean free paths. This non-locality presents a great difficulty for computation. Scattering is an important effect in diffuse gases, and as the density of the intervening material increases, the absorption opacity becomes far larger than the scattering opacity for the photon frequencies that contain a majority of the energy in typical HED sources (less than 5 keV). Therefore, in the dense systems of interest in HED sciences scattering can generally be neglected. Additionally, when measured at the laboratory-frame frequency ν, these terms are complicated by the effects of aberration and Doppler shift. For the purpose of yielding tractable models for radiation hydrodynamics, in this section we address both of these issues to simplify the evaluation of these material-interaction terms.

A.2.1 Thermal absorption and emission

In general, the extinction coefficient $\chi(\mathbf{x}, t; \mathbf{n}, \nu)$ is calculated by the sum $\chi = \sum_i n_i \sigma_i$, where n_i is the number density of particles of type i which absorb or scatter photons of frequency ν with a cross-section $\sigma_i(\nu)$. Neglecting scattering, we replace the extinction coefficient with the thermal absorption coefficient $\kappa^a_\nu(\mathbf{x}, t; \mathbf{n}, \nu)$. The thermal absorption coefficient is a material parameter that can be evaluated from atomic kinetics, given the state of the material. A quantity used in dimensional analysis of radiation hydrodynamics systems is the mean free path $\lambda_\nu = 1/\kappa^a_\nu$. This quantity scales with the mean distance a photon travels before being absorbed by intervening material.

Additionally, we replace the emissivity with the thermal emissivity $\eta^t_\nu(x_i, t; n_j, \nu)$. If the system is in strict thermodynamic equilibrium, in which the material emits and absorbs radiation as a blackbody, the Kirchhoff-Planck relation allows us to write the

thermal emissivity in terms of the thermal absorption coefficient:

$$\eta_\nu^t = \kappa_\nu^a B_\nu(\nu, T). \tag{A.12}$$

Where B_ν is the spectral energy density of a blackbody, which depends upon the temperature of the material T,

$$B_\nu(\nu, T) = \frac{2h\nu^3}{c^2} \frac{1}{e^{\frac{h\nu}{k_B T}} - 1}. \tag{A.13}$$

Here, k_B is the Boltzmann constant. Integrating Equation (A.12) over frequency,

$$\eta^t = \kappa^a B(T) = \kappa^a \sigma_R T^4. \tag{A.14}$$

Where σ_R is the Stefan-Boltzmann constant, and κ^a is the mean thermal absorption coefficient. In general, we extend this relationship from strict thermodynamic equilibrium to local thermodynamic equilibrium (LTE), where gradients of material quantities (density, temperature, pressure) occur on length-scales much larger than the photon mean free path λ_ν. This is discussed in greater detail in Section A.4.1.

A.3 Co-moving equations

Due to the effects of relativistic aberration and Doppler shift, the frequency and directional dependence of the material interaction terms — and consequently the unknown radiation quantities $(E_R, \mathbf{F}_R, \underline{\underline{\mathbf{P}_R}})$ — are complicated when frequency is measured in the laboratory frame. These effects include a dependence of both frequency and direction upon the velocity of the background material $\mathbf{u}$. However, if the frequency is measured in the co-moving frame of the material, denoted as ν_0, the material interaction terms are isotropic. So, we transform Equations (A.7) and (A.10) to be evaluated at ν_0. In this section, we drop the arguments $\mathbf{x}, t$ from all

quantities for convenience.

We could proceed by applying the Lorentz transformation to all quantities, but it is conceptually simpler to consider Lorentz invariant quantities. We do not rigorously justify each of these steps, and direct the reader to Mihalas and Mihalas [25] for a more detailed treatment. One Lorentz invariant is the number of photons entering a volume $\mathrm{d}V$ into the solid angle $\mathrm{d}\omega$ and frequency interval $\mathrm{d}\nu$ in time $\mathrm{d}t$,

$$N = \frac{\eta(\mathbf{n}, \nu)\mathrm{d}\omega\mathrm{d}\nu\mathrm{d}V\mathrm{d}t}{h\nu}. \tag{A.15}$$

The quantity $\nu\mathrm{d}\nu\mathrm{d}\omega$ can be shown to be Lorentz invariant as well. Using these two invariants together, we obtain

$$\eta(\mathbf{n}, \nu) = \left(\frac{\nu}{\nu_0}\right)^2 \eta_0(\nu_0). \tag{A.16}$$

Where the emissivity in the co-moving frame, η_0, is isotropic. Similarly for the extinction coefficient, the number of photons disappearing is invariant,

$$N = \frac{\chi(\mathbf{n}, \nu)I(\mathbf{n}, \nu)\mathrm{d}\omega\mathrm{d}\nu\mathrm{d}V\mathrm{d}t}{h\nu}. \tag{A.17}$$

The quantity I/ν^3 is Lorentz invariant as well. This yields

$$\chi(\mathbf{n}, \nu) = \left(\frac{\nu_0}{\nu}\right)\chi_0(\nu_0). \tag{A.18}$$

We evaluate $\eta(\mathbf{n}, \nu)$ and $\chi(\mathbf{n}, \nu)$ at the Doppler-shifted co-moving frequency, correct to $\mathcal{O}(u/c)$:

$$\nu_0 = \nu\left(1 - \frac{\mathbf{n} \cdot \mathbf{u}}{c}\right). \tag{A.19}$$

Then, using Equations (A.16) and (A.18) and Taylor expanding in frequency up to

$\mathcal{O}(u/c)$, we can write,

$$\chi(\mathbf{n},\nu) = \chi_0(\nu) - \left(\frac{\mathbf{n}\cdot\mathbf{u}}{c}\right)\left[\chi_0(\nu) + \nu\frac{\partial\chi_0}{\partial\nu}\right], \tag{A.20a}$$

$$\eta(\mathbf{n},\nu) = \eta_0(\nu) + \left(\frac{\mathbf{n}\cdot\mathbf{u}}{c}\right)\left[2\eta_0(\nu) - \nu\frac{\partial\eta_0}{\partial\nu}\right]. \tag{A.20b}$$

Inserting these expansions into Equations (A.8) and (A.11), we have

$$S_E = \int_0^\infty \left[4\pi\eta_0(\nu) - c\chi_0(\nu)E_\nu\right]\mathrm{d}\nu + \frac{\mathbf{u}}{c}\cdot\int_0^\infty\left[\chi_0(\nu) + \nu\frac{\partial\chi_0}{\partial\nu}\right]\mathbf{F}_\nu\mathrm{d}\nu, \tag{A.21a}$$

$$\mathbf{S}_F = -\frac{1}{c}\int_0^\infty \chi_0(\nu)\mathbf{F}_\nu\mathrm{d}\nu + \frac{4\pi\mathbf{u}}{c^2}\int_0^\infty\eta_0(\nu)\mathrm{d}\nu + \frac{\mathbf{u}}{c}\cdot\int_0^\infty\left[\chi_0(\nu) + \nu\frac{\partial\chi_0}{\partial\nu}\right]\underline{\underline{\mathbf{P}_R}}\mathrm{d}\nu. \tag{A.21b}$$

We note that ν is still measured in the Eulerian frame, so these source terms are said to be in the mixed form. Using the definitions in Equations (A.3) - (A.5), along with the Lorentz invariance of I/ν^3 and Equation (A.19), and retaining only terms up to order $\mathcal{O}(u/c)$,

$$E_R = E_{R,0} + \frac{2}{c^2}\mathbf{u}\cdot\mathbf{F}_{\nu,0}, \tag{A.22a}$$

$$\mathbf{F}_R = \mathbf{F}_{R,0} + E_{R,0}\mathbf{u} + \mathbf{u}\cdot\underline{\underline{\mathbf{P}_{R,0}}}, \tag{A.22b}$$

$$\underline{\underline{\mathbf{P}_R}} = \underline{\underline{\mathbf{P}_{R,0}}} + \frac{1}{c^2}(\mathbf{u}\mathbf{F}_{R,0} + \mathbf{F}_{R,0}\mathbf{u}). \tag{A.22c}$$

Similarly, we transform the source terms up to $\mathcal{O}(u/c)$,

$$S_E = S_{E,0} + \mathbf{u}\cdot\mathbf{S}_{F,0}, \tag{A.23a}$$

$$\mathbf{S}_F = \mathbf{S}_{F,0} + \frac{\mathbf{u}}{c}S_{E,0}, \tag{A.23b}$$

where the source terms in the co-moving frame are

$$S_{E,0} = \int_0^\infty \left[4\pi\eta_0(\nu_0) - c\chi_0(\nu_0)E_{\nu,0}(\nu_0)\right] \mathrm{d}\nu_0, \tag{A.24a}$$

$$\mathbf{S}_{F,0} = -\frac{1}{c}\int_0^\infty \chi_0(\nu_0)\mathbf{F}_{\nu,0}(\nu_0)\mathrm{d}\nu_0. \tag{A.24b}$$

Inserting these into Equations (A.7) and (A.10), we have

$$\frac{\partial}{\partial t}\left[E_{R,0} + \frac{2}{c^2}\mathbf{u}\cdot\mathbf{F}_{\nu,0}\right] + \nabla\cdot\left[\mathbf{F}_{R,0} + E_{R,0}\mathbf{u} + \mathbf{u}\cdot\underline{\underline{\mathbf{P}_{R,0}}}\right] = S_{E,0} + \mathbf{u}\cdot\mathbf{S}_{F,0}, \tag{A.25a}$$

$$\frac{1}{c^2}\frac{\partial}{\partial t}\left[\mathbf{F}_{R,0} + E_{R,0}\mathbf{u} + \mathbf{u}\cdot\underline{\underline{\mathbf{P}_{R,0}}}\right] + \nabla\cdot\left[\underline{\underline{\mathbf{P}_{R,0}}} + \frac{1}{c^2}(\mathbf{u}\mathbf{F}_{R,0} + \mathbf{F}_{R,0}\mathbf{u})\right] = \mathbf{S}_{F,0} + \frac{\mathbf{u}}{c}S_{E,0}. \tag{A.25b}$$

Retaining leading-order terms in the limit $u/c \ll 1$, Equations (A.25) become

$$\frac{\partial E_{R,0}}{\partial t} + \nabla\cdot\left[\mathbf{F}_{R,0} + E_{R,0}\mathbf{u} + \mathbf{u}\cdot\underline{\underline{\mathbf{P}_{R,0}}}\right] = S_{E,0} + \mathbf{u}\cdot\mathbf{S}_{F,0}, \tag{A.26a}$$

$$\nabla\cdot\underline{\underline{\mathbf{P}_{R,0}}} = \mathbf{S}_{F,0}. \tag{A.26b}$$

A.4 Radiation hydrodynamics equations

For a radiation hydrodynamics system that is not in strict thermal equilibrium, the total material energy density E and the radiation energy density E_R are both unknowns. So, in general, we solve two energy equations: one for the energy of the material and one for the energy of the radiation field. These energy equations are coupled together by the radiation-material interaction terms, and we must ensure that energy transferred to/from the radiation field via these terms is conserved. Thus, we modify the compressible Euler equations by the addition of the co-moving momentum

and energy source leading terms:

$$\frac{\partial}{\partial t}\rho\mathbf{u} + \nabla\cdot\left[\rho\mathbf{u}\mathbf{u} + p\underline{\underline{\mathbf{I}}}\right] = -\mathbf{S}_{F,0}, \tag{A.27a}$$

$$\frac{\partial}{\partial t}E + \nabla\cdot\mathbf{u}(E+p) = -S_{E,0} - \mathbf{u}\cdot\mathbf{S}_{F,0}. \tag{A.27b}$$

We augment this system with Equation (A.26a), and simplify by inserting Equation (A.26b):

$$\frac{\partial}{\partial t}\rho + \nabla\cdot\rho\mathbf{u} = 0, \tag{A.28a}$$

$$\frac{\partial}{\partial t}\rho\mathbf{u} + \nabla\cdot\left[\rho\mathbf{u}\mathbf{u} + p\underline{\underline{\mathbf{I}}} + \underline{\underline{\mathbf{P}_{R,0}}}\right] = 0, \tag{A.28b}$$

$$\frac{\partial}{\partial t}E + \nabla\cdot\mathbf{u}(E+p) + \mathbf{u}\cdot\nabla\cdot\underline{\underline{\mathbf{P}_{R,0}}} = -S_{E,0}, \tag{A.28c}$$

$$\frac{\partial}{\partial t}E_{R,0} + \nabla\cdot\left[\mathbf{F}_{R,0} + E_{R,0}\mathbf{u} + \mathbf{u}\cdot\underline{\underline{\mathbf{P}_{R,0}}}\right] - \mathbf{u}\cdot\nabla\cdot\underline{\underline{\mathbf{P}_{R,0}}} = S_{E,0}. \tag{A.28d}$$

These are the basic equations behind our study of radiation hydrodynamics. So far, we have made the assumption that the system is non-relativistic, i.e. $u/c \ll 1$. We have also assumed a form of $S_{E,0}$ that neglects the effect of scattering. Keeping in mind that all radiation equations are evaluated at the co-moving frequency ν_0, we drop the 0 subscript from this point onward.

A.4.1 The diffusion assumption

In a gas at standard conditions, we can always specify the closure relation between the pressure p and internal energy e because the particle mean free path is much smaller than the characteristic length-scale of the system. In general, radiative transfer does not share this attribute with gas dynamics. Only in dense systems far from boundaries, where the photon mean free path λ_ν is much smaller than the characteristic length scale can we impose an analytical closure relationship. Similar to the process followed in fluid mechanics, we seek to relate the tensor $\underline{\underline{\mathbf{P}_\nu}}$ to E_ν. We

can define a mean radiation pressure: $\bar{P}_\nu = \text{trace}(\underline{\underline{\mathbf{P}_\nu}}) = \frac{1}{3}E_\nu$, where the last equality can be shown simply because $\mathbf{n}$ is a unit vector. Furthermore, assuming the photon distribution function is isotropic, ie. $\underline{\underline{\mathbf{P}_\nu}} = p_\nu \underline{\underline{\mathbf{I}}}$, we obtain $p_\nu = \frac{1}{3}E_\nu$.

Another consequence of this assumption is in determining the form of $\mathbf{F}_R$. Equation (A.26b) states:

$$\nabla \cdot \underline{\underline{\mathbf{P}_R}} = -\frac{1}{c}\int_0^\infty \chi(\nu)\mathbf{F}_\nu(\nu)\mathrm{d}\nu \tag{A.29}$$

As we have assumed the radiation field is isotropic, we can write:

$$\frac{1}{3}\nabla E_R = -\frac{1}{c}\int_0^\infty \chi(\nu)\mathbf{F}_\nu(\nu)\mathrm{d}\nu \tag{A.30}$$

Integrating the right-hand side and replacing the extinction coefficient with a mean value $\bar{\chi}(\nu)$,

$$\mathbf{F}_R = -\frac{c}{3\bar{\chi}}\nabla E_R \tag{A.31}$$

Following the assumption of isotropy, radiation transport follows a diffusive flux law similar to Fourier heat conduction in a fluid. One key difference is that, in general, $\bar{\chi}$ depends on the state of the material, so in general radiation diffusion is non-linear with a variable diffusion coefficient.

We may assess the validity of the diffusion coefficient by considering relative time-scales between motion of the fluid and the diffusion of photons. Defining a characteristic system length L and fluid speed u, we write the time scale of hydrodynamic motion as $\tau_f = L/u$. We write the time-scale of diffusion as $\tau_d = L^2/D_R$, where D_R is the diffusion coefficient. Noting from the above result that $D_R \sim c\lambda_\nu$, we define the time scale related to radiation diffusion as,

$$\tau_d = \frac{L^2}{c\lambda_\nu}. \tag{A.32}$$

The diffusion assumption is valid in the case that hydrodynamic motion transports energy much slower than radiation diffusion, ($\tau_f \gg \tau_d$). This is the equilibrium diffusion regime, where the radiation field equilibrates to the fluid conditions faster than the fluid can propagate disturbances. Thus, the radiation field is always a quantity that is known, that instantaneously equilibrates with the fluid. The more generally applicable regime is that of non-equilibrium diffusion, where the flow transports energy faster than radiation diffusion ($\tau_f \leq \tau_d$). The non-equilibrium diffusion regime occurs when the fluid is sufficiently opaque to trap and advect radiation energy along with it, while the diffusion process transports radiative energy too slowly to redistribute the radiation energy into equilibrium. We consider these regimes when describing models of radiative hydrodynamics systems.

An assumption that is often made alongside the diffusion assumption is that of LTE, which assumes that spatial gradients in the material are much larger than the photon mean free path. These two assumptions are not necessarily equivalent, but both tend to apply in sufficiently dense systems. This condition is required for the energies of the material and radiation field to be simultaneously defined at a point $(\mathbf{x}, t)$ in such a way that they tend to equilibrate. This equilibration occurs through radiation diffusion, as well as through the energy source term that accounts for emission and absorption in Equation (A.24a). This is in contrast to the assumption of strict thermodynamic equilibrium, in which the radiation field is a blackbody and is given by the Planck function, Equation (A.13). The assumption of LTE and of isotropy (and radiation diffusion) are often applied together, as they yield a tractable mathematical description and both are valid for sufficiently dense systems far from boundaries.

A.4.2 Multigroup non-equilibrium diffusion

Here we describe the most general model for radiation hydrodynamics discussed here, using a multigroup approach to discretize the radiation quantities with respect to the frequency variable. Though the analysis in Section A.3 was applied to frequency-integrated quantities, we can apply it similarly to the quantities integrated over frequency groups. We break the frequency spectrum into G number of radiation groups where frequency-dependent quantities are assumed piecewise constant in each group. The g-th group spans the frequencies $\nu \in [\nu_g, \nu_{g+1}]$. The g-th radiation energy density is defined $E_g = \int_{\nu_g}^{\nu_{g+1}} E_\nu \mathrm{d}\nu$. Applying the LTE assumption to each group, we evaluate the source term in Equation (A.24a) using Equation (A.14) to obtain:

$$S_{E,g} = c \int_{\nu_g}^{\nu_{g+1}} \kappa_\nu^a \left[\frac{4\pi}{c} B_\nu(\nu, T) - E_\nu \right] \mathrm{d}\nu = c\kappa_{P,g} \left[B_g - E_g \right], \tag{A.33}$$

where the group-wise blackbody energy density is:

$$B_g(T) = \int_{\nu_g}^{\nu_{g+1}} \frac{4\pi}{c} B_\nu(\nu, T) \mathrm{d}\nu, \tag{A.34}$$

and the Planck mean opacity for group g is defined as:

$$\kappa_{P,g} = \frac{\int_{\nu_g}^{\nu_{g+1}} \kappa_\nu^a(\nu) B_\nu(\nu, T) \mathrm{d}\nu}{B_g(T)}. \tag{A.35}$$

Applying the diffusion assumption result in Equation (A.31), integrated over each group rather than the entire spectrum, we obtain,

$$\mathbf{F}_{R,g} = -\frac{c}{3\kappa_{R,g}} \nabla E_g, \tag{A.36}$$

where the Rosseland mean opacity for group g is defined by:

$$\kappa_{R,g} = \frac{\frac{\partial B_g(T)}{\partial T}}{\int_{\nu_g}^{\nu_{g+1}} \frac{1}{\kappa_\nu^a(\nu)} \frac{\partial B_\nu(\nu,T)}{\partial T} \mathrm{d}\nu}. \tag{A.37}$$

We also have the assumption of isotropy for each group,

$$\underline{\underline{\mathbf{P}_g}} = p_g \underline{\underline{\mathbf{I}}} = \frac{1}{3} E_g \underline{\underline{\mathbf{I}}}. \tag{A.38}$$

Thus, evaluating (A.28d) group-wise results in G number of radiation energy equations:

$$\frac{\partial}{\partial t} E_g + \nabla \cdot [\mathbf{u}(E_g + p_g)] - \frac{1}{3}(\nabla \cdot \mathbf{u}) \left[\int_{\nu_g}^{\nu_{g+1}} \frac{\partial}{\partial \nu} \nu E_\nu \mathrm{d}\nu \right] - \mathbf{u} \cdot \nabla p_g = \nabla \cdot \frac{c}{3\kappa_{R,g}} \nabla E_g + c\kappa_{P,g} \left[B_g - E_g \right]. \tag{A.39}$$

And the material energy equation:

$$\frac{\partial}{\partial t} E + \nabla \cdot [\mathbf{u}(E + p)] + \mathbf{u} \cdot \nabla p_R = -\sum_g c\kappa_{P,g} \left[B_g - E_g \right], \tag{A.40}$$

where $E_R = \sum_g E_g$ and $p_R = \frac{1}{3} E_R$.

In practice, for each group g the Rosseland and Planck mean opacities are assumed to be constant. In general, these quantities, along with the thermal absorption coefficient κ_ν^a, may depend on material properties such as mass density and temperature. We also solve the conservation of mass and momentum equations for the fluid:

$$\frac{\partial}{\partial t} \rho + \nabla \cdot \rho \mathbf{u} = 0, \tag{A.41a}$$

$$\frac{\partial}{\partial t} \rho \mathbf{u} + \nabla \cdot \left[\rho \mathbf{u}\mathbf{u} + (p + p_R) \underline{\underline{\mathbf{I}}} \right] = 0, \tag{A.41b}$$

$$\tag{A.41c}$$

This is the most detailed model for radiation hydrodynamics that will be discussed

in this thesis, as it addresses the frequency dependence of the unknown radiation quantities.

A.4.3 Gray non-equilibrium diffusion

Now, we assume that radiation is "gray", or monoenergetic. This assumption is often applied when the radiation energy is concentrated in a portion of the spectrum over which the optical properties of the material don't vary significantly. Effectively, we ignore spectral variation of the radiation and material-interaction quantities, and solve for the total radiation energy density, $E_R = \sum_g E_g$. As in the multigroup case, we employ the diffusion and LTE assumptions, integrating over the entire spectrum, so that Equations (A.14), (A.36) and (A.38) result in:

$$\frac{\partial}{\partial t}\rho + \nabla \cdot \rho\mathbf{u} = 0, \quad \text{(A.42a)}$$

$$\frac{\partial}{\partial t}\rho\mathbf{u} + \nabla \cdot \left[\rho\mathbf{u}\mathbf{u} + (p + p_R)\underline{\underline{\mathbf{I}}}\right] = 0, \quad \text{(A.42b)}$$

$$\frac{\partial}{\partial t}E + \nabla \cdot [\mathbf{u}(E + p)] + \mathbf{u} \cdot \nabla p_R = -c\kappa_P \left[a_R T^4 - E_R\right], \quad \text{(A.42c)}$$

$$\frac{\partial}{\partial t}E_R + \nabla \cdot [\mathbf{u}(E_R + p_R)] - \mathbf{u} \cdot \nabla p_R = \nabla \cdot \frac{c}{3\kappa_R}\nabla E_R + c\kappa_P \left[a_R T^4 - E_R\right]. \quad \text{(A.42d)}$$

Note the presence of non-conservative terms as well as source terms in each energy equation.

A.4.4 Gray equilibrium diffusion

Now, we insist that the radiation field and material are in strict thermodynamic equilibrium. The source term in Equation (A.24a) becomes, making use of Equation (A.14):

$$S_E = 4\pi\kappa B(T) - c\kappa E_R. \quad \text{(A.43)}$$

If we assume also that the radiation and the material are in strict thermodynamic equilibrium with one another, S_E must be zero and the radiation energy density E_R is not an unknown and can be specified with the temperature alone:

$$E_R = \frac{4\sigma_B}{c} T^4 = a_R T^4. \tag{A.44}$$

As solving an equation for the radiation energy density would amount to solving more equations that unknowns, we solve the system (A.28) with a single energy equation comprised of the sum of (A.28c) and (A.26a):

$$\frac{\partial}{\partial t}\rho + \nabla \cdot \rho\mathbf{u} = 0, \tag{A.45a}$$

$$\frac{\partial}{\partial t}\rho\mathbf{u} + \nabla \cdot \left[\rho\mathbf{u}\mathbf{u} + (p + p_R)\underline{\underline{\mathbf{I}}}\right] = 0, \tag{A.45b}$$

$$\frac{\partial}{\partial t}(E + E_R) + \nabla \cdot [\mathbf{u}(E + E_R + p + p_R)] = \nabla \cdot \frac{c}{3\kappa_R}\nabla E_R. \tag{A.45c}$$

APPENDIX B

Derivation of Analytical Impulse Models

This appendix details the derivation of the analytical impulse models utilized in this dissertation. We follow the derivations in Reaugh et al. [119], the results of which agree with other sources [120, 135]. In each case, we assume that energetic particles deposit a specific energy profile $E(m)$, in an initially uniform 1-D slab of material. Each model involves the final specific energy distribution $E_f(m)$, which cannot be known a-priori, and instead must be modeled or obtained using data.

B.1 Whitener model

The Whitener model [135] is derived by assuming that, for each differential element of material, the energy lost during the blow-off process is entirely converted into kinetic energy:

$$E(m) - E_f(m) = \Delta E(m) = \frac{1}{2}u^2, \tag{B.1}$$

where u is the material velocity. We note that this assumption implies that each differential layer of the material is unimpeded by other layers from expanding from the bulk material. Using the definition of the impulse, $I = \int_0^{m_B} u \mathrm{d}m$, we obtain the

expression

$$I = \sqrt{2} \int_0^{m_B} \left[E(m) - E_f(m)\right]^{1/2} \mathrm{d}m. \tag{B.2}$$

Here, m_B is the blow-off interface Lagrangian coordinate, equal to the amount of mass blown off of the slab. This model tends to significantly overestimate impulse, and does not take into account the interaction of successive layers of material, which exert pressure upon one another.

B.2 BBAY model

Unlike the Whitener model, the Bethe, Bade, Averell, and Yos (BBAY) model is a closed-form solution of the equations of motion. We write the radiation hydrodynamics equations for a single fluid in 1-D Lagrangian coordinates to describe the blow-off material:

$$\frac{\partial x}{\partial m} = \nu \tag{B.3a}$$

$$\frac{Du}{Dt} + \frac{\partial p}{\partial m} = 0 \tag{B.3b}$$

$$\frac{De}{Dt} + p\frac{D\nu}{Dt} = s_R \tag{B.3c}$$

where x is the Eulerian coordinate, $\nu = 1/\rho$ is the specific volume, e is the material specific internal energy, p is the pressure, and $s_R(m,t)$ is the source term due to absorption per unit mass. Here we use the Lagrangian material derivative:

$$\frac{D}{Dt} = \frac{\partial}{\partial t} + \frac{\mathrm{d}x}{\mathrm{d}t}\frac{\partial}{\partial x} \tag{B.4}$$

where we note that

$$\frac{\mathrm{d}x}{\mathrm{d}t} = u \tag{B.5}$$

The form of (B.3) neglects terms present in other treatments of radiation hydrodynamics, such as those presented in Appendix A. We also do not solve an energy equation for the radiation field. This modeling approach is justified because in this analysis, we assume that the duration over which radiation is heating the material, the drive time τ_D, is small compared to the time scales associated with the hydrodynamic motion. Additionally, we assume that the heated material does not heat to sufficiently high temperatures to emit substantial radiation itself. Therefore, there is no two-way coupling between the fluid and radiation field, so we use equations that govern the motion of the blow-off fluid, with a source term added to (B.3c) to represent heating from radiation. This source term is nonzero during the drive time only. To obtain an analytical solution to (B.3), we assume that the energy deposition occurs at a constant rate over the drive time τ_D,

$$s_R(m,t) = \begin{cases} \left(\frac{1}{\tau_D}\right)\max\left\{\ E(m) - E_f(m),\ 0\ \right\}, & 0 \le t \le \tau_D, \\ 0, & \tau_D < t. \end{cases} \tag{B.6}$$

We note that, as stated previously, τ_D is (assumed) small over the hydrodynamic times of interest. In fact, the current analysis seeks to find a closed-form solution to (B.3) for times $t > \tau_D$. Here $E(m)$ is the profile of energy per unit mass deposited within the material. We formally define the blow-off interface coordinate m_B as:

$$E(m_B) = E_f(m_B). \tag{B.7}$$

We define a new dependent variable Z as:

$$Z = \int_0^m x(\tilde{m},t)\mathrm{d}\tilde{m}. \tag{B.8}$$

In terms of this new variable, we rewrite (B.3) and (B.5) as:

$$x = Z', \tag{B.9a}$$

$$\nu = Z'', \tag{B.9b}$$

$$u = \dot{Z}', \tag{B.9c}$$

$$P = -\ddot{Z}, \tag{B.9d}$$

$$\dot{e} = s_R + \ddot{Z}\dot{Z}''. \tag{B.9e}$$

Here we denote partial derivatives with respect to the Lagrangian variable m by Z', and the total derivative D/Dt by $\dot{Z}$. We assume that the blow-off material obeys the ideal gas law,

$$e = p\nu/(\gamma - 1). \tag{B.10}$$

Substituting this equation of state, (B.9e) becomes:

$$\dddot{Z}Z'' + \gamma\ddot{Z}\dot{Z}'' = (1-\gamma)s_R. \tag{B.11}$$

We assume that Z is separable,

$$Z(m,t) = z_m(m)z_t(t), \tag{B.12}$$

which yields, after inserting into (B.11),

$$\left[\dddot{z}_t z_t + \gamma\ddot{z}_t\dot{z}_t\right] z_m z_m'' = (1-\gamma)s_R. \tag{B.13}$$

Since s_R is a function of m only, we can write separate equations that depend on t and m,

$$\dddot{z}_t z_t + \gamma \ddot{z}_t \dot{z}_t = \begin{cases} c_1, & 0 \le t \le \tau_D, \\ 0, & \tau_D \le t, \end{cases} \tag{B.14a}$$

$$z_m z_m'' = (1-\gamma)\frac{s_R}{c_1} = \frac{(1-\gamma)}{c_1 \tau_D} \max\{\ E(m) - E_f(m),\ 0\ \}, \tag{B.14b}$$

where c_1 is a constant of integration. Inserting the general solution $z_t = t^n$ into (B.14a), valid for the interval $0 \le t \le \tau_D$, we find that $n = \frac{3}{2}$ and $c_1 = \frac{3}{8}(3\gamma - 1)$. For $\tau_D \le t$, we can write (B.14a) as,

$$z_t^{(1-\gamma)} \frac{\mathrm{d}}{\mathrm{d}t}\left[z_t^{\gamma} \ddot{z}_t\right] = 0, \tag{B.15}$$

which implies,

$$z_t^{\gamma} \ddot{z}_t = c_2, \tag{B.16}$$

where c_2 is a constant. We integrate (B.16) and enforce continuity at $t = \tau_D$ with the conditions $z_t(\tau_D) = \tau_D^{3/2}$ and $\dot{z}_t(\tau_D) = \frac{3}{2}\tau_D^{1/2}$ to obtain

$$\dot{z}_t = \left[\frac{3\tau_D}{2\beta} - \frac{3\tau_D^{(3\gamma-1)/2}}{2(\gamma-1)} z_t^{(1-\gamma)}\right]^{1/2}, \tag{B.17}$$

where $\beta = \left[\frac{3}{2} + \frac{1}{\gamma - 1}\right]^{-1} = \frac{3(\gamma-1)}{4c_1}$. The equation (B.14b) becomes:

$$z_m z_m'' = -\frac{4}{3}\frac{\beta}{\tau_D} \max\{\ E(m) - E_f(m), \quad 0\ \}, \tag{B.18}$$

valid in the region $0 \leq m \leq m_B$. We enforce boundary conditions by requiring that the left boundary is a free surface, and the blow-off interface is fixed

$$p(0,t) = -z_m(0)\ddot{z}_t = 0, \tag{B.19a}$$

$$u(m_B,t) = z'_m(m_B)\dot{z}_t = 0. \tag{B.19b}$$

Here we evaluate the impulse as:

$$I = \int_0^\infty p(m_B,t)\mathrm{d}t = \left[\dot{z}_t(0) - \dot{z}_t(\infty)\right] z_m(m_B). \tag{B.20}$$

Because $z_m(m)\dot{z}_t(0) = \dot{Z}(m,0) = \int_0^m u(\tilde{m},0)\mathrm{d}\tilde{m}$ and the initial velocity is zero, $u(m,0) = 0$, we obtain that $\dot{z}_t(0) = 0$. From (B.17), we obtain,

$$\dot{z}_t(\infty) = \sqrt{\frac{3\tau_D}{2\beta}}, \tag{B.21}$$

which yields

$$I = -\sqrt{\frac{3\tau_D}{2\beta}} z_m(m_B). \tag{B.22}$$

We further define the function:

$$F(m) = \frac{4}{3}\frac{\beta}{\tau_D}\max\left\{\ E(m) - E_f(m), \quad 0\ \right\}. \tag{B.23}$$

Rearranging (B.18), integrating, and employing the boundary condition $z'_m(m_B) = 0$ we obtain:

$$z'_m(m) = -\int_{m_B}^m \frac{F(\tilde{m})}{z_m(\tilde{m})}\mathrm{d}\tilde{m}. \tag{B.24}$$

Integrating once more, and employing the boundary condition $z_m(0) = 0$ gives,

$$z_m(m) = \int_0^m \left[\int_{m^*}^{m_B} \frac{F(\tilde{m})}{z_m(\tilde{m})} \mathrm{d}\tilde{m} \right] \mathrm{d}m^*. \tag{B.25}$$

Exchanging the order of integration, we have

$$z_m(m_B) = \int_0^{m_B} \frac{\tilde{m} F(\tilde{m})}{z_m(\tilde{m})} \mathrm{d}\tilde{m}. \tag{B.26}$$

One could solve (B.30) numerically, but the original BBAY derivation makes an approximation. We assume that the average of z_m over the interval $0 \leq m \leq m_B$ is $z_m(m_B)/\alpha^2$, where α is a constant to be determined. Replacing z_m within the integrand with this average value yields

$$[z_m(m_B)]^2 = \alpha^2 \int_0^{m_B} \tilde{m} F(\tilde{m}) \mathrm{d}\tilde{m}. \tag{B.27}$$

Inserting this expression into (B.22) yields,

$$I = \alpha \Big[2 \int_0^{m_B} m \left[E(m) - E_f(m) \right] \mathrm{d}m \Big]^{1/2}. \tag{B.28}$$

Thus we obtain the BBAY model as utilized throughout this work. We note that one can confirm that the expression stands to reason by the following consideration. If we consider a mass m within the blow-off from the slab, being pushed by the energy contained in an incremental mass Δm behind it, the final kinetic energy will be $\frac{1}{2} m u^2 = (E - E_f)\Delta m$. Thus, the square of the momentum at a point m is

$$(mu)^2 = 2m(E - E_f)\Delta m. \tag{B.29}$$

Integrating over the blow-off region $0 \leq m \leq m_B$, we obtain the expression

$$I = \alpha \Big[2 \int_0^{m_B} m \left[E(m) - E_f(m) \right] \mathrm{d}m \Big]^{1/2}. \tag{B.30}$$

Which, with the exception of the constant α, is the same expression obtained in this derivation.

APPENDIX C

Extending DG Approach to Multigroup Radiation Hydrodynamics

This appendix describes the extension of our method to the multigroup radiation diffusion equations. The form of System (3.1) assumes that the transport of radiation energy can be adequately described by a single radiation energy density, and its interaction with the material can be described using a single opacity. However, there are problems in which the unknown radiation quantities depend strongly on frequency. Multigroup treatment is necessary in cases where the spectrally dependent radiation energy density E_ν deviates significantly from Planckian. We derived the multigroup equations in Appendix A. Rather than solving the single transport equation (3.1d), one solves G equations, each governing the transport of radiation in the g-th frequency group $\nu \in [\nu_{g-1/2}, \nu_{g+1/2}]$:

$$\frac{\partial}{\partial t}E_g+\frac{\partial}{\partial x_j}u_j(E_g+p_g)-u_j\frac{\partial}{\partial x_j}p_g-\frac{1}{3}\frac{\partial u_j}{\partial x_j}\int_{\nu_{g-1/2}}^{\nu_{g+1/2}}\frac{\partial(\nu E_\nu)}{\partial \nu}\mathrm{d}\nu-\frac{\partial}{\partial x_j}D_g\frac{\partial}{\partial x_j}E_g=S_g. \quad \text{(C.1)}$$

Here $p_g = \frac{1}{3}E_g$. Note that $E_R = \int_0^\infty E_\nu \mathrm{d}\nu$, and $E_g = \int_{\nu_{g-1/2}}^{\nu_{g+1/2}} E_\nu \mathrm{d}\nu$. The group-wise

radiation diffusion coefficient is

$$D_g = \frac{c}{3\kappa_{R,g}}. \tag{C.2}$$

And the group-wise source term is

$$S_g = c\kappa_{P,g}(B_g - E_g). \tag{C.3}$$

Now, the source term in the material energy equation 3.1c will be replaced by

$$S_R = \sum_g c\kappa_{P,g}(B_g - E_g). \tag{C.4}$$

Comparison with (3.1d) reveals that the only term in (C.1) that needs additional numerical treatment is the integral term. We follow the approach of Ref. [79] and consider logarithmically spaced frequency bins, i.e., $\ln \nu_{g+1/2} - \ln \nu_{g-1/2} = \Delta(\ln \nu)$ is constant for all groups. Then, we have

$$E_g = \int_{\nu_{g-1/2}}^{\nu_{g+1/2}} E_\nu \mathrm{d}\nu = \int_{\ln \nu_{g-1/2}}^{\ln \nu_{g+1/2}} \nu E_\nu \mathrm{d}(\ln \nu) \approx \nu E_\nu \Delta(\ln \nu). \tag{C.5}$$

This approximation allows us to approximate the integral in (C.1) as,

$$\int_{\nu_{g-1/2}}^{\nu_{g+1/2}} \frac{\partial(\nu E_\nu)}{\partial \nu} \mathrm{d}\nu \approx \frac{E_{g+1/2} - E_{g-1/2}}{\Delta(\ln \nu)}. \tag{C.6}$$

We interpolate using adjacent E_g values for the values at $g \pm 1/2$. Once we have made this simplification, we treat the integral term in Equation (C.1) as a non-conservative advection term, and discretize it as described in Section 3.5.1.

APPENDIX D

Properties of DG Discretization Operators and HR Limiting Procedure

D.1 Properties of the DG weak form

In this appendix, we verify properties of the DG discretization operators that we use in our analysis of pressure and temperature errors in Section 3.6.1. In the following, X and Y are variables and a is a constant. Without loss of generality, we assume an upwind flux, $\mathbf{f}^*|_{x_{e-1/2}} = \mathbf{f}^{e-1}|_{x_{e-1/2}}$. We rely on the following properties governing the discretization operator for the conservative advective flux:

$$
\begin{aligned}
D^j_{f,e}(aX+Y) &= (M^{-1})^{jk}_e R^k_{f,e}(aX+Y) \\
&= (M^{-1})^{jk}_e \Bigg\{ \left[(a\widehat{X}^m_e + \widehat{Y}^m_e)\phi^m_e \phi^k_e |_{x_{e+1/2}} - (a\widehat{X}^m_{e-1} + \widehat{Y}^m_{e-1})\phi^m_{e-1}\phi^k_e |_{x_{e-1/2}} \right] \\
&\qquad - \int_{\Omega_e} \frac{\partial \phi^k_e}{\partial x}(aX^h + Y^h)\mathrm{d}x \Bigg\} \\
&= (M^{-1})^{jk}_e \Bigg\{ a\left[\widehat{X}^m_e \phi^m_e \phi^k_e |_{x_{e+1/2}} - \widehat{X}^m_{e-1}\phi^m_{e-1}\phi^k_e |_{x_{e-1/2}} \right] - a\int_{\Omega_e} \frac{\partial \phi^k_e}{\partial x} X^h \mathrm{d}x \\
&\qquad + \left[\widehat{Y}^m_e \phi^m_e \phi^j_e |_{x_{e+1/2}} - \widehat{Y}^m_{e-1}\phi^m_{e-1}\phi^j_e |_{x_{e-1/2}} \right] - \int_{\Omega_e} \frac{\partial \phi^k_e}{\partial x} Y^h \mathrm{d}x \Bigg\} \\
&= (M^{-1})^{jk}_e \left[aR^k_{f,e}(X) + R^k_{f,e}(Y) \right] = aD^k_{f,e}(X) + D^k_{f,e}(Y), \quad \text{(D.1)}
\end{aligned}
$$

$$
\begin{aligned}
D^j_{f,e}(a) = (M^{-1})^{jk}_e \Bigg\{ a\left[\phi^k_e \right]^{x_{e+1/2}}_{x_{e-1/2}} - a\int_{\Omega_e} \frac{\partial \phi^k_e}{\partial x}\mathrm{d}x \Bigg\} = \\
(M^{-1})^{jk}_e \Bigg\{ a\left[\phi^k_e \right]^{x_{e+1/2}}_{x_{e-1/2}} - a\left[\phi^k_e \right]^{x_{e+1/2}}_{x_{e-1/2}} \Bigg\} = 0. \quad \text{(D.2)}
\end{aligned}
$$

We also make use of the properties of the non-conservative advection, diffusion, and source term discretization operators:

$$
D^j_{h,e}(0) = -(M^{-1})^{jk}_e \left\{ \left[\{\phi^k_e\}(0) \right]^{x_{e+1/2}}_{x_{e-1/2}} - \int_{\Omega_e} \phi^k_e(0)\mathrm{d}x \right\} = 0, \quad \text{(D.3)}
$$

$$
D^j_{g,e}(0) = -(M^{-1})^{jk}_e \left\{ \left[\phi^k_e(0) \right]^{x_{e+1/2}}_{x_{e-1/2}} - \int_{\Omega_e} (0)\frac{\partial \phi^k_e}{\partial x}\mathrm{d}x \right\} = 0. \quad \text{(D.4)}
$$

$$
D^j_{s,e}(0) = -(M^{-1})^{jk}_e \left\{ \int_{\Omega_e} \phi^k_e(0)\mathrm{d}x \right\} = 0. \quad \text{(D.5)}
$$

D.2 Properties of HR limiting

We now verify the nonlinear properties of HR limiting mentioned in Section 3.6.2 following the proofs in Ref. [196].

D.2.1 Addition

We consider the sum $Q = X + Y$, with two different limiting approaches: $\widetilde{Q} = \widetilde{X + Y}$, and $\widetilde{\widetilde{Q}} = \widetilde{X} + \widetilde{Y}$. We consider three adjacent computational cells, $e-1$, e, and $e+1$. Without loss of generality, we assume $P = 1$. In this case, we write the Taylor polynomial representation of the variables as,

$$X(x) = \widehat{X}^0 + \widehat{X}^1 x, \quad Y(x) = \widehat{Y}^0 + \widehat{Y}^1 x, \tag{D.6}$$

before limiting, and

$$\widetilde{X}(x) = \widetilde{\widehat{X}^0} + \widetilde{\widehat{X}^1} x, \quad \widetilde{Y}(x) = \widetilde{\widehat{Y}^0} + \widetilde{\widehat{Y}^1} x, \tag{D.7}$$

after limiting in each cell. HR limiting with MUSCL reconstruction gives:

$$\widetilde{\widehat{X}_e^1} = \frac{1}{2}\text{minmod}\left\{\widehat{X}_e^0 - \widehat{X}_{e-1}^0, \quad \widehat{X}_{e+1}^0 - \widehat{X}_e^0\right\}, \tag{D.8a}$$

$$\widetilde{\widehat{Y}_e^1} = \frac{1}{2}\text{minmod}\left\{\widehat{Y}_e^0 - \widehat{Y}_{e-1}^0, \quad \widehat{Y}_{e+1}^0 - \widehat{Y}_e^0\right\}. \tag{D.8b}$$

Applying the limiting procedure to the sum of the two variables, we obtain

$$\begin{aligned}\widetilde{\widehat{Q}_e^1} &= \frac{1}{2}\text{minmod}\left\{\widehat{Q}_e^0 - \widehat{Q}_{e-1}^0, \quad \widehat{Q}_{e+1}^0 - \widehat{Q}_e^0\right\} \\ &= \frac{1}{2}\text{minmod}\left\{(\widehat{X}_e^0 - \widehat{X}_{e-1}^0) + (\widehat{Y}_e^0 - \widehat{Y}_{e-1}^0), (\widehat{X}_{e+1}^0 - \widehat{X}_e^0) + (\widehat{Y}_{e+1}^0 - \widehat{Y}_e^0)\right\}.\end{aligned} \tag{D.9}$$

Instead, summing the individually limited variables,

$$\widetilde{\widehat{Q}}_e^1 = \frac{1}{2}\text{minmod}\left\{\widehat{X}_e^0 - \widehat{X}_{e-1}^0, \quad \widehat{X}_{e+1}^0 - \widehat{X}_e^0\right\} + \frac{1}{2}\text{minmod}\left\{\widehat{Y}_e^0 - \widehat{Y}_{e-1}^0, \quad \widehat{Y}_{e+1}^0 - \widehat{Y}_e^0\right\}. \tag{D.10}$$

Because we have, in general, $\text{minmod}(x_1+y_1, x_2+y_2) \neq \text{minmod}(x_1, x_2)+\text{minmod}(y_1, y_2)$, we have that $\widetilde{\widehat{Q}}_e^1 \neq \widetilde{\widehat{Q}}_e^1$, so $\widetilde{X+Y} \neq \widetilde{X} + \widetilde{Y}$.

D.2.2 Multiplication

Now, we let $Q = XY$, and $\widetilde{Q} = \widetilde{X}\widetilde{Y}$ in element e. By Equation (3.67), we have

$$\widehat{Q}^0 = \widehat{X}^0\widehat{Y}^0, \qquad \widehat{Q}^1 = \widehat{X}^0\widehat{Y}^1 + \widehat{X}^1\widehat{Y}^0, \tag{D.11}$$

and in the other case,

$$\widetilde{\widehat{Q}^0} = \widetilde{\widehat{X}^0}\widetilde{\widehat{Y}^0}, \qquad \widetilde{\widehat{Q}^1} = \widetilde{\widehat{X}^0}\widetilde{\widehat{Y}^1} + \widetilde{\widehat{X}^1}\widetilde{\widehat{Y}^0}, \tag{D.12}$$

We evaluate the element averages of Q and $\widetilde{Q}$ over the reference element $x \in [-1, 1]$,

$$\frac{1}{2}\int_{\Omega_e} Q\mathrm{d}x = \frac{1}{2}\widehat{Q}^0 = \frac{1}{2}\widehat{X}^0\widehat{Y}^0 \tag{D.13}$$

$$\frac{1}{2}\int_{\Omega_e} \widetilde{Q}\mathrm{d}x = \frac{1}{2}\widetilde{\widehat{Q}^0} = \frac{1}{2}\widetilde{\widehat{X}^0}\widetilde{\widehat{Y}^0}. \tag{D.14}$$

Comparing the two, we see that in general $\int_{\Omega_e} Q\mathrm{d}x \neq \int_{\Omega_e} \widetilde{Q}\mathrm{d}x$.

BIBLIOGRAPHY

BIBLIOGRAPHY

[1] National Research Council, *Frontiers in High Energy Density Physics: The X-Games of Contemporary Science*. National Academies Press, Washington, DC, 2003.

[2] R. P. Drake, "Perspectives on high-energy-density physics," *Physics of Plasmas*, vol. 16, no. 5, p. 055501, 2009.

[3] M. S. Murillo, "Strongly coupled plasma physics and high energy-density matter," *Physics of Plasmas*, vol. 11, no. 5, pp. 2964–2971, 2004.

[4] S. D. Baalrud, "Transport coefficients in strongly coupled plasmas," *Physics of Plasmas*, vol. 19, no. 3, p. 030701, 2012.

[5] S. D. Bergeson, S. D. Baalrud, C. L. Ellison, E. Grant, F. R. Graziani, T. C. Killian, M. S. Murillo, J. L. Roberts, and L. G. Stanton, "Exploring the crossover between high-energy-density plasma and ultracold neutral plasma physics," *Physics of Plasmas*, vol. 26, no. 10, p. 100501, 2019.

[6] R. Drake, F. Doss, R. McClarren, M. Adams, N. Amato, D. Bingham, C. Chou, C. DiStefano, K. Fidkowski, B. Fryxell, T. Gombosi, M. Grosskopf, J. Holloway, B. van der Holst, C. Huntington, S. Karni, C. Krauland, C. Kuranz, E. Larsen, B. van Leer, B. Mallick, D. Marion, W. Martin, J. Morel, E. Myra, V. Nair, K. Powell, L. Rauchwerger, P. Roe, E. Rutter, I. Sokolov, Q. Stout, B. Torralva, G. Toth, K. Thornton, and A. Visco, "Radiative effects in radiative shocks in shock tubes," *High Energy Density Physics*, vol. 7, no. 3, pp. 130–140, 2011.

[7] A. J. Visco, R. P. Drake, S. H. Glenzer, T. Döppner, G. Gregori, D. H. Froula, and M. J. Grosskopf, "Measurement of Radiative Shock Properties by X-Ray Thomson Scattering," *Phys. Rev. Lett.*, vol. 108, p. 145001, Apr 2012.

[8] J. Colgan, J. Abdallah, A. Y. Faenov, S. A. Pikuz, E. Wagenaars, N. Booth, O. Culfa, R. J. Dance, R. G. Evans, R. J. Gray, T. Kaempfer, K. L. Lancaster, P. McKenna, A. L. Rossall, I. Y. Skobelev, K. S. Schulze, I. Uschmann, A. G. Zhidkov, and N. C. Woolsey, "Exotic Dense-Matter States Pumped by a Relativistic Laser Plasma in the Radiation-Dominated Regime," *Phys. Rev. Lett.*, vol. 110, p. 125001, Mar 2013.

[9] D. Umstadter, "Relativistic laser plasma interactions," *Journal of Physics D: Applied Physics*, vol. 36, pp. R151–R165, apr 2003.

[10] D. Gordon, K. C. Tzeng, C. E. Clayton, A. E. Dangor, V. Malka, K. A. Marsh, A. Modena, W. B. Mori, P. Muggli, Z. Najmudin, D. Neely, C. Danson, and C. Joshi, "Observation of Electron Energies Beyond the Linear Dephasing Limit from a Laser-Excited Relativistic Plasma Wave," *Phys. Rev. Lett.*, vol. 80, pp. 2133–2136, Mar 1998.

[11] S. X. Hu, "Continuum Lowering and Fermi-Surface Rising in Strongly Coupled and Degenerate Plasmas," *Phys. Rev. Lett.*, vol. 119, p. 065001, Aug 2017.

[12] H. J. Lee, P. Neumayer, J. Castor, T. Döppner, R. W. Falcone, C. Fortmann, B. A. Hammel, A. L. Kritcher, O. L. Landen, R. W. Lee, D. D. Meyerhofer, D. H. Munro, R. Redmer, S. P. Regan, S. Weber, and S. H. Glenzer, "X-Ray Thomson-Scattering Measurements of Density and Temperature in Shock-Compressed Beryllium," *Phys. Rev. Lett.*, vol. 102, p. 115001, Mar 2009.

[13] C. A. Haynam, P. J. Wegner, J. M. Auerbach, M. W. Bowers, S. N. Dixit, G. V. Erbert, G. M. Heestand, M. A. Henesian, M. R. Hermann, K. S. Jancaitis, K. R. Manes, C. D. Marshall, N. C. Mehta, J. Menapace, E. Moses, J. R. Murray, M. C. Nostrand, C. D. Orth, R. Patterson, R. A. Sacks, M. J. Shaw, M. Spaeth, S. B. Sutton, W. H. Williams, C. C. Widmayer, R. K. White, S. T. Yang, and B. M. V. Wonterghem, "National Ignition Facility laser performance status," *Appl. Opt.*, vol. 46, pp. 3276–3303, Jun 2007.

[14] T. Boehly, D. Brown, R. Craxton, R. Keck, J. Knauer, J. Kelly, T. Kessler, S. Kumpan, S. Loucks, S. Letzring, F. Marshall, R. McCrory, S. Morse, W. Seka, J. Soures, and C. Verdon, "Initial performance results of the OMEGA laser system," *Optics Communications*, vol. 133, no. 1, pp. 495–506, 1997.

[15] A. Casner, T. Caillaud, S. Darbon, A. Duval, I. Thfouin, J. Jadaud, J. LeBreton, C. Reverdin, B. Rosse, R. Rosch, N. Blanchot, B. Villette, R. Wrobel, and J. Miquel, "LMJ/PETAL laser facility: Overview and opportunities for laboratory astrophysics," *High Energy Density Physics*, vol. 17, pp. 2–11, 2015. 10th International Conference on High Energy Density Laboratory Astrophysics.

[16] J. D. Sethian, A. E. Robson, K. A. Gerber, and A. W. DeSilva, "Enhanced stability and neutron production in a dense z-pinch plasma formed from a frozen deuterium fiber," *Phys. Rev. Lett.*, vol. 59, pp. 1790–1790, Oct 1987.

[17] D. Strickland and G. Mourou, "Compression of amplified chirped optical pulses," *Optics Communications*, vol. 55, no. 6, pp. 447–449, 1985.

[18] M. Barrios, K. Fournier, S. Regan, O. Landen, M. May, Y. Opachich, K. Widmann, D. Bradley, and G. Collins, "Backlighter development at the National Ignition Facility (NIF): Zinc to zirconium," *High Energy Density Physics*, vol. 9, no. 3, pp. 626–634, 2013.

[19] S. R. Nagel, T. J. Hilsabeck, P. M. Bell, D. K. Bradley, M. J. Ayers, M. A. Barrios, B. Felker, R. F. Smith, G. W. Collins, O. S. Jones, J. D. Kilkenny,

T. Chung, K. Piston, K. S. Raman, B. Sammuli, J. D. Hares, and A. K. L. Dymoke-Bradshaw, "Dilation x-ray imager a new/faster gated x-ray imager for the NIF," *Review of Scientific Instruments*, vol. 83, no. 10, p. 10E116, 2012.

[20] A. Kritcher, T. Döppner, D. Swift, J. Hawreliak, G. Collins, J. Nilsen, B. Bachmann, E. Dewald, D. Strozzi, S. Felker, O. Landen, O. Jones, C. Thomas, J. Hammer, C. Keane, H. Lee, S. Glenzer, S. Rothman, D. Chapman, D. Kraus, P. Neumayer, and R. Falcone, "Probing matter at gbar pressures at the nif," *High Energy Density Physics*, vol. 10, pp. 27–34, 2014.

[21] D. C. Eder, A. T. Anderson, D. G. Braun, and M. T. Tobin, "Ablation of NIF targets and diagnostic components by high-power lasers and x rays from high-temperature plasmas," in *High-Power Laser Ablation III* (C. R. Phipps, ed.), vol. 4065, pp. 86 – 96, International Society for Optics and Photonics, SPIE, 2000.

[22] T. W. L. Sanford, R. E. Olson, R. L. Bowers, G. A. Chandler, M. S. Derzon, D. E. Hebron, R. J. Leeper, R. C. Mock, T. J. Nash, D. L. Peterson, L. E. Ruggles, W. W. Simpson, K. W. Struve, and R. A. Vesey, "Z-Pinch-Generated X Rays Demonstrate Potential for Indirect-Drive ICF Experiments," *Phys. Rev. Lett.*, vol. 83, pp. 5511–5514, Dec 1999.

[23] C. Thoma, D. R. Welch, R. E. Clark, D. V. Rose, and I. E. Golovkin, "Hybrid-PIC modeling of laser-plasma interactions and hot electron generation in gold hohlraum walls," *Physics of Plasmas*, vol. 24, no. 6, p. 062707, 2017.

[24] A. Y. Faenov, T. A. Pikuz, P. Mabey, B. Albertazzi, T. Michel, G. Rigon, S. A. Pikuz, A. Buzmakov, S. Makarov, N. Ozaki, T. Matsuoka, K. Katagiri, K. Miyanishi, K. Takahashi, K. A. Tanaka, Y. Inubushi, T. Togashi, T. Yabuuchi, M. Yabashi, A. Casner, R. Kodama, and M. Koenig, "Advanced high resolution x-ray diagnostic for HEDP experiments," *Scientific Reports*, vol. 8, no. 1, p. 16407, 2018.

[25] D. Mihalas and B. W. Mihalas, *Foundations of Radiation Hydrodynamics*. Courier Corporation, 2013.

[26] É. Falize, S. Bouquet, and C. Michaut, "Radiation hydrodynamics scaling laws in high energy density physics and laboratory astrophysics," *Journal of Physics: Conference Series*, vol. 112, p. 042016, may 2008.

[27] T. Ma, D. Mariscal, R. Anirudh, T. Bremer, B. Z. Djordjevic, T. Galvin, E. Grace, S. Herriot, S. Jacobs, B. Kailkhura, R. Hollinger, J. Kim, S. Liu, J. Ludwig, D. Neely, J. J. Rocca, G. G. Scott, R. A. Simpson, B. S. Spears, T. S. Spinka, K. Swanson, J. J. Thiagarajan, B. V. Essen, S. Wang, S. C. Wilks, G. J. Williams, J. Zhang, M. C. Herrmann, and C. Haefner, "Accelerating the rate of discovery: toward high-repetition-rate HED science," *Plasma Physics and Controlled Fusion*, vol. 63, p. 104003, sep 2021.

[28] D. S. Clark, M. M. Marinak, C. R. Weber, D. C. Eder, S. W. Haan, B. A. Hammel, D. E. Hinkel, O. S. Jones, J. L. Milovich, P. K. Patel, H. F. Robey, J. D. Salmonson, S. M. Sepke, and C. A. Thomas, "Radiation hydrodynamics modeling of the highest compression inertial confinement fusion ignition experiment from the National Ignition Campaign," *Physics of Plasmas*, vol. 22, no. 2, p. 022703, 2015.

[29] A. B. Zylstra, R. Nora, P. Patel, and O. Hurricane, "Model validation for inferred hot-spot conditions in national ignition facility experiments," *Physics of Plasmas*, vol. 28, no. 12, p. 122703, 2021.

[30] D. R. Leibrandt, R. P. Drake, A. B. Reighard, and S. G. Glendinning, "A validation test of the flux-limited diffusion approximation for radiation hydrodynamics," *The Astrophysical Journal*, vol. 626, pp. 616–625, jun 2005.

[31] W. A. Farmer, C. Bruulsema, G. F. Swadling, M. W. Sherlock, M. D. Rosen, W. Rozmus, D. H. Edgell, J. Katz, B. B. Pollock, and J. S. Ross, "Validation of heat transport modeling using directly driven beryllium spheres," *Physics of Plasmas*, vol. 27, no. 8, p. 082701, 2020.

[32] D. E. Keyes, L. C. McInnes, C. Woodward, W. Gropp, E. Myra, M. Pernice, J. Bell, J. Brown, A. Clo, J. Connors, E. Constantinescu, D. Estep, K. Evans, C. Farhat, A. Hakim, G. Hammond, G. Hansen, J. Hill, T. Isaac, X. Jiao, K. Jordan, D. Kaushik, E. Kaxiras, A. Koniges, K. Lee, A. Lott, Q. Lu, J. Magerlein, R. Maxwell, M. McCourt, M. Mehl, R. Pawlowski, A. P. Randles, D. Reynolds, B. Rivière, U. Rüde, T. Scheibe, J. Shadid, B. Sheehan, M. Shephard, A. Siegel, B. Smith, X. Tang, C. Wilson, and B. Wohlmuth, "Multiphysics simulations: Challenges and opportunities," *The International Journal of High Performance Computing Applications*, vol. 27, no. 1, pp. 4–83, 2013.

[33] J. Geiser, "Recent advances in splitting methods for multiphysics and multiscale: Theory and applications," *Journal of Algorithms & Computational Technology*, vol. 9, no. 1, pp. 65–93, 2015.

[34] S. Boscarino and G. Russo, "On a class of uniformly accurate imex runge–kutta schemes and applications to hyperbolic systems with relaxation," *SIAM Journal on Scientific Computing*, vol. 31, no. 3, pp. 1926–1945, 2009.

[35] J. Kou and W. Zhang, "Data-driven modeling for unsteady aerodynamics and aeroelasticity," *Progress in Aerospace Sciences*, vol. 125, p. 100725, 2021.

[36] W. Yan, S. Lin, O. L. Kafka, Y. Lian, C. Yu, Z. Liu, J. Yan, S. Wolff, H. Wu, E. Ndip-Agbor, M. Mozaffar, K. Ehmann, J. Cao, G. J. Wagner, and W. K. Liu, "Data-driven multi-scale multi-physics models to derive process–structure–property relationships for additive manufacturing," *Computational Mechanics*, vol. 61, no. 5, pp. 521–541, 2018.

[37] P. W. Hatfield, J. A. Gaffney, G. J. Anderson, S. Ali, L. Antonelli, S. Başeğmez du Pree, J. Citrin, M. Fajardo, P. Knapp, B. Kettle, B. Kustowski, M. J. MacDonald, D. Mariscal, M. E. Martin, T. Nagayama, C. A. J. Palmer, J. L. Peterson, S. Rose, J. J. Ruby, C. Shneider, M. J. V. Streeter, W. Trickey, and B. Williams, "The data-driven future of high-energy-density physics," *Nature*, vol. 593, no. 7859, pp. 351–361, 2021.

[38] L. Spitzer, *Physical Processes in the Interstellar Medium*. John Wiley & Sons, 1978.

[39] H. W. Yorke, "The Dynamical Evolution of H II Regions—Recent Theoretical Developments," *Annual Review of Astronomy and Astrophysics*, vol. 24, no. 1, pp. 49–87, 1986.

[40] M. W. Pound, "Molecular Gas in the Eagle Nebula," *The Astrophysical Journal*, vol. 493, pp. L113–L116, feb 1998.

[41] K. Sugitani, M. Tamura, Y. Nakajima, C. Nagashima, T. Nagayama, H. Nakaya, A. J. Pickles, T. Nagata, S. Sato, N. Fukuda, and K. Ogura, "Near-Infrared Study of M16: Star Formation in the Elephant Trunks," *The Astrophysical Journal*, vol. 565, pp. L25–L28, jan 2002.

[42] G. I. Taylor, "The instability of liquid surfaces when accelerated in a direction perpendicular to their planes. i," *Proceedings of the Royal Society of London. Series A. Mathematical and Physical Sciences*, vol. 201, no. 1065, pp. 192–196, 1950.

[43] E. Frieman, "On Elephant-Trunk Structures in the Region of O Associations," *The Astrophysical Journal*, vol. 120, p. 18, 1954.

[44] L. Spitzer Jr, "Behavior of Matter in Space," *The Astrophysical Journal*, vol. 120, p. 1, 1954.

[45] A. Mizuta, J. O. Kane, M. W. Pound, B. A. Remington, D. D. Ryutov, and H. Takabe, "Formation of Pillars at the Boundaries between H-II Regions and Molecular Clouds," *The Astrophysical Journal*, vol. 647, pp. 1151–1158, aug 2006.

[46] B. Reipurth, "Star formation in BOK globules and low-mass clouds. I-The cometary globules in the GUM Nebula," *Astronomy and Astrophysics*, vol. 117, pp. 183–198, 1983.

[47] F. Bertoldi and C. F. McKee, "The photoevaporation of interstellar clouds. II-Equilibrium cometary clouds," *The Astrophysical Journal*, vol. 354, pp. 529–548, 1990.

[48] J. Kane, A. Mizuta, M. Pound, B. Remington, and D. Ryutov, *Molecular Clouds: Observation to Experiment*, pp. 261–265. Dordrecht: Springer Netherlands, 2005.

[49] S. Woosley and T. Janka, "The physics of core-collapse supernovae," *Nature Physics*, vol. 1, pp. 147–154, 2005.

[50] S. M. Couch, "The mechanism(s) of core-collapse supernovae," *Phil. Trans. R. Soc. A*, vol. 375, p. 20160271, 2017.

[51] H.-T. Janka, K. Langanke, A. Marek, G. Martínez-Pinedo, and B. Müller, "Theory of core-collapse supernovae," *Physics Reports*, vol. 442, no. 1, pp. 38–74, 2007. The Hans Bethe Centennial Volume 1906-2006.

[52] M. Schwarzschild, *Structure and Evolution of Stars*, vol. 2379. Princeton University Press, 2015.

[53] C. L. Fryer and K. C. B. New, "Gravitational Waves from Gravitational Collapse," *Living Reviews in Relativity*, vol. 6, no. 2, 2003.

[54] J. José and C. Iliadis, "Nuclear astrophysics: the unfinished quest for the origin of the elements," *Reports on Progress in Physics*, vol. 74, p. 096901, aug 2011.

[55] C. C. Kuranz, R. P. Drake, E. C. Harding, M. J. Grosskopf, H. F. Robey, B. A. Remington, M. J. Edwards, A. R. Miles, T. S. Perry, B. E. Blue, T. Plewa, N. C. Hearn, J. P. Knauer, D. Arnett, and D. R. Leibrandt, "Two-dimensional blast-wave-driven Rayleigh-Taylor Instability: Experiment and simulation," *The Astrophysical Journal*, vol. 696, pp. 749–759, apr 2009.

[56] C. C. Kuranz, H.-S. Park, C. M. Huntington, A. R. Miles, B. A. Remington, T. Plewa, M. R. Trantham, H. F. Robey, D. Shvarts, A. Shimony, K. Raman, S. MacLaren, W. C. Wan, F. W. Doss, J. Kline, K. A. Flippo, G. Malamud, T. A. Handy, S. Prisbrey, C. M. Krauland, S. R. Klein, E. C. Harding, R. Wallace, M. J. Grosskopf, D. C. Marion, D. Kalantar, E. Giraldez, and R. P. Drake, "How high energy fluxes may affect Rayleigh–Taylor instability growth in young supernova remnants," *Nature Communications*, vol. 9, no. 1, p. 1564, 2018.

[57] S. I. Abarzhi, A. K. Bhowmick, A. Naveh, A. Pandian, N. C. Swisher, R. F. Stellingwerf, and W. D. Arnett, "Supernova, nuclear synthesis, fluid instabilities, and interfacial mixing," *Proceedings of the National Academy of Sciences*, vol. 116, no. 37, pp. 18184–18192, 2019.

[58] R. Toschi, "Nuclear fusion, an energy source," *Fusion Engineering and Design*, vol. 36, no. 1, pp. 1–8, 1997.

[59] J. D. Lawson, "Some criteria for a power producing thermonuclear reactor," *Proceedings of the Physical Society. Section B*, vol. 70, pp. 6–10, jan 1957.

[60] E. Teller and S. Ulam, "On Heterocatalytic Detonations I. Hydrodynamic Lenses and Radiation Mirrors," tech. rep., Los Alamos National Laboratory, Los Alamos, NM (United States), 1951.

[61] R. Betti and O. Hurricane, "Inertial-confinement fusion with lasers," *Nature Phys.*, vol. 12, pp. 435–448, 2016.

[62] D. Clery, "Alternatives to tokamaks: a faster-better-cheaper route to fusion energy?," *Philosophical Transactions of the Royal Society A: Mathematical, Physical and Engineering Sciences*, vol. 377, no. 2141, p. 20170431, 2019.

[63] R. P. Drake, *High-Energy-Density Physics: Fundamentals, Inertial Fusion, and Experimental Astrophysics*. Springer, 2006.

[64] S. Pfalzner, *An Introduction to Inertial Confinement Fusion*. CRC Press, 2006.

[65] O. A. Hurricane, D. A. Callahan, D. T. Casey, E. L. Dewald, T. R. Dittrich, T. Döppner, S. Haan, D. E. Hinkel, L. F. Berzak Hopkins, O. Jones, A. L. Kritcher, S. Le Pape, T. Ma, A. G. Macphee, J. L. Milovich, J. Moody, A. Pak, H. S. Park, P. K. Patel, J. E. Ralph, H. F. Robey, J. S. Ross, J. D. Salmonson, B. K. Spears, P. T. Springer, R. Tommasini, F. Albert, L. R. Benedetti, R. Bionta, E. Bond, D. K. Bradley, J. Caggiano, P. M. Celliers, C. Cerjan, J. A. Church, R. Dylla-Spears, D. Edgell, M. J. Edwards, D. Fittinghoff, M. A. Barrios Garcia, A. Hamza, R. Hatarik, H. Herrmann, M. Hohenberger, D. Hoover, J. L. Kline, G. Kyrala, B. Kozioziemski, G. Grim, J. E. Field, J. Frenje, N. Izumi, M. Gatu Johnson, S. F. Khan, J. Knauer, T. Kohut, O. Landen, F. Merrill, P. Michel, A. Moore, S. R. Nagel, A. Nikroo, T. Parham, R. R. Rygg, D. Sayre, M. Schneider, D. Shaughnessy, D. Strozzi, R. P. Town, D. Turnbull, P. Volegov, A. Wan, K. Widmann, C. Wilde, and C. Yeamans, "Inertially confined fusion plasmas dominated by alpha-particle self-heating," *Nature Physics*, vol. 12, no. 8, 2016.

[66] J. Freeman, M. Clauser, and S. Thompson, "Rayleigh-Taylor instabilities in inertial-confinement fusion targets," *Nuclear Fusion*, vol. 17, pp. 223–230, apr 1977.

[67] A. Casner, "Recent progress in quantifying hydrodynamics instabilities and turbulence in inertial confinement fusion and high-energy-density experiments," *Philosophical Transactions of the Royal Society A: Mathematical, Physical and Engineering Sciences*, vol. 379, no. 2189, p. 20200021, 2021.

[68] A. B. Zylstra, O. A. Hurricane, D. A. Callahan, A. L. Kritcher, J. E. Ralph, H. F. Robey, J. S. Ross, C. V. Young, K. L. Baker, D. T. Casey, T. Döppner, L. Divol, M. Hohenberger, S. Le Pape, A. Pak, P. K. Patel, R. Tommasini, S. J. Ali, P. A. Amendt, L. J. Atherton, B. Bachmann, D. Bailey, L. R. Benedetti, L. Berzak Hopkins, R. Betti, S. D. Bhandarkar, J. Biener, R. M. Bionta, N. W. Birge, E. J. Bond, D. K. Bradley, T. Braun, T. M. Briggs, M. W. Bruhn, P. M. Celliers, B. Chang, T. Chapman, H. Chen, C. Choate, A. R. Christopherson, D. S. Clark, J. W. Crippen, E. L. Dewald, T. R. Dittrich, M. J. Edwards, W. A. Farmer, J. E. Field, D. Fittinghoff, J. Frenje, J. Gaffney, M. Gatu Johnson, S. H. Glenzer, G. P. Grim, S. Haan, K. D. Hahn, G. N. Hall, B. A. Hammel,

J. Harte, E. Hartouni, J. E. Heebner, V. J. Hernandez, H. Herrmann, M. C. Herrmann, D. E. Hinkel, D. D. Ho, J. P. Holder, W. W. Hsing, H. Huang, K. D. Humbird, N. Izumi, L. C. Jarrott, J. Jeet, O. Jones, G. D. Kerbel, S. M. Kerr, S. F. Khan, J. Kilkenny, Y. Kim, H. Geppert Kleinrath, V. Geppert Kleinrath, C. Kong, J. M. Koning, J. J. Kroll, M. K. G. Kruse, B. Kustowski, O. L. Landen, S. Langer, D. Larson, N. C. Lemos, J. D. Lindl, T. Ma, M. J. MacDonald, B. J. MacGowan, A. J. Mackinnon, S. A. MacLaren, A. G. MacPhee, M. M. Marinak, D. A. Mariscal, E. V. Marley, L. Masse, K. Meaney, N. B. Meezan, P. A. Michel, M. Millot, J. L. Milovich, J. D. Moody, A. S. Moore, J. W. Morton, T. Murphy, K. Newman, J.-M. G. Di Nicola, A. Nikroo, R. Nora, M. V. Patel, L. J. Pelz, J. L. Peterson, Y. Ping, B. B. Pollock, M. Ratledge, N. G. Rice, H. Rinderknecht, M. Rosen, M. S. Rubery, J. D. Salmonson, J. Sater, S. Schiaffino, D. J. Schlossberg, M. B. Schneider, C. R. Schroeder, H. A. Scott, S. M. Sepke, K. Sequoia, M. W. Sherlock, S. Shin, V. A. Smalyuk, B. K. Spears, P. T. Springer, M. Stadermann, S. Stoupin, D. J. Strozzi, L. J. Suter, C. A. Thomas, R. P. J. Town, E. R. Tubman, C. Trosseille, P. L. Volegov, C. R. Weber, K. Widmann, C. Wild, C. H. Wilde, B. M. Van Wonterghem, D. T. Woods, B. N. Woodworth, M. Yamaguchi, S. T. Yang, and G. B. Zimmerman, "Burning plasma achieved in inertial fusion," *Nature*, vol. 601, no. 7894, pp. 542–548, 2022.

[69] G. N. Minerbo, "Maximum entropy Eddington factors," *Journal of Quantitative Spectroscopy and Radiative Transfer*, vol. 20, no. 6, pp. 541–545, 1978.

[70] C. D. Levermore and G. C. Pomraning, "A flux-limited diffusion theory," *The Astrophysical Journal*, vol. 248, pp. 321–334, 1981.

[71] C. M. Lund and J. R. Wilson, "Some numerical methods for time-dependent multifrequency radiation transport calculations in one dimension," tech. rep., Lawrence Livermore National Laboratory, Livermore, CA (United States), 1980.

[72] J. Morel, "Diffusion-limit asymptotics of the transport equation, the P1/3 equations, and two flux-limited diffusion theories," *Journal of Quantitative Spectroscopy and Radiative Transfer*, vol. 65, no. 5, pp. 769–778, 2000.

[73] J. C. Hayes and M. L. Norman, "Beyond Flux-limited Diffusion: Parallel Algorithms for Multidimensional Radiation Hydrodynamics," *The Astrophysical Journal Supplement Series*, vol. 147, pp. 197–220, jul 2003.

[74] Y.-F. Jiang, J. M. Stone, and S. W. Davis, "A Godunov Method for Multidimensional Radiation Magnetohydrodynamics Based on a Variable Eddington Tensor," *The Astrophysical Journal Supplement Series*, vol. 199, p. 14, feb 2012.

[75] D. Balsara, "Fast and accurate discrete ordinates methods for multidimensional radiative transfer. part i, basic methods," *Journal of Quantitative Spectroscopy and Radiative Transfer*, vol. 69, no. 6, pp. 671–707, 2001.

[76] B. A. Whitney, "Monte Carlo radiative transfer," *Bulletin of the Astronomical Society of India*, vol. 39, pp. 101–127, Mar. 2011.

[77] *Dynamics of X-Ray-Irradiated Materials*, ch. 8, pp. 191–214. John Wiley & Sons, Ltd, 2011.

[78] R. B. Williams *et al.*, *Adaptive multigroup radiation diffusion.* PhD thesis, Massachusetts Institute of Technology, 2005.

[79] B. van der Holst, G. Tóth, I. V. Sokolov, K. G. Powell, J. P. Holloway, E. S. Myra, Q. Stout, M. L. Adams, J. E. Morel, S. Karni, B. Fryxell, and R. P. Drake, "CRASH: A Block-Adaptive-Mesh Code for Radiative Shock Hydrodynamics—Implementation and Verification," *The Astrophysical Journal Supplement Series*, vol. 194, p. 23, may 2011.

[80] J. T. Larsen and S. M. Lane, "Hyades—a plasma hydrodynamics code for dense plasma studies," *Journal of Quantitative Spectroscopy and Radiative Transfer*, vol. 51, no. 1, pp. 179–186, 1994. Special Issue Radiative Properties of Hot Dense Matter.

[81] C. Sijoy and S. Chaturvedi, "TRHD: Three-temperature radiation-hydrodynamics code with an implicit non-equilibrium radiation transport using a cell-centered monotonic finite volume scheme on unstructured-grids," *Computer Physics Communications*, vol. 190, pp. 98–119, 2015.

[82] M. W. Sincell, M. Gehmeyr, and D. Mihalas, "The quasi-stationary structure of radiating shock waves. II. The two-temperature fluid," *Shock Waves*, vol. 9, no. 6, pp. 403–411, 1999.

[83] M. W. Sincell, M. Gehmeyr, and D. Mihalas, "The quasi-stationary structure of radiating shock waves. II. The two-temperature fluid," *Shock Waves*, vol. 9, no. 6, pp. 403–411, 1999.

[84] L. Spitzer and R. Härm, "Transport phenomena in a completely ionized gas," *Phys. Rev.*, vol. 89, pp. 977–981, Mar 1953.

[85] C. Li, J. Gu, F. Ge, Z. Dai, and S. Zou, "Impact of different electron thermal conductivity models on the performance of cryogenic implosions," *Physics of Plasmas*, vol. 29, no. 4, p. 042702, 2022.

[86] R. C. Malone, R. L. McCrory, and R. L. Morse, "Indications of strongly flux-limited electron thermal conduction in laser-target experiments," *Phys. Rev. Lett.*, vol. 34, pp. 721–724, Mar 1975.

[87] M. S. Murillo, "Viscosity estimates of liquid metals and warm dense matter using the yukawa reference system," *High Energy Density Physics*, vol. 4, no. 1, pp. 49–57, 2008.

[88] P. Arnault, "Modeling viscosity and diffusion of plasma for pure elements and multicomponent mixtures from weakly to strongly coupled regimes," *High Energy Density Physics*, vol. 9, no. 4, pp. 711–721, 2013.

[89] D. Ryutov, R. P. Drake, J. Kane, E. Liang, B. A. Remington, and W. M. Wood-Vasey, "Similarity Criteria for the Laboratory Simulation of Supernova Hydrodynamics," *The Astrophysical Journal*, vol. 518, pp. 821–832, jun 1999.

[90] R. B. Lowrie and J. D. Edwards, "Radiative shock solutions with grey nonequilibrium diffusion," *Shock Waves*, vol. 18, no. 2, pp. 129–143, 2008.

[91] G. C. Pomraning, *The Equations of Radiation Hydrodynamics*. Courier Corporation, 2005.

[92] L. Arriola and J. M. Hyman, *Sensitivity Analysis for Uncertainty Quantification in Mathematical Models*, pp. 195–247. Dordrecht: Springer Netherlands, 2009.

[93] V. G. Eck, W. P. Donders, J. Sturdy, J. Feinberg, T. Delhaas, L. R. Hellevik, and W. Huberts, "A guide to uncertainty quantification and sensitivity analysis for cardiovascular applications," *International journal for numerical methods in biomedical engineering*, vol. 32, no. 8, p. e02755, 2016.

[94] B. R. Spies and T. M. Habashy, "Sensitivity analysis of crosswell electromagnetics," *Geophysics*, vol. 60, no. 3, pp. 834–845, 1995.

[95] T. Turányi, "Sensitivity analysis of complex kinetic systems. Tools and applications," *Journal of Mathematical Chemistry*, vol. 5, no. 3, pp. 203–248, 1990.

[96] C. Gourieroux, J. Laurent, and O. Scaillet, "Sensitivity analysis of Values at Risk," *Journal of Empirical Finance*, vol. 7, no. 3, pp. 225–245, 2000. Special issue on Risk Management.

[97] H. Rabitz, M. Kramer, and D. Dacol, "Sensitivity analysis in chemical kinetics," *Annual Review of Physical Chemistry*, vol. 34, no. 1, pp. 419–461, 1983.

[98] A. Saltelli, S. Tarantola, and K. P.-S. Chan, "A quantitative model-independent method for global sensitivity analysis of model output," *Technometrics*, vol. 41, no. 1, pp. 39–56, 1999.

[99] J. Helton, J. Johnson, C. Sallaberry, and C. Storlie, "Survey of sampling-based methods for uncertainty and sensitivity analysis," *Reliability Engineering & System Safety*, vol. 91, no. 10, pp. 1175–1209, 2006. The Fourth International Conference on Sensitivity Analysis of Model Output (SAMO 2004).

[100] Z. Wang, K. Fidkowski, R. Abgrall, F. Bassi, D. Caraeni, A. Cary, H. Deconinck, R. Hartmann, K. Hillewaert, H. Huynh, N. Kroll, G. May, P.-O. Persson, B. van Leer, and M. Visbal, "High-order CFD methods: current status and perspective," *International Journal for Numerical Methods in Fluids*, vol. 72, no. 8, pp. 811–845, 2013.

[101] P. Moin and K. Mahesh, "Direct Numerical Simulation: A Tool in Turbulence Research," *Annual Review of Fluid Mechanics*, vol. 30, pp. 539–578, Jan. 1998.

[102] G. E. Barter and D. L. Darmofal, "Shock capturing with pde-based artificial viscosity for dgfem: Part i. formulation," *Journal of Computational Physics*, vol. 229, no. 5, pp. 1810–1827, 2010.

[103] D. Zhang, C. Jiang, D. Liang, and L. Cheng, "A review on TVD schemes and a refined flux-limiter for steady-state calculations," *Journal of Computational Physics*, vol. 302, pp. 114–154, 2015.

[104] D. B. Sinars, M. A. Sweeney, C. S. Alexander, D. J. Ampleford, T. Ao, J. P. Apruzese, C. Aragon, D. J. Armstrong, K. N. Austin, T. J. Awe, A. D. Baczewski, J. E. Bailey, K. L. Baker, C. R. Ball, H. T. Barclay, S. Beatty, K. Beckwith, K. S. Bell, J. F. Benage, N. L. Bennett, K. Blaha, D. E. Bliss, J. J. Boerner, C. J. Bourdon, B. A. Branch, J. L. Brown, E. M. Campbell, R. B. Campbell, D. G. Chacon, G. A. Chandler, K. Chandler, P. J. Christenson, M. D. Christison, E. B. Christner, R. C. Clay, K. R. Cochrane, A. P. Colombo, B. M. Cook, C. A. Coverdale, M. E. Cuneo, J. S. Custer, A. Dasgupta, J.-P. Davis, M. P. Desjarlais, D. H. Dolan, J. D. Douglass, G. S. Dunham, S. Duwal, A. D. Edens, M. J. Edwards, E. G. Evstatiev, B. G. Farfan, J. R. Fein, E. S. Field, J. A. Fisher, T. M. Flanagan, D. G. Flicker, M. D. Furnish, B. R. Galloway, P. D. Gard, T. A. Gardiner, M. Geissel, J. L. Giuliani, M. E. Glinsky, M. R. Gomez, T. Gomez, G. P. Grim, K. D. Hahn, T. A. Haill, N. D. Hamlin, J. H. Hammer, S. B. Hansen, H. L. Hanshaw, E. C. Harding, A. J. Harvey-Thompson, D. Headley, M. C. Herrmann, M. H. Hess, C. Highstrete, O. A. Hurricane, B. T. Hutsel, C. A. Jennings, O. M. Johns, D. Johnson, M. D. Johnston, B. M. Jones, M. C. Jones, P. A. Jones, P. E. Kalita, R. J. Kamm, J. W. Kellogg, M. L. Kiefer, M. W. Kimmel, P. F. Knapp, M. D. Knudson, A. Kreft, G. R. Laity, P. W. Lake, D. C. Lamppa, W. L. Langston, J. S. Lash, K. R. LeChien, J. J. Leckbee, R. J. Leeper, G. T. Leifeste, R. W. Lemke, W. Lewis, S. A. Lewis, G. P. Loisel, Q. M. Looker, A. J. Lopez, D. J. Lucero, S. A. MacLaren, R. J. Magyar, M. A. Mangan, M. R. Martin, T. R. Mattsson, M. K. Matzen, A. J. Maurer, M. G. Mazarakis, R. D. McBride, H. S. McLean, C. A. McCoy, G. R. McKee, J. L. McKenney, A. R. Miles, J. A. Mills, M. D. Mitchell, N. W. Moore, C. E. Myers, T. Nagayama, G. Natoni, A. C. Owen, S. Patel, K. J. Peterson, T. D. Pointon, J. L. Porter, A. J. Porwitzky, S. Radovich, K. S. Raman, P. K. Rambo, W. D. Reinhart, G. K. Robertson, G. A. Rochau, S. Root, D. V. Rose, D. C. Rovang, C. L. Ruiz, D. E. Ruiz, D. Sandoval, M. E. Savage, M. E. Sceiford, M. A. Schaeuble, P. F. Schmit, M. S. Schollmeier, J. Schwarz, C. T. Seagle, A. B. Sefkow, D. B. Seidel, G. A. Shipley, J. Shores, L. Shulenburger, S. C. Simpson, S. A. Slutz, I. C. Smith, C. S. Speas, P. E. Specht, M. J. Speir, D. C. Spencer, P. T. Springer, A. M. Steiner, B. S. Stoltzfus, W. A. Stygar, J. Ward Thornhill, J. A. Torres, J. P. Townsend, C. Tyler, R. A. Vesey, P. E. Wakeland, T. J. Webb, E. A. Weinbrecht, M. R. Weis, D. R. Welch, J. L. Wise, M. Wu, D. A. Yager-Elorriaga, A. Yu, and E. P. Yu, "Review of pulsed power-driven high

energy density physics research on Z at Sandia," *Physics of Plasmas*, vol. 27, no. 7, p. 070501, 2020.

[105] J. M. Soures, R. L. McCrory, C. P. Verdon, A. Babushkin, R. E. Bahr, T. R. Boehly, R. Boni, D. K. Bradley, D. L. Brown, R. S. Craxton, J. A. Delettrez, W. R. Donaldson, R. Epstein, P. A. Jaanimagi, S. D. Jacobs, K. Kearney, R. L. Keck, J. H. Kelly, T. J. Kessler, R. L. Kremens, J. P. Knauer, S. A. Kumpan, S. A. Letzring, D. J. Lonobile, S. J. Loucks, L. D. Lund, F. J. Marshall, P. W. McKenty, D. D. Meyerhofer, S. F. B. Morse, A. Okishev, S. Papernov, G. Pien, W. Seka, R. Short, M. J. Shoup, M. Skeldon, S. Skupsky, A. W. Schmid, D. J. Smith, S. Swales, M. Wittman, and B. Yaakobi, "Direct-drive laser-fusion experiments with the OMEGA, 60-beam, >40 kJ, ultraviolet laser system," *Physics of Plasmas*, vol. 3, no. 5, pp. 2108–2112, 1996.

[106] M. J. May, J. D. Colvin, G. E. Kemp, M. A. Barrios, K. Widmann, R. Benjamin, D. Thorn, P. Poole, and B. Blue, "Development of high intensity x-ray sources at the National Ignition Facility," *Physics of Plasmas*, vol. 25, no. 5, p. 056302, 2018.

[107] H.-S. Park, K. T. Lorenz, R. M. Cavallo, S. M. Pollaine, S. T. Prisbrey, R. E. Rudd, R. C. Becker, J. V. Bernier, and B. A. Remington, "Viscous Rayleigh-Taylor Instability Experiments at High Pressure and Strain Rate," *Phys. Rev. Lett.*, vol. 104, p. 135504, Apr 2010.

[108] J. D. Lindl, P. Amendt, R. L. Berger, S. G. Glendinning, S. H. Glenzer, S. W. Haan, R. L. Kauffman, O. L. Landen, and L. J. Suter, "The physics basis for ignition using indirect-drive targets on the National Ignition Facility," *Physics of Plasmas*, vol. 11, no. 2, pp. 339–491, 2004.

[109] D. A. Callahan, O. A. Hurricane, J. E. Ralph, C. A. Thomas, K. L. Baker, L. R. Benedetti, L. F. Berzak Hopkins, D. T. Casey, T. Chapman, C. E. Czajka, E. L. Dewald, L. Divol, T. Döppner, D. E. Hinkel, M. Hohenberger, L. C. Jarrott, S. F. Khan, A. L. Kritcher, O. L. Landen, S. LePape, S. A. MacLaren, L. P. Masse, N. B. Meezan, A. E. Pak, J. D. Salmonson, D. T. Woods, N. Izumi, T. Ma, D. A. Mariscal, S. R. Nagel, J. L. Kline, G. A. Kyrala, E. N. Loomis, S. A. Yi, A. B. Zylstra, and S. H. Batha, "Exploring the limits of case-to-capsule ratio, pulse length, and picket energy for symmetric hohlraum drive on the National Ignition Facility Laser," *Physics of Plasmas*, vol. 25, no. 5, p. 056305, 2018.

[110] H.-S. Park, B. R. Maddox, E. Giraldez, S. P. Hatchett, L. T. Hudson, N. Izumi, M. H. Key, S. Le Pape, A. J. MacKinnon, A. G. MacPhee, P. K. Patel, T. W. Phillips, B. A. Remington, J. F. Seely, R. Tommasini, R. Town, J. Workman, and E. Brambrink, "High-resolution 17–75kev backlighters for high energy density experiments," *Physics of Plasmas*, vol. 15, no. 7, p. 072705, 2008.

[111] B. E. Blue, J. F. Hansen, and H. F. Robey, "Improved pinhole-apertured point-projection backlighter geometry," *Review of Scientific Instruments*, vol. 75, no. 10, pp. 3989–3991, 2004.

[112] J. R. Schwank, M. R. Shaneyfelt, and P. E. Dodd, "Radiation Hardness Assurance Testing of Microelectronic Devices and Integrated Circuits: Radiation Environments, Physical Mechanisms, and Foundations for Hardness Assurance," *IEEE Transactions on Nuclear Science*, vol. 60, no. 3, pp. 2074–2100, 2013.

[113] E. Stassinopoulos and J. Raymond, "The space radiation environment for electronics," *Proceedings of the IEEE*, vol. 76, no. 11, pp. 1423–1442, 1988.

[114] G. Lindström, M. Moll, and E. Fretwurst, "Radiation hardness of silicon detectors – a challenge from high-energy physics," *Nuclear Instruments and Methods in Physics Research Section A: Accelerators, Spectrometers, Detectors and Associated Equipment*, vol. 426, no. 1, pp. 1–15, 1999.

[115] J. R. Schwank, "Space and military radiation effects in silicon-on-insulator devices," tech. rep., Sandia National Laboratories, Albuquerque, NM (United States), 1996.

[116] M. Petaev, S. Jacobsen, J. Remo, R. Adams, and D. Sasselov, "Experimental Study of High-Energy Processing of Protoplanetary Materials," in *AGU Fall Meeting Abstracts*, vol. 2006, pp. MR53D–05, 2006.

[117] J. L. Remo, M. D. Furnish, and R. J. Lawerence, "Plasma-driven Z-pinch X-ray loading and momentum coupling in meteorite and planetary materials," *Journal of Plasma Physics*, vol. 79, no. 2, p. 121–141, 2013.

[118] S. P. Hau-Riege, *High-Intensity X-rays - Interaction with Matter: Processes in Plasmas, Clusters, Molecules and Solids*. John Wiley & Sons, 2012.

[119] J. E. Reaugh, A. Lutze, and G. Yonas, "Melt-dominated impulse experiments and calculations," tech. rep., Defense Atomic Support Agency, Washington, DC (United States), 1970.

[120] J. L. Remo and M. D. Furnish, "Analysis of Z-pinch shock wave experiments on meteorite and planetary materials," *International Journal of Impact Engineering*, vol. 35, no. 12, pp. 1516 – 1521, 2008. Hypervelocity Impact Proceedings of the 2007 Symposium.

[121] H. N. Kornblum, R. L. Kauffman, and J. A. Smith, "Measurement of 0.1–3-kev x rays from laser plasmas," *Review of Scientific Instruments*, vol. 57, no. 8, pp. 2179–2181, 1986.

[122] C. Sorce, J. Schein, F. Weber, K. Widmann, K. Campbell, E. Dewald, R. Turner, O. Landen, K. Jacoby, P. Torres, and D. Pellinen, "Soft x-ray power diagnostic improvements at the Omega Laser Facility," *Review of Scientific Instruments*, vol. 77, no. 10, p. 10E518, 2006.

[123] E. L. Dewald, K. M. Campbell, R. E. Turner, J. P. Holder, O. L. Landen, S. H. Glenzer, R. L. Kauffman, L. J. Suter, M. Landon, M. Rhodes, and D. Lee, "Dante soft x-ray power diagnostic for National Ignition Facility," *Review of Scientific Instruments*, vol. 75, no. 10, pp. 3759–3761, 2004.

[124] J. L. Bourgade, B. Villette, J. L. Bocher, J. Y. Boutin, S. Chiche, N. Dague, D. Gontier, J. P. Jadaud, B. Savale, R. Wrobel, and R. E. Turner, "DMX: An absolutely calibrated time-resolved broadband soft x-ray spectrometer designed for MJ class laser-produced plasmas (invited)," *Review of Scientific Instruments*, vol. 72, no. 1, pp. 1173–1182, 2001.

[125] J. A. Gaffney, S. T. Brandon, K. D. Humbird, M. K. G. Kruse, R. C. Nora, J. L. Peterson, and B. K. Spears, "Making inertial confinement fusion models more predictive," *Physics of Plasmas*, vol. 26, no. 8, p. 082704, 2019.

[126] M. J. May, K. Widmann, C. Sorce, H.-S. Park, and M. Schneider, "Uncertainty analysis technique for OMEGA Dante measurements," *Review of Scientific Instruments*, vol. 81, no. 10, p. 10E505, 2010.

[127] M. Kramer, J. Calo, and H. Rabitz, "An improved computational method for sensitivity analysis: Green's function method with 'AIM'," *Applied Mathematical Modelling*, vol. 5, no. 6, pp. 432–441, 1981.

[128] M. Ionescu-Bujor and D. G. Cacuci, "A Comparative Review of Sensitivity and Uncertainty Analysis of Large-Scale Systems—i: Deterministic Methods," *Nuclear Science and Engineering*, vol. 147, no. 3, pp. 189–203, 2004.

[129] C. D. Newlander, J. R. Place, R. J. Scammon, and E. R. Copus, "Nuclear Hardness Evaluation Procedures (NHEP) Program, Phase 1: Analytic Technique Survey," tech. rep., Air Force Weapons Laboratory, Kirtland Air Force Base, NM (United States), 1978.

[130] K. B. Fournier, J. Celeste, V. Rekow, D. R. Bopp, M. J. May, J. H. Fisher, R. Horton, C. D. Newlander, P. Jenkins, and K. Trautz, "A test cassette for x-ray-exposure experiments at the National Ignition Facility," *Review of Scientific Instruments*, vol. 81, no. 7, p. 075113, 2010.

[131] K. B. Fournier, C. G. Brown, M. F. Yeoman, J. H. Fisher, S. W. Seiler, D. Hinshelwood, S. Compton, F. R. Holdener, G. E. Kemp, C. D. Newlander, R. P. Gilliam, N. Froula, M. Lilly, J. F. Davis, M. A. Lerch, and B. E. Blue, "X-ray transport and radiation response assessment (XTRRA) experiments at the National Ignition Facility," *Review of Scientific Instruments*, vol. 87, no. 11, p. 11D421, 2016.

[132] N. W. Moore, K. S. Bell, H. Hilborn, B. N. Woodworth, M. Mesh, D. E. Bruss, B. C. Franke, P. L. Poole, R. J. Hohlfelder, T. Zarick, R. Romero, G. R.

Chantler, C. A. Esquivel, M. J. May, T. M. Flanagan, and B. E. Blue, "Sample test array and recovery (STAR) platform at the National Ignition Facility," *Review of Scientific Instruments*, vol. 92, no. 5, p. 053539, 2021.

[133] K. B. Fournier, M. J. May, J. D. Colvin, J. O. Kane, M. Schneider, E. Dewald, C. A. Thomas, S. Compton, R. E. Marrs, J. Moody, E. Bond, P. Michel, J. H. Fisher, C. D. Newlander, and J. F. Davis, "Multi-kev x-ray source development experiments on the National Ignition Facility," *Physics of Plasmas*, vol. 17, no. 8, p. 082701, 2010.

[134] D. H. Dolan and S. C. Jones, "Push-pull analysis of photonic Doppler velocimetry measurements," *Review of Scientific Instruments*, vol. 78, no. 7, p. 076102, 2007.

[135] R. J. Lawerence, "The equivalence of simple models for radiation-induced impulse," in *Shock Compression of Condensed Matter–1991*, pp. 785 – 788, Amsterdam: Elsevier, 1992.

[136] J. L. Remo, M. D. Furnish, and R. J. Lawerence, "Soft X-ray Shock Loading and Momentum Coupling in Meteorite Planetary Materials," tech. rep., Sandia National Laboratories, Albuquerque, NM (United States), 2010.

[137] R. J. Lawrence *et al.*, "Analytic models for pulsed x-ray impulse coupling," *AIP Conference Proceedings*, vol. 1426, no. 1, pp. 883–886, 2012.

[138] K. Zhang, W. Tang, and K. Fu, "Modeling of dynamic behavior of carbon fiber-reinforced polymer (cfrp) composite under x-ray radiation," *Materials*, vol. 11, no. 1, 2018.

[139] R. J. Procassini, D. E. Cullen, G. M. Greenman, and C. A. Hagmann, "Verification and validation of Mercury: a modern, Monte Carlo particle transport code," tech. rep., Lawrence Livermore National Laboratory, Livermore, CA (United States), 2004.

[140] R. Howerton, R. Dye, and S. T. Perkins, "Evaluated nuclear data library," tech. rep., Lawrence Livermore National Laboratory, Livermore, CA (United States), 1981.

[141] B. S. Ryujin, "Performance and portability in the Ares multi-physics code," tech. rep., Lawrence Livermore National Laboratory, Livermore, CA (United States), 2015.

[142] R. M. More, K. H. Warren, D. A. Young, and G. B. Zimmerman, "A new quotidian equation of state (QEOS) for hot dense matter," *The Physics of Fluids*, vol. 31, no. 10, pp. 3059–3078, 1988.

[143] D. A. Young and E. M. Corey, "A new global equation of state model for hot, dense matter," *Journal of Applied Physics*, vol. 78, no. 6, pp. 3748–3755, 1995.

[144] D. J. Steinberg, S. G. Cochran, and M. W. Guinan, "A constitutive model for metals applicable at high-strain rate," *Journal of Applied Physics*, vol. 51, no. 3, pp. 1498–1504, 1980.

[145] D. J. Steinberg and C. M. Lund, "A constitutive model for strain rates from 10^{-4} to 10^{6} s^{-1}," *Journal of Applied Physics*, vol. 65, no. 4, pp. 1528–1533, 1989.

[146] E. Lee, H. Hornig, and J. Kury, "Adiabatic expansion of high explosive detonation products," tech. rep., University of California Radiation Laboratory, Livermore, CA (United States), 1968.

[147] A. I. Burshtein, *Introduction to Thermodynamics and Kinetic Theory of Matter*. John Wiley & Sons, 2008.

[148] D. J. Steinberg, "Equation of state and strength properties of selected materials," tech. rep., Lawrence Livermore National Laboratory, Livermore, CA (United States), 1996.

[149] G. R. Johnson and W. H. Cook, "A constitutive model and data for metals subjected to large strains, high strain rates and high temperatures," *Proc. 7th Int. Symp. on Ballistics, The Hague, The Netherlands*, pp. 541–547, 1983.

[150] A. Manes, L. Peroni, M. Scapin, and M. Giglio, "Analysis of strain rate behavior of an Al 6061 T6 alloy," *Procedia Engineering*, vol. 10, pp. 3477–3482, 2011. 11th International Conference on the Mechanical Behavior of Materials (ICM11).

[151] M. J. D. Powell, "An efficient method for finding the minimum of a function of several variables without calculating derivatives," *The Computer Journal*, vol. 7, pp. 155–162, 01 1964.

[152] P. Virtanen, R. Gommers, T. E. Oliphant, M. Haberland, T. Reddy, D. Cournapeau, E. Burovski, P. Peterson, W. Weckesser, J. Bright, S. J. van der Walt, M. Brett, J. Wilson, K. J. Millman, N. Mayorov, A. R. J. Nelson, E. Jones, R. Kern, E. Larson, C. J. Carey, I. Polat, Y. Feng, E. W. Moore, J. VanderPlas, D. Laxalde, J. Perktold, R. Cimrman, I. Henriksen, E. A. Quintero, C. R. Harris, A. M. Archibald, A. H. Ribeiro, F. Pedregosa, P. van Mulbregt, A. Vijaykumar, A. P. Bardelli, A. Rothberg, A. Hilboll, A. Kloeckner, A. Scopatz, A. Lee, A. Rokem, C. N. Woods, C. Fulton, C. Masson, C. Häggström, C. Fitzgerald, D. A. Nicholson, D. R. Hagen, D. V. Pasechnik, E. Olivetti, E. Martin, E. Wieser, F. Silva, F. Lenders, F. Wilhelm, G. Young, G. A. Price, G.-L. Ingold, G. E. Allen, G. R. Lee, H. Audren, I. Probst, J. P. Dietrich, J. Silterra, J. T. Webber, J. Slavič, J. Nothman, J. Buchner, J. Kulick, J. L. Schönberger, J. V. de Miranda Cardoso, J. Reimer, J. Harrington, J. L. C. Rodríguez, J. Nunez-Iglesias, J. Kuczynski, K. Tritz, M. Thoma, M. Newville, M. Kümmerer, M. Bolingbroke, M. Tartre, M. Pak, N. J. Smith, N. Nowaczyk,

N. Shebanov, O. Pavlyk, P. A. Brodtkorb, P. Lee, R. T. McGibbon, R. Feldbauer, S. Lewis, S. Tygier, S. Sievert, S. Vigna, S. Peterson, S. More, T. Pudlik, T. Oshima, T. J. Pingel, T. P. Robitaille, T. Spura, T. R. Jones, T. Cera, T. Leslie, T. Zito, T. Krauss, U. Upadhyay, Y. O. Halchenko, and Y. Vázquez-Baeza, "SciPy 1.0: fundamental algorithms for scientific computing in Python," *Nature Methods*, vol. 17, no. 3, pp. 261–272, 2020.

[153] A. Eiger, K. Sikorski, and F. Stenger, "A Bisection Method for Systems of Nonlinear Equations," *ACM Trans. Math. Softw.*, vol. 10, no. 4, p. 367–377, 1984.

[154] L. N. Trefethen and D. Bau III, *Numerical linear algebra*. Siam, 1997.

[155] J. J. Valencia and P. N. Quested, "Thermophysical Properties," in *Metals Process Simulation*, ASM International, 11 2010.

[156] A. Kramida, Yu. Ralchenko, J. Reader, and and NIST ASD Team. NIST Atomic Spectra Database (ver. 5.9), [Online]. Available: `https://physics.nist.gov/asd` [2022, June 12]. National Institute of Standards and Technology, Gaithersburg, MD., 2021.

[157] Y. Zhou, T. T. Clark, D. S. Clark, S. Gail Glendinning, M. Aaron Skinner, C. M. Huntington, O. A. Hurricane, A. M. Dimits, and B. A. Remington, "Turbulent mixing and transition criteria of flows induced by hydrodynamic instabilities," *Physics of Plasmas*, vol. 26, no. 8, p. 080901, 2019.

[158] M. Gittings, R. Weaver, M. Clover, T. Betlach, N. Byrne, R. Coker, E. Dendy, R. Hueckstaedt, K. New, W. R. Oakes, D. Ranta, and R. Stefan, "The RAGE radiation-hydrodynamic code," *Computational Science & Discovery*, vol. 1, p. 015005, nov 2008.

[159] S. H. Langer, I. Karlin, and M. M. Marinak, "Performance Characteristics of HYDRA - a Multi-Physics Simulation Code from LLNL," tech. rep., Lawrence Livermore National Laboratory, Livermore, CA (United States), 2015.

[160] M. M. Marinak, G. D. Kerbel, N. A. Gentile, O. Jones, D. Munro, S. Pollaine, T. R. Dittrich, and S. W. Haan, "Three-dimensional HYDRA simulations of National Ignition Facility targets," *Physics of Plasmas*, vol. 8, no. 5, pp. 2275–2280, 2001.

[161] D. S. Clark, A. L. Kritcher, J. L. Milovich, J. D. Salmonson, C. R. Weber, S. W. Haan, B. A. Hammel, D. E. Hinkel, M. M. Marinak, M. V. Patel, and S. M. Sepke, "Capsule modeling of high foot implosion experiments on the National Ignition Facility," *Plasma Physics and Controlled Fusion*, vol. 59, p. 055006, mar 2017.

[162] G. Alfonsi, "Reynolds-Averaged Navier–Stokes Equations for Turbulence Modeling," *Applied Mechanics Reviews*, vol. 62, 06 2009. 040802.

[163] P. Sagaut, *Large Eddy Simulation for Incompressible Flows*. Springer, 2006.

[164] F. F. Grinstein, L. G. Margolin, and W. J. Rider, eds., *Implicit Large Eddy Simulation: Computing Turbulent Flow Dynamics*. Cambridge University Press, 2010.

[165] P. Moin and K. Mahesh, "DIRECT NUMERICAL SIMULATION: A Tool in Turbulence Research," *Annual Review of Fluid Mechanics*, vol. 30, no. 1, pp. 539–578, 1998.

[166] K. A. Flippo, F. W. Doss, E. C. Merritt, B. G. DeVolder, C. A. Di Stefano, P. A. Bradley, D. Capelli, T. Cardenas, T. R. Desjardins, F. Fierro, C. M. Huntington, J. L. Kline, L. Kot, S. Kurien, E. N. Loomis, S. A. MacLaren, T. J. Murphy, S. R. Nagel, T. S. Perry, R. B. Randolph, A. Rasmus, and D. W. Schmidt, "Late-time mixing and turbulent behavior in high-energy-density shear experiments at high atwood numbers," *Physics of Plasmas*, vol. 25, no. 5, p. 056315, 2018.

[167] K. Raman, J. Bender, C. Huntington, S. MacLaren, S. Nagel, and S. Prisbrey, "Evaluating turbulence models at high energy densities," *NNSA Stewardship Science Today*, vol. 2, 3 2020.

[168] J. D. Bender, O. Schilling, K. S. Raman, R. A. Managan, B. J. Olson, S. R. Copeland, C. L. Ellison, D. J. Erskine, C. M. Huntington, B. E. Morgan, and et al., "Simulation and flow physics of a shocked and reshocked high-energy-density mixing layer," *Journal of Fluid Mechanics*, vol. 915, p. A84, 2021.

[169] G. Viciconte, B.-J. Gréa, F. S. Godeferd, P. Arnault, and J. Clérouin, "Sudden diffusion of turbulent mixing layers in weakly coupled plasmas under compression," *Phys. Rev. E*, vol. 100, p. 063205, Dec 2019.

[170] P. R. Spalart, "Philosophies and fallacies in turbulence modeling," *Progress in Aerospace Sciences*, vol. 74, pp. 1–15, 2015.

[171] H. Xiao and P. Cinnella, "Quantification of model uncertainty in rans simulations: A review," *Progress in Aerospace Sciences*, vol. 108, pp. 1–31, 2019.

[172] B. M. Haines, F. F. Grinstein, and J. D. Schwarzkopf, "Reynolds-averaged Navier–Stokes initialization and benchmarking in shock-driven turbulent mixing," *Journal of Turbulence*, vol. 14, no. 2, pp. 46–70, 2013.

[173] B. E. Morgan, B. J. Olson, W. J. Black, and J. A. McFarland, "Large-eddy simulation and reynolds-averaged navier-stokes modeling of a reacting rayleigh-taylor mixing layer in a spherical geometry," *Physical Review E*, vol. 98, 9 2018.

[174] B. Cockburn, S.-Y. Lin, and C.-W. Shu, "TVB Runge-Kutta local projection discontinuous Galerkin finite element method for conservation laws III: One-dimensional systems," *Journal of Computational Physics*, vol. 84, no. 1, pp. 90–113, 1989.

[175] S. Adjerid and T. C. Massey, "Superconvergence of discontinuous Galerkin solutions for a nonlinear scalar hyperbolic problem," *Computer Methods in Applied Mechanics and Engineering*, vol. 195, no. 25, pp. 3331–3346, 2006. Discontinuous Galerkin Methods.

[176] L. H. Khieu and E. Johnsen, *Analysis of Improved Advection Schemes for Discontinuous Galerkin Methods*, p. 3221. 2014.

[177] Z. Wang, "High-order methods for the Euler and Navier–Stokes equations on unstructured grids," *Progress in Aerospace Sciences*, vol. 43, no. 1, pp. 1–41, 2007.

[178] B. Cockburn and C.-W. Shu, "TVB Runge-Kutta Local Projection Discontinuous Galerkin Finite Element Method for Conservation Laws II: General Framework," *Mathematics of Computation*, vol. 52, no. 186, pp. 411–435, 1989.

[179] L. Krivodonova, "Limiters for high-order discontinuous Galerkin methods," *Journal of Computational Physics*, vol. 226, no. 1, pp. 879–896, 2007.

[180] J. Zhu, J. Qiu, and C.-W. Shu, "High-order runge-kutta discontinuous galerkin methods with a new type of multi-resolution weno limiters," *Journal of Computational Physics*, vol. 404, p. 109105, 2020.

[181] Y. Liu, C.-W. Shu, E. Tadmor, and M. Zhang, "Central discontinuous galerkin methods on overlapping cells with a nonoscillatory hierarchical reconstruction," *SIAM Journal on Numerical Analysis*, vol. 45, no. 6, pp. 2442–2467, 2007.

[182] Z. Xu, Y. Liu, and C.-W. Shu, "Hierarchical reconstruction for discontinuous galerkin methods on unstructured grids with a weno-type linear reconstruction and partial neighboring cells," *Journal of Computational Physics*, vol. 228, no. 6, pp. 2194–2212, 2009.

[183] R. B. Lowrie and J. E. Morel, "Discontinuous galerkin for hyperbolic systems with stiff relaxation," in *Discontinuous Galerkin Methods* (B. Cockburn, G. E. Karniadakis, and C.-W. Shu, eds.), (Berlin, Heidelberg), pp. 385–390, Springer Berlin Heidelberg, 2000.

[184] S. Bolding, J. Hansel, J. D. Edwards, J. E. Morel, and R. B. Lowrie, "Second-order discretization in space and time for radiation-hydrodynamics," *Journal of Computational Physics*, vol. 338, pp. 511–526, 2017.

[185] M. Holec, J. Limpouch, R. Liska, and S. Weber, "High-order discontinuous galerkin nonlocal transport and energy equations scheme for radiation hydrodynamics," *International Journal for Numerical Methods in Fluids*, vol. 83, no. 10, pp. 779–797, 2017.

[186] S. Tokareva and E. Toro, "Hllc-type riemann solver for the baer–nunziato equations of compressible two-phase flow," *Journal of Computational Physics*, vol. 229, no. 10, pp. 3573–3604, 2010.

[187] E. Franquet and V. Perrier, "Runge–kutta discontinuous galerkin method for the approximation of baer and nunziato type multiphase models," *Journal of Computational Physics*, vol. 231, no. 11, pp. 4096–4141, 2012.

[188] L. D. Gryngarten and S. Menon, "A generalized approach for sub- and supercritical flows using the local discontinuous galerkin method," *Computer Methods in Applied Mechanics and Engineering*, vol. 253, pp. 169–185, 2013.

[189] S. Osher and J. A. Sethian, "Fronts propagating with curvature-dependent speed: Algorithms based on Hamilton-Jacobi formulations," *Journal of Computational Physics*, vol. 79, no. 1, pp. 12–49, 1988.

[190] W. J. Rider and D. B. Kothe, "Reconstructing volume tracking," *Journal of Computational Physics*, vol. 141, no. 2, pp. 112–152, 1998.

[191] D. P. Starinshak, *Level set methods for multimaterial radiative shock hydrodynamics*. PhD thesis, University of Michigan, Ann Arbor, 2012.

[192] R. Abgrall, "How to prevent pressure oscillations in multicomponent flow calculations: A quasi conservative approach," *Journal of Computational Physics*, vol. 125, no. 1, pp. 150–160, 1996.

[193] K.-M. Shyue, "An efficient shock-capturing algorithm for compressible multicomponent problems," *Journal of Computational Physics*, vol. 142, no. 1, pp. 208–242, 1998.

[194] S. Alahyari Beig and E. Johnsen, "Maintaining interface equilibrium conditions in compressible multiphase flows using interface capturing," *Journal of Computational Physics*, vol. 302, pp. 548–566, 2015.

[195] P. Movahed and E. Johnsen, "A solution-adaptive method for efficient compressible multifluid simulations, with application to the richtmyer–meshkov instability," *Journal of Computational Physics*, vol. 239, pp. 166–186, 2013.

[196] M. T. Henry de Frahan, S. Varadan, and E. Johnsen, "A new limiting procedure for discontinuous Galerkin methods applied to compressible multiphase flows with shocks and interfaces," *Journal of Computational Physics*, vol. 280, pp. 489–509, 2015.

[197] K. So, X. Hu, and N. Adams, "Anti-diffusion interface sharpening technique for two-phase compressible flow simulations," *Journal of Computational Physics*, vol. 231, no. 11, pp. 4304–4323, 2012.

[198] K.-M. Shyue and F. Xiao, "An Eulerian interface sharpening algorithm for compressible two-phase flow: The algebraic THINC approach," *Journal of Computational Physics*, vol. 268, pp. 326–354, 2014.

[199] E. Johnsen and T. Colonius, "Implementation of WENO schemes in compressible multicomponent flow problems," *Journal of Computational Physics*, vol. 219, no. 2, pp. 715–732, 2006.

[200] V. Coralic and T. Colonius, "Finite-volume weno scheme for viscous compressible multicomponent flows," *Journal of Computational Physics*, vol. 274, pp. 95–121, 2014.

[201] S. Kawai and H. Terashima, "A high-resolution scheme for compressible multicomponent flows with shock waves," *International Journal for Numerical Methods in Fluids*, vol. 66, pp. 1207–1225, Aug. 2011.

[202] E. Johnsen and F. Ham, "Preventing numerical errors generated by interface-capturing schemes in compressible multi-material flows," *Journal of Computational Physics*, vol. 231, no. 17, pp. 5705–5717, 2012.

[203] M. Baer and J. Nunziato, "A two-phase mixture theory for the deflagration-to-detonation transition (ddt) in reactive granular materials," *International Journal of Multiphase Flow*, vol. 12, no. 6, pp. 861–889, 1986.

[204] A. Murrone and H. Guillard, "A five equation reduced model for compressible two phase flow problems," *Journal of Computational Physics*, vol. 202, no. 2, pp. 664–698, 2005.

[205] A. K. Kapila, R. Menikoff, J. B. Bdzil, S. F. Son, and D. S. Stewart, "Two-phase modeling of deflagration-to-detonation transition in granular materials: Reduced equations," *Physics of Fluids*, vol. 13, no. 10, pp. 3002–3024, 2001.

[206] G. Perigaud and R. Saurel, "A compressible flow model with capillary effects," *Journal of Computational Physics*, vol. 209, no. 1, pp. 139–178, 2005.

[207] F. Petitpas, J. Massoni, R. Saurel, E. Lapebie, and L. Munier, "Diffuse interface model for high speed cavitating underwater systems," *International Journal of Multiphase Flow*, vol. 35, no. 8, pp. 747–759, 2009.

[208] J. J. Kreeft and B. Koren, "A new formulation of kapila's five-equation model for compressible two-fluid flow, and its numerical treatment," *Journal of Computational Physics*, vol. 229, no. 18, pp. 6220–6242, 2010.

[209] W. Sutherland, "Lii. the viscosity of gases and molecular force," *The London, Edinburgh, and Dublin Philosophical Magazine and Journal of Science*, vol. 36, no. 223, pp. 507–531, 1893.

[210] J. Larsen, *Foundations of high-energy-density physics: Physical processes of matter at extreme conditions*. Cambridge University Press, 2017.

[211] S. Atzeni and J. Meyer-ter Vehn, *The Physics of Inertial Fusion: Beam Plasma Interaction, Hydrodynamics, Hot Dense Matter*. OUP Oxford, 2004.

[212] G. Allaire, S. Clerc, and S. Kokh, "A five-equation model for the simulation of interfaces between compressible fluids," *Journal of Computational Physics*, vol. 181, no. 2, pp. 577–616, 2002.

[213] G. H. Miller and E. G. Puckett, "A high-order godunov method for multiple condensed phases," *Journal of Computational Physics*, vol. 128, no. 1, pp. 134–164, 1996.

[214] J. C. Butcher, *Numerical Methods for Ordinary Differential Equations*. John Wiley & Sons, 2016.

[215] P. Roe, "Approximate riemann solvers, parameter vectors, and difference schemes," *Journal of Computational Physics*, vol. 43, no. 2, pp. 357–372, 1981.

[216] A. Harten, P. D. Lax, and B. van Leer, *On Upstream Differencing and Godunov-Type Schemes for Hyperbolic Conservation Laws*, pp. 53–79. Berlin, Heidelberg: Springer Berlin Heidelberg, 1997.

[217] V. Rusanov, "The calculation of the interaction of non-stationary shock waves and obstacles," *USSR Computational Mathematics and Mathematical Physics*, vol. 1, no. 2, pp. 304–320, 1962.

[218] G. D. Maso, P. L. Floch, and F. Murat, "Definition and weak stability of non-conservative products," *Journal de Mathématiques Pures et Appliquées*, vol. 74, pp. 483–548, 1995.

[219] S. Rhebergen, O. Bokhove, and J. van der Vegt, "Discontinuous galerkin finite element methods for hyperbolic nonconservative partial differential equations," *Journal of Computational Physics*, vol. 227, no. 3, pp. 1887–1922, 2008.

[220] F. Bassi and S. Rebay, "A High-Order Accurate Discontinuous Finite Element Method for the Numerical Solution of the Compressible Navier–Stokes Equations," *Journal of Computational Physics*, vol. 131, no. 2, pp. 267–279, 1997.

[221] D. N. Arnold, F. Brezzi, B. Cockburn, and L. D. Marini, "Unified analysis of discontinuous galerkin methods for elliptic problems," *SIAM Journal on Numerical Analysis*, vol. 39, no. 5, pp. 1749–1779, 2002.

[222] B. Cockburn and C.-W. Shu, "The local discontinuous galerkin method for time-dependent convection-diffusion systems," *SIAM Journal on Numerical Analysis*, vol. 35, no. 6, pp. 2440–2463, 1998.

[223] P. E. Johnson, L. H. Khieu, and E. Johnsen, "Analysis of recovery-assisted discontinuous galerkin methods for the compressible navier-stokes equations," *Journal of Computational Physics*, vol. 423, p. 109813, 2020.

[224] B. van Leer, "Towards the ultimate conservative difference scheme. V. A second-order sequel to Godunov's method," *Journal of Computational Physics*, vol. 32, no. 1, pp. 101–136, 1979.

[225] X.-D. Liu, S. Osher, and T. Chan, "Weighted Essentially Non-oscillatory Schemes," *Journal of Computational Physics*, vol. 115, no. 1, pp. 200–212, 1994.

[226] E. Johnsen, J. Larsson, A. V. Bhagatwala, W. H. Cabot, P. Moin, B. J. Olson, P. S. Rawat, S. K. Shankar, B. Sjögreen, H. Yee, X. Zhong, and S. K. Lele, "Assessment of high-resolution methods for numerical simulations of compressible turbulence with shock waves," *Journal of Computational Physics*, vol. 229, no. 4, pp. 1213–1237, 2010.

[227] G. Dimonte and M. Schneider, "Turbulent Richtmyer–Meshkov instability experiments with strong radiatively driven shocks," *Physics of Plasmas*, vol. 4, no. 12, pp. 4347–4357, 1997.

[228] O. A. Hurricane, J. F. Hansen, H. F. Robey, B. A. Remington, M. J. Bono, E. C. Harding, R. P. Drake, and C. C. Kuranz, "A high energy density shock driven Kelvin–Helmholtz shear layer experiment," *Physics of Plasmas*, vol. 16, no. 5, p. 056305, 2009.

[229] F. D. Swesty and E. S. Myra, "Numerical Algorithm for Modeling Multigroup Neutrino-Radiation Hydrodynamics in Two Spatial Dimensions," *The Astrophysical Journal Supplement Series*, vol. 181, pp. 1–52, feb 2009.

[230] G. I. Taylor, "The formation of a blast wave by a very intense explosion i. theoretical discussion," *Proceedings of the Royal Society of London. Series A. Mathematical and Physical Sciences*, vol. 201, no. 1065, pp. 159–174, 1950.

[231] K. Schmidmayer, S. H. Bryngelson, and T. Colonius, "An assessment of multicomponent flow models and interface capturing schemes for spherical bubble dynamics," *Journal of Computational Physics*, vol. 402, p. 109080, 2020.

[232] D. Wirasaet, S. Tanaka, E. Kubatko, J. Westerink, and C. Dawson, "A performance comparison of nodal discontinuous Galerkin methods on triangles and quadrilaterals," *International Journal for Numerical Methods in Fluids*, vol. 64, no. 10-12, pp. 1336–1362, 2010.

[233] Z. Drmač, I. Mezić, and R. Mohr, "Data driven modal decompositions: Analysis and enhancements," *SIAM Journal on Scientific Computing*, vol. 40, no. 4, pp. A2253–A2285, 2018.

[234] H. Ye, R. J. Beamish, S. M. Glaser, S. C. H. Grant, C. hao Hsieh, L. J. Richards, J. T. Schnute, and G. Sugihara, "Equation-free mechanistic ecosystem forecasting using empirical dynamic modeling," *Proceedings of the National Academy of Sciences*, vol. 112, no. 13, pp. E1569–E1576, 2015.

[235] E. Feinberg, G. Cearley, E. Johnsen, C. Kuranz, P. Poole, P. Porazik, S. Moon, B. Blue, and L. Berzak Hopkins, "Direct laser impulse effects on titanium," in *APS Division of Plasma Physics Meeting Abstracts*, vol. 2021, pp. CO03–015, 2021.

[236] A. Kanevsky, M. H. Carpenter, D. Gottlieb, and J. S. Hesthaven, "Application of implicit–explicit high order Runge–Kutta methods to discontinuous-Galerkin schemes," *Journal of Computational Physics*, vol. 225, no. 2, pp. 1753–1781, 2007.

[237] M. M. Crockatt, A. J. Christlieb, C. K. Garrett, and C. D. Hauck, "Hybrid methods for radiation transport using diagonally implicit runge–kutta and space–time discontinuous galerkin time integration," *Journal of Computational Physics*, vol. 376, pp. 455–477, 2019.

[238] R. J. LeVeque, D. Mihalas, E. Dorfi, and E. Müller, *Computational Methods for Astrophysical Fluid Flow: Saas-Fee Advanced Course 27. Lecture Notes 1997 Swiss Society for Astrophysics and Astronomy*, vol. 27. Springer Science & Business Media, 2006.

[239] S. Chandrasekhar, *Radiative transfer*. Courier Corporation, 2013.

[240] E. Landi Degl'Innocenti and M. Landi Degl'Innocenti, "Transfer equations for polarized light," *Il Nuovo Cimento B (1971-1996)*, vol. 27, no. 1, pp. 134–144, 1975.